A SEARCH FOR GRAVITATIONAL RADIATION

FROM PSR 1937+214

Thesis by

Mark Hereld

In Partial Fulfillment of the Requirements

for the Degree of

Doctor of Philosophy

California Institute of Technology

Pasadena, California

1984

(Submitted June 17, 1983)

ACKNOWLEDGEMENTS

I owe the dregs of my sanity to the collective membership, past and present, of the Gravitational Physics and Theoretical Astrophysics groups at Caltech. The combination of personalities has made for a working environment which promotes progress while usually remaining unharried. I've learned a great deal in collaboration with these people, some of it physics.

Ron Drever is to be thanked specially for his unflagging support as my advisor. Stan Whitcomb's time as vice-advisor has been constantly appreciated. I am particularly grateful for his comments and suggestions on early drafts of the thesis. Bob Spero and Dana Anderson have given support and suggestions. And for their help in manning the experiment I thank the rest of the group: Yekta Gürsel, Mike Bischoff, Gary Gutt, and Jim Kaufman.

Siu Au Lee's contributions to the Caltech effort, which include work on the problem of stabilizing the laser, are gratefully acknowledged by the entire group.

The Caltech Gravitational Physics group continues to benefit from the work being done by the Glasgow group, and from interaction with its members: R.W.P. Drever, W.A. Edelstein, G.M. Ford, S. Hoggan, J. Hough, I. Kerr, W. Martin, B.J. Meers, A.J. Munley, G.P. Newton, J.R. Pugh, N.A. Robertson, and H. Ward.

My debt to Carl Caves is extensive.

I'd like to thank my parents - Jerry and Lorraine - and my brothers and sister - Kurt, Scott, Dale, and Kerry - for the love and support they've shown me for as long as I've known them. I wouldn't have wanted it any other way.

And finally, I'd like to express my love and thanks to Catherine, whose friendship and confidence have made it easier for me even while things were less

than easy for her.

My work at Caltech has been supported in part by National Science Foundation grants PHY79-12305 and PHY82-04056, an Institute Fellowship in 1978-79, and aid from the Federally funded College Work-Study Program.

ABSTRACT

A search for gravitational radiation from the "millisecond pulsar", PSR 1937+214, using a 40 meter baseline laser interferometric detector is described. Four days of observation yielded 1.2×10^5 seconds of data. Throughout the experiment, the pulsar phase was synthesized to an accuracy of better than one tenth of the pulsar period. A trigger generated from this signal synchronized the data averaging. Narrow band amplitude spectra centered at the pulsar's fundamental electromagnetic pulsation frequency (~642 Hz) and its first harmonic were obtained. The spectra, one for each combination of polarization and center frequency, place 99.7% confidence level limits on the emitted gravitational radiation. In dimensionless strain, h, the rms limits are:

642 Hz	"plus" polarization	1.6×10^{-17}
"	"cross" "	3.1×10^{-17}
1294 Hz	"plus" polarization	1.1×10^{-17}
"	"cross" "	1.5×10^{-17}

Over the four day observing period, the performance of the detector varied with changing temperature. During the stable night hours, the two optical cavities remained locked to reflection minima for 20 to 80 minutes before momentarily losing lock. Temperature changes of 1° to 2° C in the morning and evening necessitated compensating adjustments to the optics to maintain good fringe visibility.

The interferometer senses changes in the separations between three test masses. The test masses hang like pendulums so that they are free to move in response to gravitational radiation. The suspension system is designed to provide passive isolation from seismic and environmental vibration noise. The

orientation of each test mass is stabilized with a feedback loop. The design of the test masses, their suspension systems, and the servo system which controls their orientation is described.

TABLE OF CONTENTS

Chapter 1
INTRODUCTION

The challenge of detecting gravitational radiation is motivated by several things. As a test of theories of gravitation it stands apart from the classic tests: the gravitational redshift, the bending of light by the sun, the precession of Mercury's perihelion, and the dragging of inertial frames. The approximations made in studying these effects perturbatively are different from those that go into studying gravitational radiation. The aspects of gravitation probed are thus different. Detection of gravitational waves can provide the speed of their propagation. One way to do this is by measuring the time of flight of a disturbance between two widely separated detectors. As another example of physics essentially inaccessible to the classic tests, gravity waves can provide polarization information which is tantamount to identifying the spin content of the gravitational interaction. (In fact, indirect evidence for the existence of gravitational radiation may already be in hand. Observations of pulse arrival times from the binary pulsar PSR 1913+16 have been used by Taylor and Weisberg (1982) to "rule out a number of theories of gravitation previously considered viable.")

A stronger motivation, particularly in light of the dwindling probability of an alternative to General Relativity, is the new window on astrophysical processes provided by gravitational radiation. Much of what goes on, for example, in the birth of a neutron star or a black hole during a supernova is hidden from us by a cloak of electromagnetically opaque matter. Gravitational radiation, because of its weak coupling to this matter, can pass unabsorbed through the expanding stellar material. Even in the absence of an "electromagnetic cloak" the information carried by gravitational radiation tends to be of a different nature. Its amplitude waveform and polarization content carry information about the

catastrophic dynamics of the collapse, unavailable from electromagnetic signals.

1.1. Sources of Gravitational Radiation

The sources of gravitational radiation can be divided into three somewhat overlapping categories: 1) the *burst sources* include broad band sources of gravitational waves arising from cataclysmic events such as supernovae and collisions between black holes, 2) *periodic sources* include binary systems and rapidly rotating compact objects like pulsars, and 3) *stochastic background sources* include remnant radiation from the early universe as well as the composite radiation that may be produced by a large number of objects radiating out of synchrony with one another.

The estimates and calculations of many theorists have been combined and interpreted by Thorne (1980). The results are reproduced here in Figure 1.1. For details and further references on sources see Smarr (1979). The sources have been characterized by two parameters: dimensionless strain, h, and frequency. A passing gravitational wave distorts distances by changing the metric components, $g_{\mu\nu}$, which define the separation between events in spacetime.[1)] The dimensionless strain measures the magnitude of the metric perturbation due to the passing gravitational wave. It is roughly the induced change in length per unit length, $\delta L / L$.

For burst sources, shown in the vertically hatched region of the figure, the "frequency" is roughly the inverse duration of the impulsive event. The strain, h, is the rms strain in that time interval. These estimates are based on an event rate of one burst per month. For example, the figure is populated in the 1 kHz

[1)] Any good text on gravitation will explain these concepts further. For example, see Chapter 10 in Weinberg (1972) or Chapter 35 in Misner, Thorne, and Wheeler (1973)

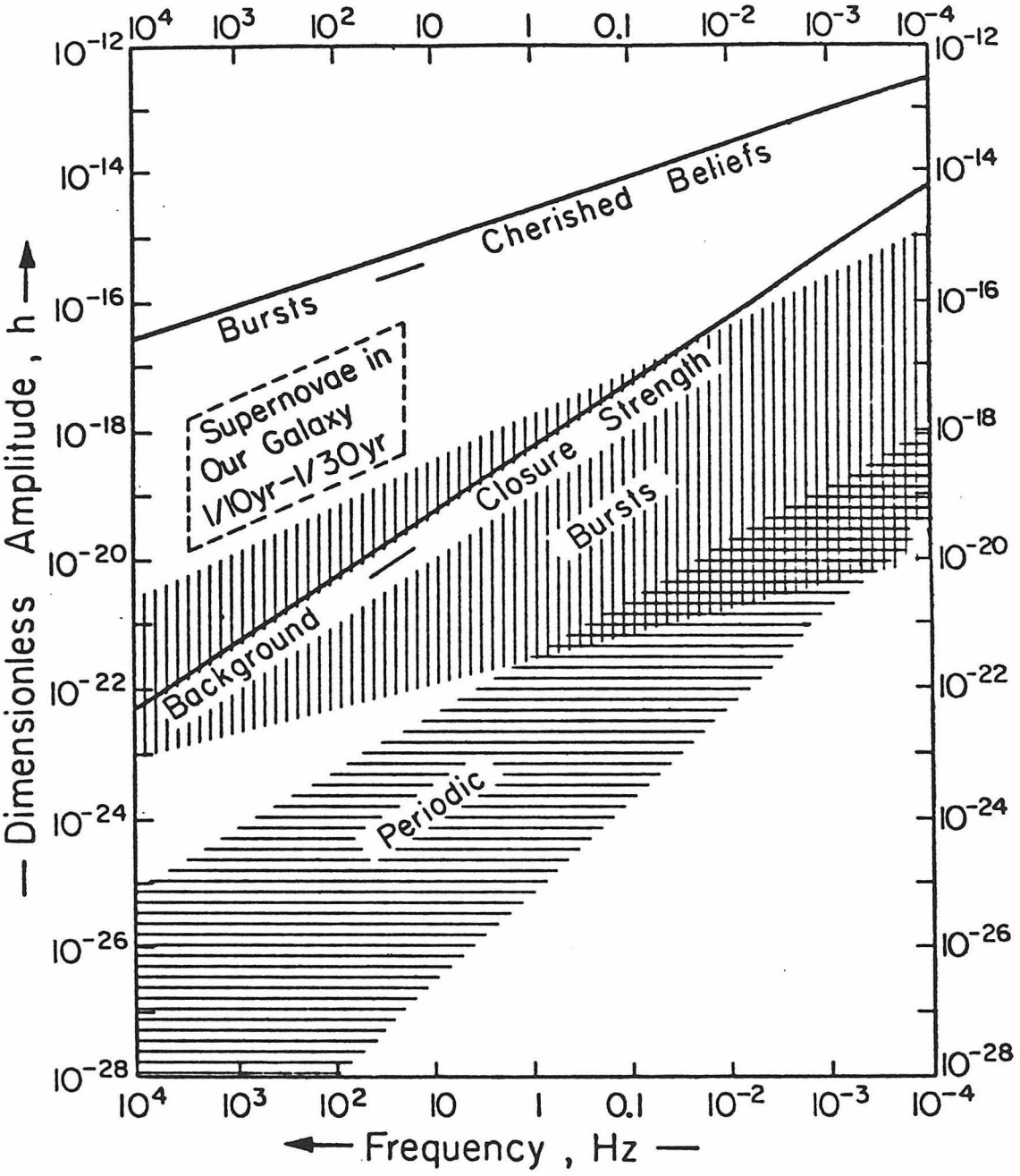

Figure 1.1. Estimates of the strengths of the gravitational waves that bathe the Earth. Bursts of gravitational radiation, at a rate of one per month, might have amplitudes as high as the "cherished beliefs" line without violating any of our fundamental beliefs about the Universe. They are more likely to lie in the vertically hatched region according to current models. A stochastic background with an energy density large enough to close the Universe is represented by the "closure strength" line. This is likely to be larger than the existing background by several orders of magnitude.

regime by the violent deaths of stars in supernovae to form neutron stars or black holes. Gravitational radiation is produced by the asymmetrical collapse and bounce of the $\sim 1\,M_{\odot}$ stellar interior with a time scale of about 1 msec. Detecting a supernova in our own galaxy might require a sensitivity of only 10^{-18} in dimensionless strain amplitude but is likely to happen only once in 10 to 30 years. For once-a-month event rates a detector must be sensitive to supernovae as far away as the Virgo cluster of galaxies (10 to 20 Mpc). Other sources of broad band burst energy in gravitational waves include neutron star core quakes and collisions between black holes or neutron stars.

The horizontally hatched area includes the estimated rms strains from periodic sources. Rapidly rotating neutron stars with time varying quadrupole moments fall into this category. Estimates for the Crab and Vela pulsars made by Zimmermann (1978) and revised by Zimmermann and Szedenits (1979) place the probable dimensionless strain at 5×10^{-27} and 3×10^{-26} respectively. They are expected to radiate at their respective rotation frequencies, 30 Hz and 11 Hz. Periodic sources also include compact binary systems. Most notably the binary pulsar PSR 1913+16 which has been monitored since 1974, shows evidence by pulse arrival timing interpreted as orbital decay due to the emission of gravitational radiation (Taylor and Weisberg 1982). Its orbital period of about $7^{h}45^{m}$ implies a gravitational wave frequency of about 10^{-4} Hz, probably too low for earth-based detection. At the more exotic end of the frequency scale, it is tempting to suggest a pair of neutron stars circling one another in a near grazing orbit (separated by ~20 km). They will have an orbital period of about 1 msec but will radiate away their orbital energy on a time scale of only one orbit, leading to a violent coalescence of the two stars more typical of a burst source.

1.2. Gravity Wave Detectors

The search for gravitational radiation began over 20 years ago with the pioneering work of Weber (1960). The bar detector, which he invented, has seen several orders of magnitude increase in sensitivity due to improved transducer technology and the change from room temperature operation to liquid helium temperature operation. The field has also expanded to include different kinds of detectors: 1) earth based free mass antennas which use laser interferometry to measure changes in the separation between test masses, and 2) Doppler tracking of spacecraft in which the earth-spacecraft separation is measured.

The Weber-type bar antenna is a machined cylinder of high Q material - typically aluminum, although niobium, sapphire, and silicon are being used or tested for the purpose. The fundamental longitudinal mode of oscillation is about 1 kHz for the bars currently operating and under construction (see Braginsky and Thorne 1980 for a summary). Gravitational waves will excite this mode of the bar, changing the complex amplitude of the oscillation a detectable amount. The Stanford bar represents the state-of-the-art for resonant mass detectors of this kind. It is a 5 ton aluminum bar cooled to 4.3 K with an maximum Q of 6×10^6. The changes in the motion of the end of the bar are sensed by a transducer which is carefully designed for low noise performance and optimal mechanical coupling. It has an rms noise level corresponding to a sensitivity of about 10^{-18} in h (Boughn et al. 1982).

The laser interferometric free mass antenna was first considered by Moss, Miller, and Forward (1971), Weiss (1972) and Forward (1978). Three test masses are placed on two perpendicular lines - one at the intersection, and the other two at a distance, L, down each line. They are free to move with respect to one another under the influence of gravitational radiation. Differential length changes in the two baselines, $L_1 - L_2$, are measured by laser light which travels

down each arm and is made to interfere with itself - the changing interference fringes indicate changing separation. A gravity wave of ideal polarization will cause one baseline to shorten while the other lengthens which registers as a change in $L_1 - L_2$. In the original scheme, now in use at MIT (Weiss 1972) and in Munich (Rüdiger et al. 1982), the light is divided by a beam splitter on the corner test mass and traverses the baseline distance several times (bouncing between mirrors on the test masses) before being recombined - a multipass Michelson interferometer. The scheme used at Caltech and Glasgow (Drever et al. 1982) is slightly different, but analogous. The mirrors of the multipass Michelson which cause the beam to bounce back and forth without overlapping are replaced by two smaller mirrors which form a Fabry-Perot cavity. The light effectively travels the length many times, but the beams are completely overlapping. (This scheme will be discussed in more detail in Chapter 2.)

1.3. Overview

In this investigation, I used the 40 meter Caltech interferometer to search for periodic gravitational radiation from PSR 1937+214, the recently discovered "millisecond" pulsar (Backer et al. 1982). The output of the detector was averaged over a period of 94 consecutive hours (possible because gravity waves pass virtually unchanged through the earth). The averaging was synchronized to the phase of the pulsar, using an ephemeris calculated from the published period, right ascension, and declination of the pulsar (Backer, Kulkarni, and Taylor 1983) and the Astronomical Almanac (1983). Analysis of the data provided narrow band spectra centered at the pulsar's electromagnetic pulsation frequency and its first harmonic. Polarization information was also recovered from the experimental data by virtue of the earth's daily rotation. The changing orientation of the antenna with respect to the source caused its response to the two

polarizations to be distinguishable over the course of a day.

The operation of the Caltech interferometer (its optics, electronics, and sensitivity) is described in Chapter 2. Chapter 3 discusses the earmarks of a periodic source in general, PSR 1937+214 specifically, and gravitational radiation from rapidly rotating neutron stars. These two chapters provide the necessary background for understanding the experiment and the motivations behind it. In Chapter 4, I describe the experimental setup: instrumentation, data collection, and calibration. Then, in Chapter 5, I explain how the data were corrected for gravity wave polarization and reduced to provide narrow band spectral components of the dimensionless strain. Chapter 6 contains discussion of the actual data collection run, the results and their implications. Finally, one of my main contributions to the construction of the Caltech interferometer is highlighted in the Appendix. While others were working on stabilizing the laser to a Fabry-Perot cavity, designing the vacuum system, and tracking down sources of noise, I was designing and building the test masses, their suspension system, and the overall orientation control system. The considerations that went into their design as well as details of their construction are discussed there.

Chapter 2

THE CALTECH 40 METER INTERFEROMETER

The Caltech interferometer is housed in an L-shaped laboratory built onto the side of the existing Central Engineering Services building on campus. A photograph of the interferometer and laboratory is shown in Figure 2.1. At each of the three vertices is a concrete pad isolated from the surrounding foundation. Local ground disturbances caused by moving people or equipment do not couple strongly to the interferometer. An optical table supported by pneumatic feet rests on each pad. The pneumatic feet, though not used in the experiment to be described, can in time of need be pressurized to provide seismic isolation - also allowing the weight distribution on the table to be changed without changing its tilt. A vacuum tank on each table contains the freely hanging test mass. Each test mass has optical components on it so that the differential changes in their separations can be measured with the 514.5 nm wavelength light from a Lexel argon ion laser.

Two 40 meter lengths of 20 cm diameter stainless steel vacuum pipe connect the tanks. The pipes are suspended at intervals along their lengths by rope and winch. Each tank joins to the pipe with a flexible bellows section so that motions of the pipe are not transmitted to the tank. Each pipe-to-tank bellows is balanced with a second flexible bellows on the opposite side of the tank which is evacuated with the pipe so that atmospheric pressure doesn't collapse the bellows.

The entire vacuum system - tanks and pipes - is evacuated to a few millitorr by two rotary pumps. A cold trap and a molecular sieve on each pump prevent back-streaming oil from contaminating the delicate optical surfaces.

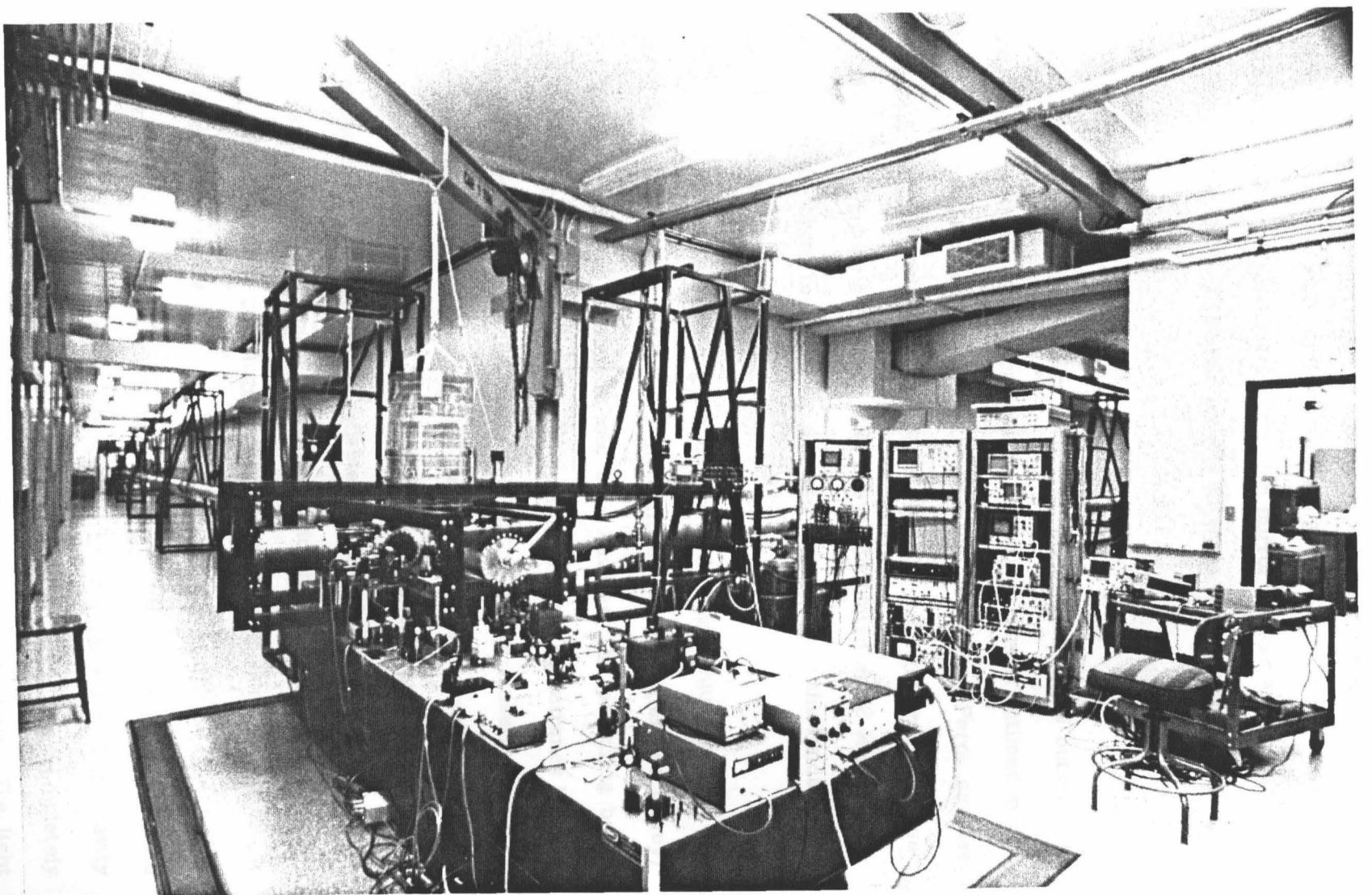

Figure 2.1. A view of the 40 meter interferometer from the corner of the lab. In the foreground is the optical table on which the laser and the central tank sit.

Light enters the vacuum system through glass viewports on the tanks. Electrical signals which drive motor-controlled mirror mounts and transducers to stabilize the orientation of the test masses enter via vacuum feedthroughs.

2.1. The Interferometer

Although the optics are subject to change, particularly those outside the vacuum tanks, the configuration used during the experiment is outlined in Figure 2.2. The interferometer consists of two identical Fabry-Perot cavities oriented perpendicular to one another. Linearly polarized light from the laser passes through a Pockels cell where it is phase modulated at 12 MHz. A telescope expands the beam to match its size and divergence to the fundamental transverse mode of each cavity.

This beam passes through a glass viewport into the vacuum tank at the corner of the L. The beam splitter on the central test mass (labeled Dewey) divides the light equally, sending it into both cavities. The polarizing beam splitter and the quarter wave plate ($\lambda/4$) combination at the entrance to each cavity isolates the laser from light reflected off the cavity. Linearly polarized light from the laser is transmitted by the coated diagonal surface of the polarizing beam splitter. After two passes through the quarter wave plate the polarization is rotated by 90° and the light is reflected by the polarizing beam splitter so than it doesn't return to the laser. This precaution minimizes parasitic oscillations and other possible couplings through the laser plasma which might degrade noise performance.

Light reflected from each cavity is directed out of the central tank and onto a photodiode on the optical table. Because of the narrow width of the cavity resonance ($\sim$10 kHz), the 12 MHz modulation sidebands are completely reflected. Only light in the central peak is stored in the cavity. The light

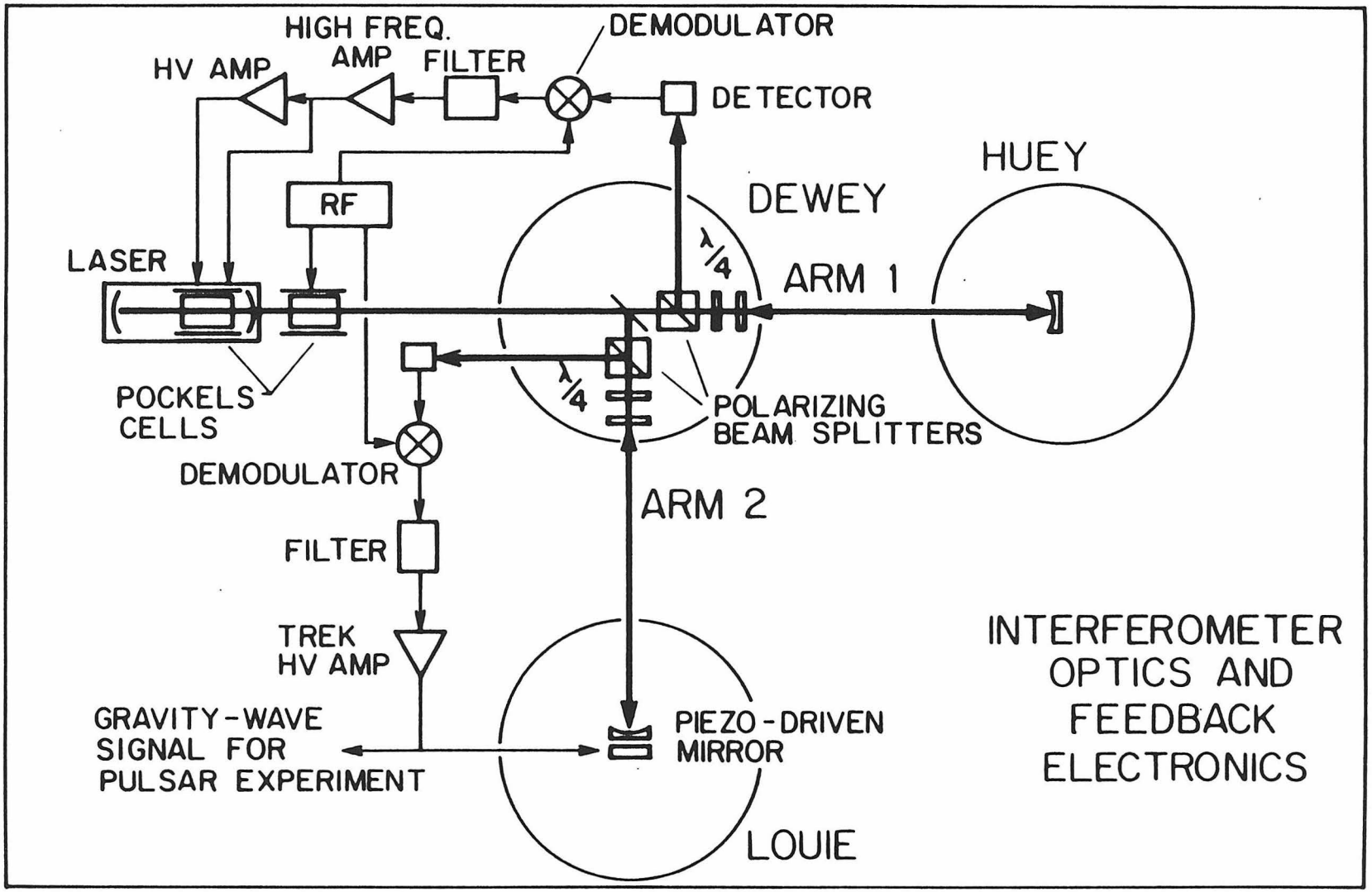

Figure 2.2. The interferometer. Two Fabry-Perot cavities monitor the Huey-Dewey and Dewey-Louie separations. The first arm signal stabilizes the laser frequency to cavity 1. The second error signal is applied, after filtering and amplification, to the piezo mirror.

reaching the photodiode has two components of interest: 1) the reflected sidebands, and 2) the unmodulated central component leaking out of the cavity. It is this second component which carries the cavity length information. The two components interfere at the photodiode, effectively comparing the phase of the laser to the phase of the light stored by the cavity. The demodulated signal representing the signed deviation from resonance is applied to various transducers to keep the cavities in resonance. The nature of this feedback is quite different in the two arms.

The phase signal from the first cavity is filtered and amplified and applied as feedback to an intra-cavity Pockels cell in the laser. Fluctuations in the laser frequency are corrected so that the laser frequency tracks a longitudinal mode of the hanging cavity. At high frequencies, above a few tens of Hertz, this cavity is extremely stable compared to the laser cavity. This is due to the very effective vibration isolation, the lack of a turbulent active medium, the relatively high reflectivity of its mirrors, and the large separation between cavity mirrors. At low frequencies, because of the resonant nature of the passive vibration isolation and the intrinsically larger ground noise, the stability is not as good.

The second cavity is equipped with a piezoelectrically movable mirror on the distant mass (labeled Louie). This "piezo mirror" presently has its lowest resonance at about 9 kHz. The speed of this element has been critical in determining the maximum loop gain, and therefore the stability of the second cavity lock. The demodulated signal from the second cavity is applied to the piezo mirror after amplification and filtering. The second cavity length is made to track the stabilized laser frequency for frequencies up to the unity gain point of the feedback loop, typically in the range of 1500 to 3000 Hz.

The undamped motion of the test masses at 1 Hz often exceeds the dynamic range of this loop. To damp this motion, the low frequency portion of the second

cavity signal is differentiated and applied to one of the three test masses by moving the point from which it hangs with a piezoelectric transducer. This velocity dependent feedback removes energy from the low frequency eigenmode with normal coordinate $L_1 - L_2$. (The length of the first cavity, L_1, gets into the picture because the stabilized laser light feeding the second cavity contains low frequency variation due to the 1 Hz motions of Huey and Dewey.) In addition, a signal derived from an auxiliary Michelson interferometer has been useful in damping large motions caused by occasional excitations of the pendulums by transient ground noise. (This signal is described in more detail in the Appendix.)

2.2. The Test Masses

The test masses hang from their centers of mass. This minimizes couplings between their orientation and position. Without this feature the critical distance between test masses would be much more sensitive to ground noise and other effects which weigh on the overall sensitivity of the antenna. Because of this feature the orientation of mass must be stabilized before the cavities can be successfully held in resonance. Specifics of the pendulum suspension and orientation control are given in the Appendix.

The test masses, merely disks of aluminum serving as small optical tables, are suspended for two reasons. Firstly, being horizontally free to move at high frequencies they respond as ideal test masses to the impinging gravitational radiation. That is, in the jargon of one interpretation, they remain in "free fall" tied to their respective geodesics while the invariant interval between them (as measured by light) undulates in response to the passing radiation. Secondly, motions of the test mass due to motions of the suspension point are attenuated by the square of the frequency for $f > 1$ Hz.

The orientation of the masses must be controlled carefully before either cavity can resonate properly. The critical angular degrees of freedom are monitored with optical levers. "Damping" and "spring" signals derived from the monitor are applied to the test masses to critically damp their rotations and tilts. The necessary torques are supplied by the moving cones of loudspeakers which are mechanically linked to the suspension wires of the test masses. The feedback signal is rolled off above 15 Hz to avoid possible conversion of electronic noise to positional noise at the frequencies of interest near 1 kHz.

2.3. Noise Sources

I'll discuss some of the sources of noise facing the CIT interferometer - from the standard quantum limit which is irrelevant at present, to the thermal noise of the test mass. The discussion of isolating the test masses from seismic noise is left for the Appendix where the design of the suspension system is detailed.

The uncertainty principle applied to the measurement of the difference in positions of the test masses in a time τ leads to $\delta x \gtrsim \sqrt{2\hbar\tau / m}$. For the measurement of millisecond bursts of gravitational radiation, with 40 meters separating 10 kg test masses the standard quantum limit is $h \gtrsim 4\times10^{-21}$.

With the laser power currently available to our detector (on the order of 100 mW single mode), the standard quantum limit is not as relevant as the limit imposed by photon counting uncertainty. If the end mirrors have reflectivity R, and the first mirrors are chosen optimally, then this limit is $(1-R)\sqrt{\lambda\hbar c / 8\pi L^2 P\tau}$. Taking R to be .995, and P to be 10 mW, the millisecond burst sensitivity is $h \gtrsim 10^{-18}$.

Thermal noise may well be the nearest fundamental hurdle. The response of a harmonic oscillator to kT noise can be derived using an equivalent spectral density for the applied force given by $(\delta F)^2 / \delta f = 4kT\gamma$, where $\gamma = m\omega_0 / Q$ is

the damping coefficient in terms of the mass, resonant frequency, and quality factor of the oscillator. If $z \equiv \omega/\omega_0$ is the normalized frequency, then the spectral density of the oscillator amplitude is

$$\frac{(\delta x)^2}{\delta f} = \frac{1}{m^2\omega_0^4}\,\frac{1}{(1-z^2)^2+z^2/Q^2}\,\frac{4kT\omega_0 m}{Q} \qquad (2.1)$$

The kT noise in the 1 Hz pendulum motion doesn't pose a problem for frequencies $\gg 1$ Hz. In this limit the spectral density of test mass position is given by $(\delta x)^2/\delta f = 4kT\omega_0/mQ\omega^4$. For a mass of 10 kg and a quality factor of 10^6, this limits the sensitivity of the 40 meter interferometer to 1 msec bursts to $h \gtrsim 3\times10^{-22}$.

Where thermal noise poses more of a difficulty is in the vibrational modes of the test mass itself. In Munich it has been demonstrated that great care must be taken in designing the test mass and affixing the cavity mirror to it so that natural resonances remain at frequencies sufficiently above 1 kHz with quality factors high enough to localize the noise away from frequencies of interest (Rüdiger et al. 1982 and Schilling 1982). For $\omega < \omega_0$ the spectral density of the mirror position given by equation 2.1 reduces to $(\delta x)^2/\delta f = 4kT/mQ\omega^3$. For a carefully designed 10 kg test mass with a Q of 10^6 and a 5 kHz resonance the room temperature limit placed on the 40 meter interferometer is about $h \gtrsim 6\times10^{-21}$. Although these numbers are not representative of the current test masses, they do not seem unattainable.

Chapter 3

PERIODIC SOURCES

Although current theory and speculation indicate that burst sources may provide the first detection of gravitational radiation, periodic sources do have a certain lure. For one thing, burst events offer no known signature which distinguishes them from local noise. Reliable detection of such radiation will at present require two sensitive detectors operating simultaneously so that candidate events can be discarded if they are not registered by both detectors. On the other hand, the Doppler shift caused by the Earth's orbit and diurnal rotation provides an unmistakable signature which depends critically on the position of the source as well as the time of observation. Such a signal could be detected by a single detector.

A single broad band detector could in principle search for unknown periodic sources. Analysis of the correlation of the signal with time-shifted versions of itself, $\rho(\tau) \sim \int s(t)s(t+\tau)dt$, could provide the period(s) of the unknown source(s) as shifts, τ, which give peaks in ρ. The diurnal and annual Doppler shift of the period can give the position of the source as well as the speed of propagation of the radiation - all this with one detector!

As luck would have it, however, typical periodic sources are not only weak producers of gravitational radiation, they tend to radiate at inconveniently low frequencies. Terrestrial detectors are of necessity less sensitive at low frequencies because of the increasing difficulty of isolating them from gravitational gradients caused by fauna, weather, and other effects (Spero 1983).

3.1. The Fast Pulsar(s)

Pulsars, long studied theoretically as possible sources of gravitational radiation, have until recently remained at the edge of plausibility for Earth-based detection. Several searches for monochromatic gravitational radiation have been carried out (among them are Levine and Stebbins 1972, Hirakawa, Tsubono, and Fujimoto 1978, and Oide, Hirakawa, and Fujimoto 1979). The search for the 2ω component of the Crab pulsar, at 60.2 Hz, has achieved a noteworthy sensitivity of $h \approx 10^{-20}$ after 621 hours of integration (Oide, Hirakawa, and Fujimoto 1979). Needless to say, no detection has been reported.

With the discovery of PSR 1937+214 by Backer et al. (1982) came a great deal of excitement in the gravitational wave community. Its 642 Hz electromagnetic pulse rate is exceptionally high - some 20 times the pulse rate of the Crab pulsar, the hitherto fastest known pulsar. A tentative determination of the slow down rate led to the possibility that this pulsar might be braking by emission of gravitational radiation. On this evidence Hough et al. (1983) carried out a search at twice the primary pulse rate (1284 Hz), using an already existing bar detector. They announced their upper limit of $h \approx 10^{-20}$ at the 11^{th} Texas Symposium on Relativistic Astrophysics in Austin. At roughly the same time a more reliable determination of the slowdown rate came: $\dot{P} = (1.24 \pm 0.25) \times 10^{-19}$ sec/sec, an exceptionally small figure by pulsar standards. The pulsar parameters reported by Backer, Kulkarni, and Taylor (1983) are tabulated in Table 3.1.

The assumed rotation frequency of 642 Hz invites several interesting comments. At a frequency of $\sim$1800 Hz a 1 $M_\odot$ pulsar with a 10 km radius may be expected to become unstable to centrifugal breakup. At this frequency the centrifugal force at the equator balances the gravitational attraction. (This number is modified somewhat by details of the pulsar model, its actual mass, and radius.)

Parameters for PSR 1937+214	
Right Ascension (1950.0)	19h 37m 28.72s ±0.013s
Declination (1950.0)	21° 28' 01".3 ±0".2
Dispersion Measure	71.20 ±0.03 e pc cm^{-3}
Period	1.557 806 449 023 msec ±110 ilp
Apparent Period Derivative	$(1.24 \pm 0.25) \times 10^{-19}$ sec/sec
Epoch (JED)	2445303.263

Table 3.1

How this object acquired its 642 Hz rotation frequency is still largely a matter of debate. Some researchers contend that the pulsar was simply born in isolation with a very low magnetic field ($\lesssim 10^9$ gauss) so that its interaction with surrounding matter and its electromagnetic dipole radiation would be consistent with its spin-down rate.[1)] Henrichs and van den Heuval (1983) advance the idea that the pulsar was formed from the coalescence of a neutron star binary. The millisecond period is supposed to result from the final orbital period.

A perhaps more conventional scenario holds that such fast pulsars have been spun up by matter accreting onto their surface (Alpar et al. 1982; Fabian et al. 1983). The matter, supplied by a companion star that has exceeded its Roche lobe, forms a disk around the pulsar - the same mechanism that gives rise to the X-ray sources found in the galactic bulge. The Keplerian period of the matter at the accretion disks inner radius determines the maximum frequency

[1)] An interesting news item in Physics Today (March 1983, p. 19) discusses the discovery of PSR 1937+214 and the implications of its millisecond period.

to which the pulsar can be spun up. If the magnetic field were sufficiently low so that the disk of accreting matter could extend undisrupted to very near the pulsar surface, then frequencies of several hundred Hz would be possible.

3.2. Gravitational Radiation

If the pulsar is not being driven, an optimistic estimator of the gravitational radiation being emitted assumes that the observed slow down is due entirely to energy lost to gravitational radiation. For an assumed mass of 1 $M_\odot$ uniformly distributed in a sphere of radius of 10 km, the rate of rotational energy loss is

$$L_{spin} \equiv -\frac{d}{dt}E_{rot} = \frac{8\pi^2}{5}\frac{MR_0^2\dot{P}}{P^3} \tag{3.1}$$

$$= 1.0\times10^{36}\ \mathrm{erg/s} = 1.8\times10^{-11}\ M_\odot/\mathrm{yr}$$

This corresponds to an rms strain sensitivity at an assumed distance of 6 kpc of

$$h \simeq \left[\frac{4GL_{GR}}{c^3\omega^2R^2}\right]^{1/2}$$

$$= 1.2\times10^{-25}\left[\frac{L_{GR}}{10^{-8}M_\odot/\mathrm{yr}}\right]^{1/2}\left[\frac{R}{1\ \mathrm{kpc}}\right]^{-1}\left[\frac{f}{1\ \mathrm{kHz}}\right]^{-1} \tag{3.2}$$

$$= 1.3\times10^{-27}$$

if the radiation is at 642 Hz, half this if it is at two times the rotation frequency. I've assumed that $L_{GR} = L_{spin}$ (i.e., spin-down is due entirely to gravitational radiation). One could hope for more radiation than this even without requiring the pulsar to be driven. Gravitational potential energy could, for example, provide additional impetus. Starquakes and corequakes evidence the conversion of this

energy to rotational energy in the well known frequency "glitches" of the Vela and Crab pulsars.

To get more than this radiation from the pulsar it must be supplied with energy. It has been shown that a rapidly rotating star can become unstable to the emission of gravitational radiation (Chandrasekhar 1970). Calculations of this effect and its implications for pulsar models have been carried out by Wagoner (1983) and Friedman (1983), suggesting that the rotation frequency of PSR 1937+214 may be close to the necessary frequency. Particularly, for conditions which may be relevant to this pulsar, Wagoner calculates the strain that might result,

$$h \simeq 2.3\times10^{-26}\left[\frac{R}{1\ \mathrm{kpc}}\right]^{-1}\left[\frac{m\,f}{1\ \mathrm{kHz}}\right]^{-1/2}\left[\frac{\dot{M}}{10^{-8}M_{\odot}/\mathrm{yr}}\right]^{1/2} \tag{3.3}$$

where R is the distance to the pulsar, m is the azimuthal normal mode index of the oscillation, f is the gravitational radiation frequency, and $\dot{M}$ is the rate of mass deposition on the stellar surface. He has assumed that the magnetic field is sufficiently low ($B \lesssim 10^8$ gauss) for the accretion disk to extend unperturbed to the surface of the pulsar. It is important to note that f is *not* the rotational frequency. For the above to hold, the angular frequency must be roughly $.6\cdot(GM/R^3)^{1/2}$ (i.e. about half the centrifugal breakup frequency). The waves, however, can come out at any frequency in the range 200-1000 Hz (with m equal to 3 or 4) depending critically on the pulsar mass. So, although the gravitational luminosity may be larger than implied by the spin-down rate, it may be difficult to predict reliably the frequency of the radiation. As mentioned at the beginning of the chapter, however, this needn't be a serious drawback with a single broad band detector, like the one described in Chapter 2. The correlation function can provide the amplitude as well as the frequency of the source.

The output of a gravity wave detector can supply a great deal of information about the source. For example, Zimmermann and Szedenitz (1979), calculated the strain induced by gravitational waves from a freely precessing rigid body for two cases.

In the first case the body is axisymmetric, with principal moments $I_1 = I_2 \neq I_3$. The gravitational radiation has two frequency components, f and $2f$. The relative amplitudes and phases of the radiation at each of these frequencies and in the two polarizations, they point out, uniquely determine the angles between the angular momentum and the body's symmetry axis, θ, and between the angular momentum and the plane of the sky, i. In addition, the absolute value of the difference between the principal moments, $|I_3 - I_1|$, can be determined if the distance to the pulsar is known by other means.

Interestingly, the fundamental frequency, f, needn't be the electromagnetic pulse frequency f_{EM}. For small wobble angle, θ, the two frequencies differ by the precession frequency: $f_{EM} = f + f_P$. The precession frequency is given by $f_P = -\cos\theta\,\varepsilon f_{EM}$, and the ellipticity is $\varepsilon \equiv (I_3 - I_1)/I_1$. An observed difference between f_{EM} and f_P would provide the value of I_1 as well as the sign of ε.

In the context of this model, measurements of the gravitational radiation emitted can provide values for the moments of inertia of the spinning neutron star in addition to its spatial orientation. Also, Zimmerman and Szedenits point out that the radiation will be predominantly at f rather than $2f$ for small wobble angle.

The second case calculated by Zimmerman and Szedenits is that of a freely precessing triaxial rigid body (with $I_1 < I_2 < I_3$). The calculation was carried out to first order in mean wobble angle, θ_m. The gravitational radiation appears at three frequencies: $f_\pm \equiv (1 \pm \varepsilon)\overline{f_{EM}}$ and $2\overline{f_{EM}}$. The mean ellipticity is $\varepsilon \equiv 2[(I_3 - I_1)(I_3 - I_2)/I_1 I_2]^{1/2}$ and $\overline{f_{EM}}$ is the mean electromagnetic pulse

frequency. Measurements of the relative amplitudes at each frequency in each polarization can again be combined with the distance to the pulsar to obtain the moments of inertia, the mean wobble angle θ_m, and the inclination angle i.

3.3. Remarks

Keeping in mind that pulsars with periods less than about 10 ms were not observed earlier largely because they weren't looked for effectively, it might not be unreasonable to think that they may become important objects of study for gravitational astronomers. Additionally, models of these fast pulsars indicate that they must have weak magnetic fields so that they don't brake electromagnetically; in some models weak fields are even a prerequisite of the spin-up mechanism. The weak magnetic fields give rise to a systematically low electromagnetic pulse power - the fast pulsars may be hiding from view. If the braking is weak enough, their likely low production rate will be offset by their longevity. The very recent identification of a second fast pulsar by Boriakoff, Buccheri, and Fauci (1983) with a period of ~6 ms is encouraging.

The experiment I will describe in the remainder of this work is an application of a laser interferometer to the task of detecting gravity waves from a periodic source.[2)] The sensitivity is lower than the previously mentioned searches for periodic gravitational radiation at Tokyo and Glasgow with resonant mass detectors. This is simply a consequence of the relative youth of free-mass interferometric detector technology and is of no lasting concern. The naturally wide bandwidth of detectors like the 40 meter Caltech interferometer offers an important advantage over resonant detectors. Not only is a wider range of

[2)] Laser interferometers have been used by several researchers to look for periodic gravitational radiation. Among them, Levine and Stebbins (1972), Sadeh and Meidav (1972), and Mast et al. (1972) have searched for gravitational radiation from the Crab pulsar by sensing strains induced in the Earth.

periods accessible, but from a single measurement, information at the fundamental and harmonics can be culled. This distinctive property is demonstrated in the experiment and analysis described in the following chapters.

Chapter 4

THE EXPERIMENTAL SET-UP

The output of the Caltech interferometer was recorded for 4 days. During this time the phase of pulsar PSR 1937+214 was generated so that recorded data could be synchronously averaged. In this chapter I describe the instrumentation used to perform this task. First, I discuss the signal from the interferometer and the calibration of that signal. In the following section I describe the use of a desk-top computer interfaced to an analog-to-digital converter as the data collection system. The third section covers the generation of the pulsar phase. A rubidium clock provided the stable time reference. The desk-top computer controlled a frequency synthesizer which provided the pulsar phase. In the final section of this chapter I describe the measures taken to verify that the phase was not lost during the observing period; if the phase had been interrupted (due to a power failure, for example) the signal-to-noise ratio advantages of time averaging would be lost.

4.1. The Signal

At frequencies where the second cavity loop gain is high the voltage on the fast piezo mirror represents the difference in arm lengths. It is essentially this voltage which provided the gravity wave signal for the pulsar experiment (Figure 4.1). To avoid loading the piezo mirror drive amplifier or injecting noise at the critical fast piezo, the voltage from a divide-by-1000 resistor divider was used. To avoid saturating the PAR-113 preamp and analog-to-digital converter (ADC) to follow, a two pole high pass R-C network rejected frequency components of the signal below about 300 Hz. The preamp ground was isolated to break ground loops. The gain of the preamp brought the signal to a few volts rms so that the

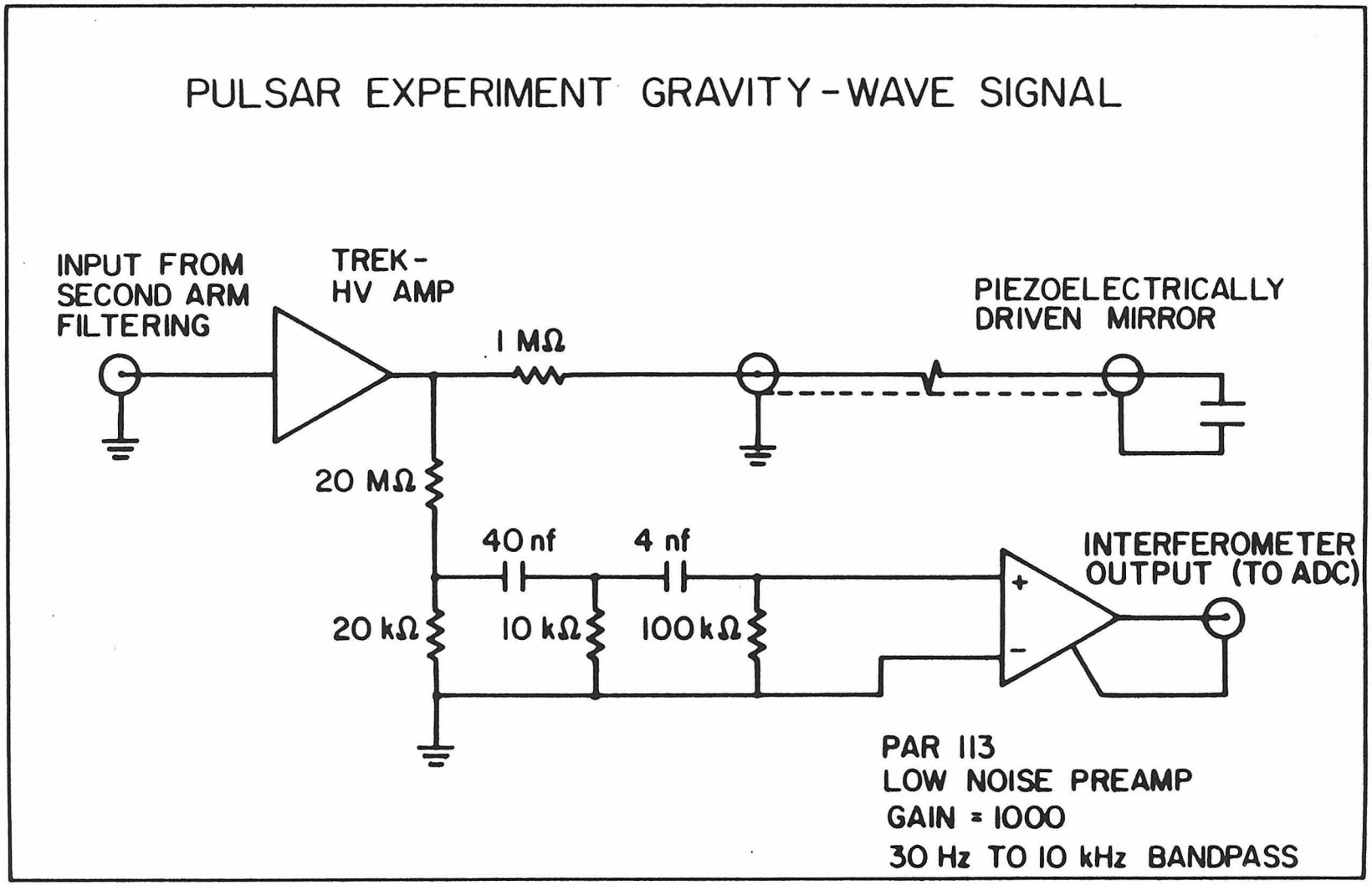

Figure 4.1. The interferometer output signal for the pulsar experiment. The 1 MΩ resistor in series with the capacitance of the piezo mirror provides a 6 dB per octave roll-off above 0.6 Hz. The RC network preceding the preamp filters out low frequency noise which might otherwise saturate the amplifier.

effect of pickup at the ADC was minimized.

The calibration of the voltage into the ADC included 3 factors. First, the piezo mirror was calibrated. The piezo mirror consists of an arrangement of three matched piezo stacks and a spring loaded mirror. How many nanometers of motion result from 1 volt applied? The most accurate value of 58±4 volts/order comes from a measurement using a microscope with a micrometer adjustable stage; one order is $\lambda/2$ which gives 4.4 nm/V for a wavelength of 514.5 nm. Various DC voltages were applied to one of the piezo stacks before it became part of the fast piezo mirror. The change in length of the stack was measured by keeping the face of the stack in focus with the micrometer on the microscope. This calibration for a single piezo stack under a microscope has been verified for the fast piezo mirror in the context of the second cavity, although with lower accuracy.

Second, the conversion from volts at the ADC to volts at the piezo mirror was measured. The input of the piezo mirror amplifier was driven by a sinusoid at the pulsar frequency, and at each of the first two harmonics. A spectrum analyzer measured the ratio of fast piezo volts to ADC volts. The results of the measurement were in accord with the values predicted by

$$\frac{\text{fast piezo volts}}{\text{ADC volts}} \simeq \left[\frac{f_0}{f}\right] \times \left[\frac{20\ \text{M}\Omega}{20\ \text{k}\Omega \parallel 10\ \text{k}\Omega}\right] \times \left[\frac{1}{\text{PAR gain}}\right] \qquad (4.1)$$

which is valid for frequencies f above f_0 and the high pass filter corner frequencies. The low pass corner, $f_0 \simeq .6$ Hz, is given by the capacitance of the fast piezo mirror and the series resistor. Above the high pass corner frequencies (~300 Hz) the capacitors in the filter approach negligible impedance so that the resistive divider is loaded by the resistance to ground of the filter. This fact is reflected in the second factor of equation 4.1.

The third factor which goes into converting volts at the ADC to differential length of the cavities is a correction for finite second cavity loop gain. Throughout the four day observation period the unity gain point of the second cavity feedback loop was measured at irregular intervals. It was measured most often after an adjustment of the optics to compensate for drifts - but, on a few occasions it was measured both before and after the adjustment to get an idea of how much it changed. The estimated average value for the unity gain point is 2200 Hz. Because of the $1/f$ dependence and the 90° phase shift of the loop gain for frequencies between about 80 Hz and a few kilohertz, the correction factor is

$$\left| \frac{1 + T(f)}{T(f)} \right| \simeq \left[1 + \left(\frac{f}{f_0} \right)^2 \right]^{1/2} \qquad (4.2)$$

where $T(f)$ is the complex loop gain, and f_0 is the unity gain frequency. For the fundamental pulsar frequency, 642 Hz, this gives a factor of 1.04 ; for the first harmonic, a factor of 1.16 .

It is important to realize that the above factors are sufficient to convert volts at the ADC to differential length change provided the PET wire pushing gain is lower than the fast mirror gain at the frequencies of interest. If not, then the motion of the fast mirror is supplemented by a motion of the support point while the loop tries to minimize the error signal at the detector. This situation would necessitate an additional correction factor. Because the gain of the wire pushing is small enough this effect can be neglected.

A typical 25.6 second average of the signal (Figure 4.2) shows a noise level of about 8.8×10^{-14} m/$\sqrt{\text{Hz}}$ at 640 Hz. The lower frequencies are attenuated by the high pass filter. The rises in the noise near 640 Hz and 1280 Hz are due to the violin mode resonances of the wires from which the test masses hang. This unfortunate circumstance from the point of view of the pulsar search at 642 Hz

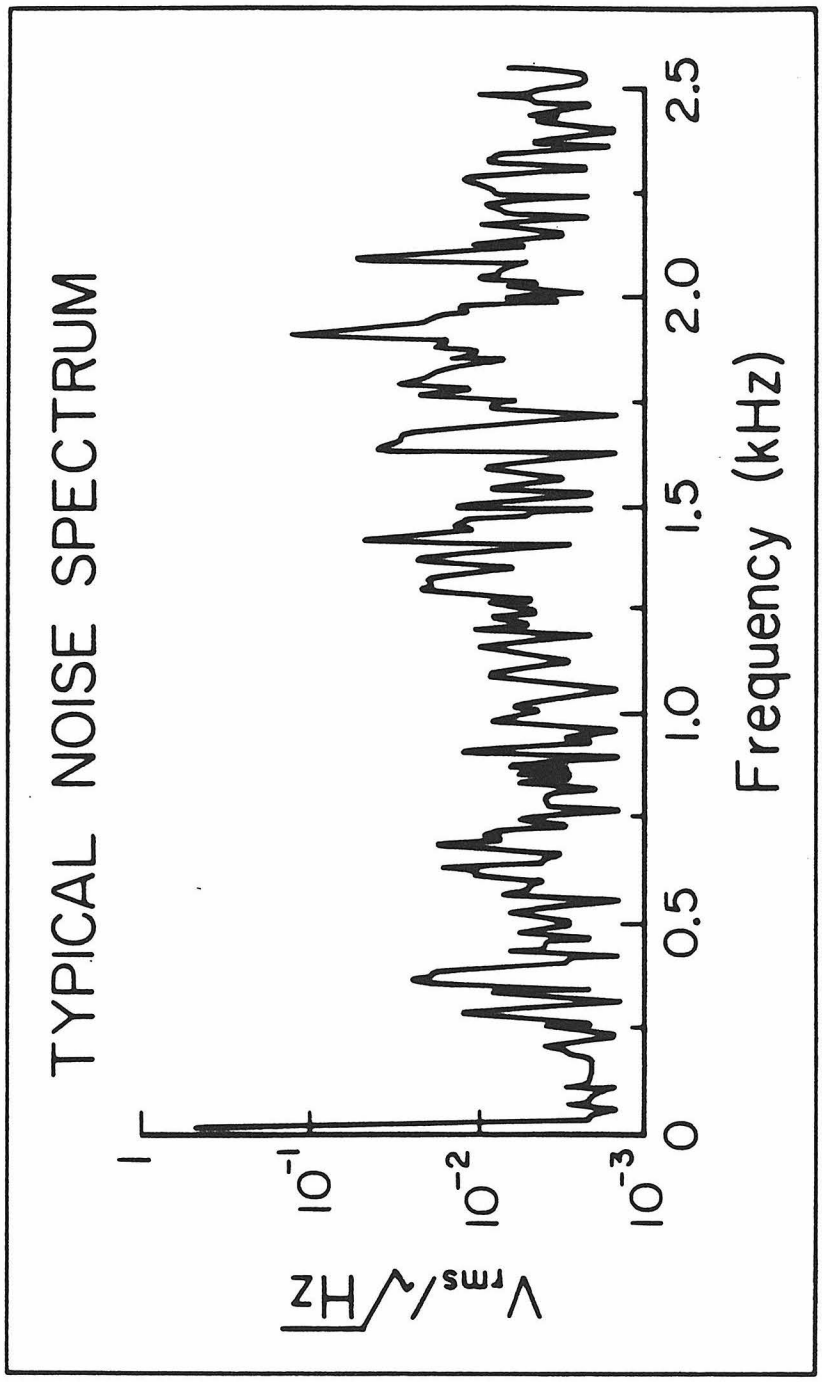

Figure 4.2. A typical noise spectrum taken at the interferometer output (see Figure 4.1). The peaks between 600 Hz and 700 Hz are due to the fundamental violin mode of the wires which support the test masses. Their first harmonics show up as peaks between 1.2 kHz and 1.5 kHz. The 10^{-2} $V/\sqrt{Hz}$ line corresponds to 6.7×10^{-14} $m/\sqrt{Hz}$ at 643 Hz and 3.7×10^{-14} $m/\sqrt{Hz}$ at 1284 Hz.

and 1284 Hz is, in fact, a design feature in a search for 1 msec burst sources. The wire length was chosen for the load of the test mass to give fundamental and first harmonic violin resonances which straddle the frequency of interest: 1 kHz.

4.2. Data Collection and Posting

The signal described in the last section was fed to an HP-3582A spectrum analyzer. The analyzer functioned as a 12-bit analog-to-digital converter and signal averager while its spectrum analyzing capabilities served only as a monitor. For this reason I refer to it as the ADC.

The data collection and timing instrumentation is shown in Figure 4.3. An HP-85A desk-top calculator (CPU - for lack of a more appropriate term) equipped with and HP-IB interface controlled the ADC. The ADC sampled the incoming signal at 10.24 kHz for .1 seconds resulting in a digitized time trace 1024 samples in length. A trigger pulse derived from the Doppler shifted pulsar frequency synchronized the start of each trace to a fixed phase of the pulsar cycle. Two hundred and fifty six (256) such time traces were averaged by the ADC before the CPU transferred the resulting 1024 point average trace to its own memory and restarted the ADC. As many as 32 of these average traces were summed in the CPU memory and written to tape every 30 minutes. A threshold detector monitored the light level falling on each of the cavity photodiodes. While the servo loop remained locked, this light level was low, but if either cavity fell out of lock, one or both of the threshold detectors would alert the CPU via hardware interrupt. The CPU responded by discarding the data already in the ADC averaging buffer and restarting the ADC after the offending servo loop reacquired lock. Most often, this would be within a fraction of a second.

The data collecting efficiency was low. That is, for 30 minutes of real time, only about 10 minutes of data went into the averaged trace that was written to

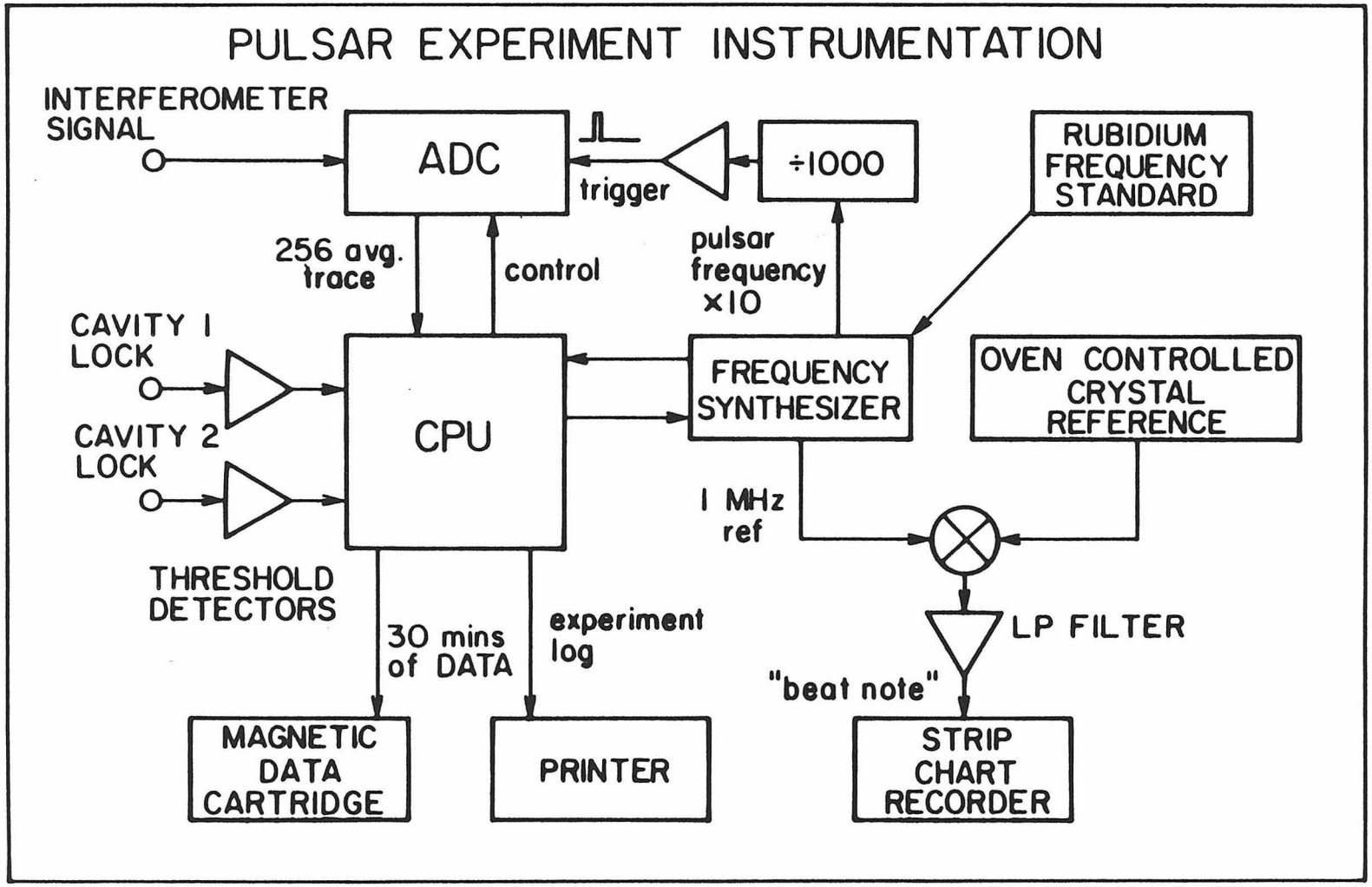

Figure 4.3. The data collection and timing instrumentation for the pulsar experiment. The signal input (at the top, left) is digitized and averaged by the ADC. The signal is averaged further in the CPU and written to magnetic tape every 30 minutes. A trigger developed from the synthesized pulsar frequency synchronizes the data collecting. The divide-by-1000 and trigger pulse-shaping are part of a larger circuit shown in Figure 4.5.

tape. The remaining 20 minutes were divided roughly as follows:

7.4 min	out of lock and other down time
5.7 min	ADC to CPU transfer time
4.5 min	ADC time to compute average
1.3 min	excess time between trigger pulses
.3 min	tape I/O

The inefficiency is essentially all due the limitations of the available instrumentation. Three factors contribute the bulk of the unused time. Each time the interferometer went out of lock, an average of 15 seconds of data were discarded. This accounts for over 5 minutes of the "out of lock and other down time" entry in the list above. (The remaining time in that entry represents an average of two hours a day spent adjusting the interferometer. Nearly all of it was concentrated in the morning and evening when the temperature was changing most rapidly.)

Less averaging in the ADC would have cut this factor, but at the expense of an already large loss of time: time to transfer data from the ADC to the CPU. This transfer time is largely due to a delay of the ADC to respond to the CPU request for data, and not the actual transfer.

In addition, the ADC spent almost a third of its time, in between collecting .1 second traces, computing the average. The dead time caused by these features might have been avoided with more costly instrumentation of the experiment. The limit seems to be inherent in the HP-85A and HP-3285A combination.

4.3. Timing

The phase of the pulsar cycle had to be tracked to within about 1/10th of a cycle over the observation period of 4 days. To maintain the part in 10^{10} stability that this requirement implies, a rubidium vapor frequency standard (HP-5065A) borrowed from JPL.[1] The standard was adjusted 2 months before the experiment began and checked 2 weeks after at the Standards Lab at JPL.[2] The Standards Lab maintains two cesium clocks (HP-5061A) with daily corrections at the level of 1 μsec based on published and broadcast NBS time. In addition, the rubidium standard was compared both shortly before and after the experiment against a WWVB receiver in our own lab. For all four tests, the standard was found to be within a part in 10^{10} of the reference. For the duration of the observation period, the rubidium clock was assumed to be accurate provided its own "continuous operation" indicator never failed. The indicator was proved operational in early tests when the clock was used to find an intermittently faulty power plug. After this was corrected, the clock ran continuously without failure until it was returned to JPL.

A frequency synthesizer (HP-3325A), phase-locked to the rubidium standard, provided a signal to the trigger generating circuitry. The CPU programmed the synthesizer with the changing 10 digit frequency at 15 minute intervals throughout the experiment. The output of the synthesizer was a piecewise linear approximation to the Doppler shifted pulsar phase. The phase was calculated to be at all times well within 1/10th of a pulsar cycle of the true phase. Because of the μHz resolution of the synthesizer and the 10 digit requirement on the frequency, I programmed the synthesizer with 10 times the pulsar frequency, ~6.4 kHz.

---

[1] Here, I gratefully acknowledge Julias Law of JPL for loaning me the clock.
[2] Thanks are due to Hunter S. McConnell for his time and expertise applied to the adjustment and checking of the clock.

The list of frequencies were calculated in advance and simply stored in CPU memory. The 10 digit accuracy required of the Doppler shifted frequencies proved to be less than trivial to come by. An available program, DOPSET,[3] was accurate to about 8 digits; it neglected planetary perturbations on the Earth's velocity. I developed a program to interpolate tables in The Astronomical Almanac (1983) and derive the velocity of the Caltech interferometer. After accounting for aberration and several coordinate changes, the relativistic Doppler shift was computed and applied to the pulsar frequency. Figure 4.4 shows the frequency as a function of time during the experiment.

After each .1 second time trace was digitized the ADC spent over .04 seconds to add it to the accumulating 1024 sample average trace; this accounts for 4.5 minutes of dead time in each 30 minutes of real time as described earlier. The total time per trace (~.14 sec) represents about 92 pulsar periods. For simplicity, trigger pulses were separated by 100 pulsar periods accounting for an inconsequential loss of efficiency in the face of the other losses; a total of about 1.3 minutes in each 30 is spent during the extra 8 pulsar periods of dead time. The trigger pulse was .5 μsec wide ($\ll$ ADC sample time). This was arranged to minimize the effect of the trigger (via crosstalk, pickup, or ground loop) on the ADC signal input.

4.4. Timing Verification and Monitoring

Since timing played such a key role in the experiment, several active tests of it were employed. To check for failure of the rubidium standard or phase lock of the synthesizer to the standard, a 1 MHz sinusoid generated by the synthesizer was mixed with a signal derived from an oven-controlled quartz crystal.

[3] I thank Mike Lessing, in the Astronomy department at Caltech, for helping me use this program on short notice.

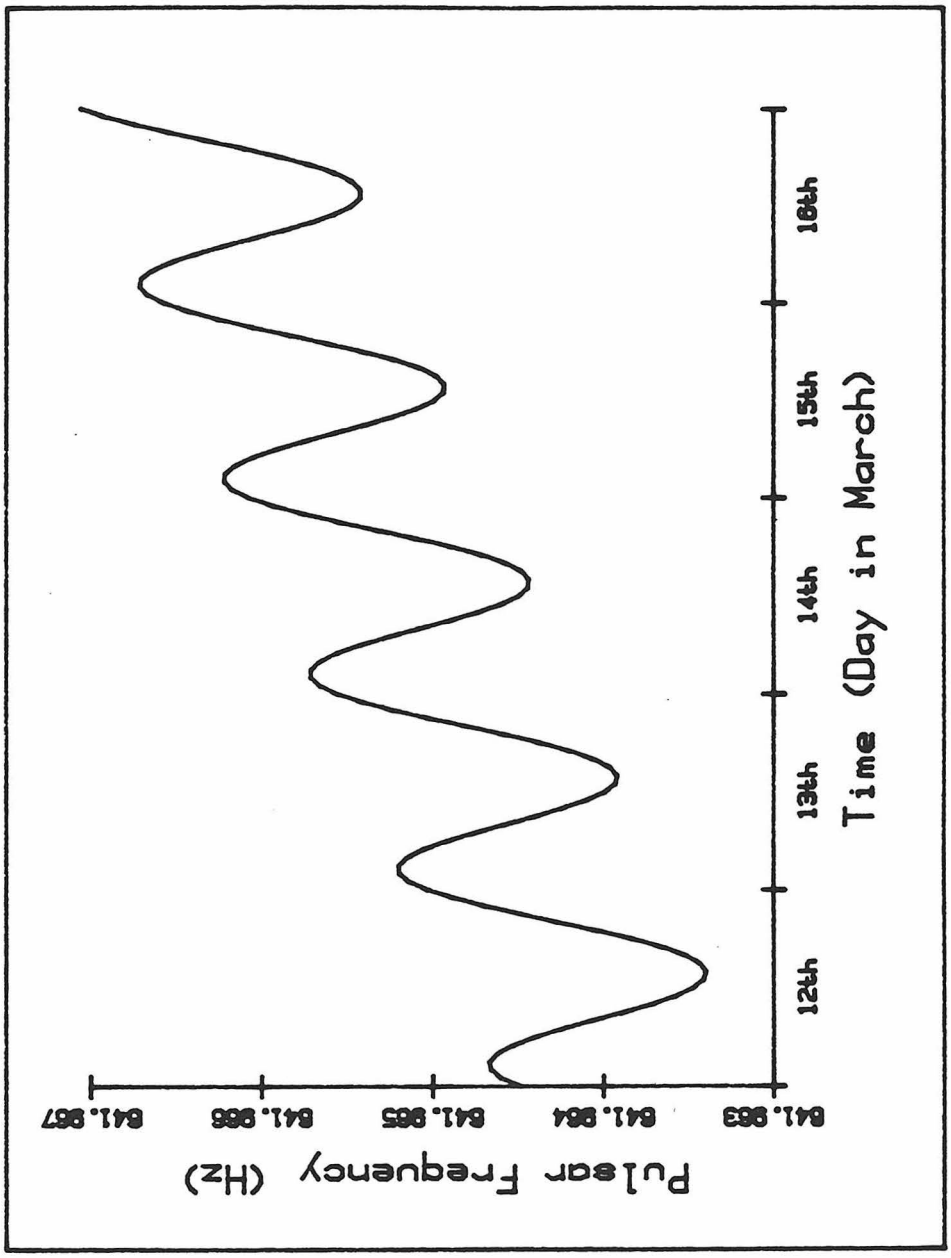

Figure 4.4. The Doppler shifted pulsar frequency during the observation period. The periodic variation is due to the daily rotation of the Earth. The secular increase of the frequency during the experiment is part of a larger periodic variation due to the Earth's orbit about the Sun.

The resulting beat note was recorded on a strip chart recorder for the duration of the experiment. The oven controlled crystal is specified to have a 5×10^{-8} accuracy, while the crystal in the synthesizer has an accuracy of 5×10^{-6}. If the standard failed or for some reason the synthesizer lost lock, the inaccuracy in its crystal would cause a noticeable change in the beat note. In addition to detecting such a failure, the strip chart might have been useful in correcting for it.

Every time the CPU changed the frequency of the synthesizer, the old value was read from the synthesizer and printed along with the new value and time of day. This provided a log which was compared with the computed frequencies to guarantee no CPU mishap. Additionally, if the synthesizer spontaneously reset or modified itself as is characteristic of faulty power connections, this would have shown up as an incorrect *old value* of the frequency.

The accumulated phase was monitored by a circuit (Figure 4.5) based on one used in the recent Glasgow search for the pulsar. At every one million (10^6) pulsar cycles (~24 min) the time in microseconds from the start of the observing period was saved in a register and displayed by a 12 digit LED array. The CPU periodically (~15 min) interrogated this register and printed its contents with the time of day for later perusal. To verify that the piecewise linear approximation to the Doppler shifted phase was sufficiently accurate, and to check that no timing errors occurred during the experiment, the times of million cycle zero-crossings were calculated using piecewise quartic approximation to the frequency table. The times recorded differed by no more than about 10 μsec from the *ideal* values calculated.

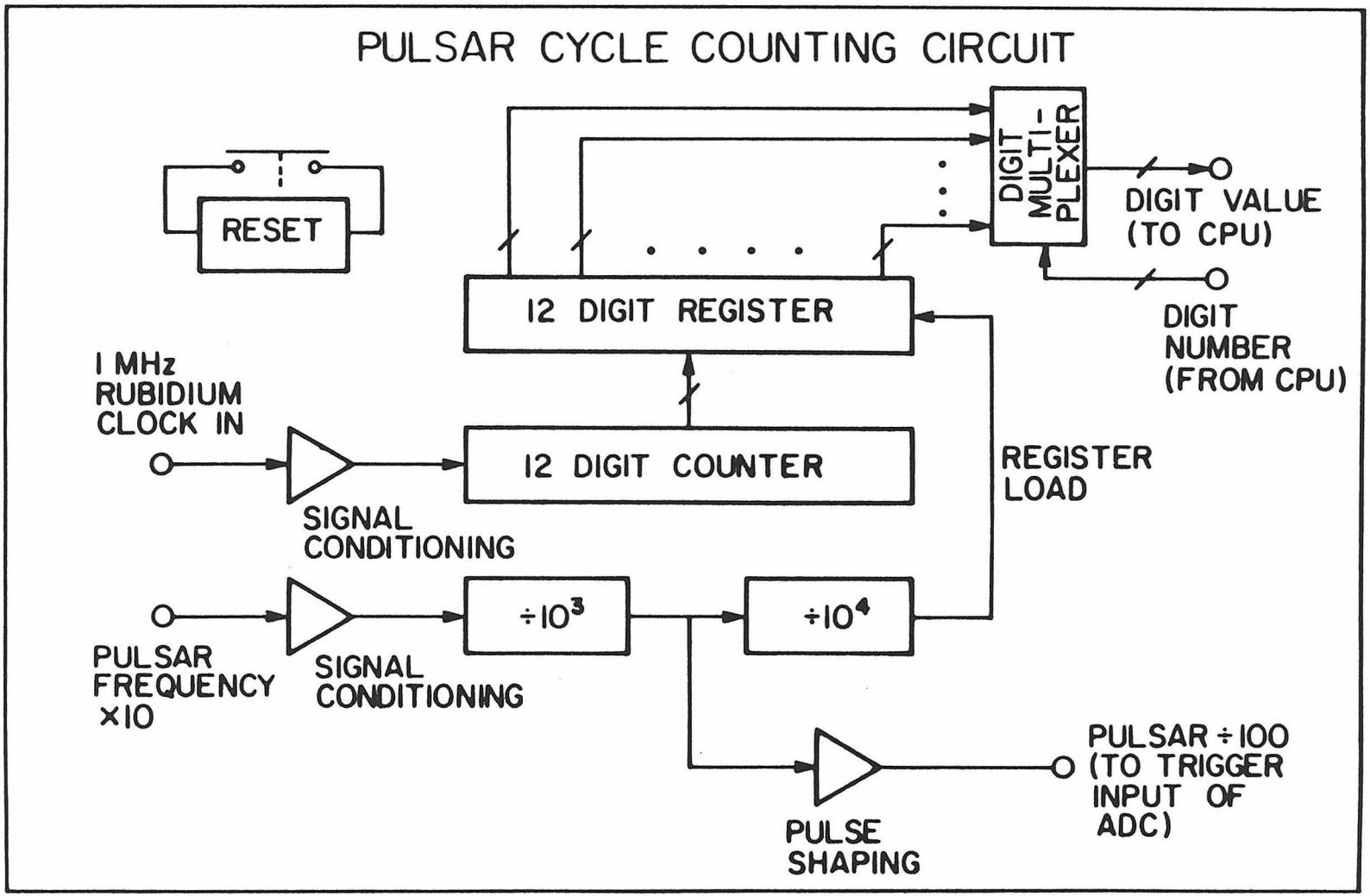

Figure 4.5. Timing verification circuit. Every millionth synthesized pulsar cycle triggers the "register load" line. The time in microseconds, as measured by the rubidium clock, is then saved in the register so that it can be read later by the CPU. Data averaging is synchronized by the trigger (generated at the bottom of the diagram).

Chapter 5
ANALYSIS

The average time traces stored every 30 minutes during the 4 day experiment were combined to give narrow band spectral information at the pulsar electromagnetic pulse frequency and its first harmonic. In the first section, I discuss the average time traces. From each stored record, I calculated the complex amplitude of the interferometer's motion at the pulsar frequency and its first harmonic. This involved a change of units from ADC volts to differential length change, as described in the previous chapter, and a calculation of the Fourier sine and cosine components. The Fourier component calculation was complicated by limitations of the speed and size of the HP-85 computer. An uncertainty for each complex amplitude was calculated. The second section describes the correction applied to account for the time dependent detector sensitivity to each of the two gravitational radiation polarizations. I explain in the third section the calculation of Fourier components in narrow frequency bands centered at each pulsar frequency. Finally, in the last section, a check of the data reduction is described. The results from the test verify that the programs all worked as designed.

5.1. Records from Tape

Each record on tape contains the data collected in 30 minutes in the form of a 1024 sample average time trace 0.1 seconds in length. In addition, each record includes the time and date that the record was written, the number of 256 average traces from the ADC that were summed to get this trace, the sensitivity setting of the ADC, and the number of times either cavity fell out of lock during the 30 minutes.

Each time record, recall, is the sum of some number of 256 trace averages from the ADC. The sum was turned into an average by dividing each point in the 1024 sample trace by the number of traces in the sum. Then the 16 bit values were converted to volts with a factor which depended on the sensitivity setting of the ADC. Finally, the conversion from volts to meters of differential motion in the two arms of the interferometer was applied. (The factors entering into this last conversion were discussed in the previous chapter.) The result is a 1024 sample time record of the length difference, synchronized to the pulsar and averaged over a period of 30 minutes.

For each record I calculated the complex amplitude at the pulsar frequency and its first harmonic. Memory and speed limitations of the small desk-top computer used forced a clumsy calculation. Rather than multiply the 1024 sample vector by cosine and sine in the straightforward way, I folded it into a single 16 sample vector representing about 1 cycle of the fundamental. To account for the actual cycle length of 15.95 samples, cycles 22 to 42 were shifted by 1 before folding, cycles 43 to 63 by 2, and cycle 64 by 3. The resulting 16 sample vector was multiplied by sines and cosines at 641.9 Hz and 1283.9 Hz to get the complex amplitudes at each frequency. This correction for cycle length is imperfect. As shown at the end of this chapter, the effect is a ~2% reduction in magnitude at 642 Hz, and ~10% reduction at 1284 Hz.

To estimate the uncertainty in the complex amplitude I assumed that the voltage represented in each time record is given by

$$v_i = x_0\cos(2\pi f_0 t_i) + y_0\sin(2\pi f_0 t_i) + n_i + m \qquad (5.1)$$

where i is the sample index from 0 to 1023, f_0 is the pulsar fundamental, n_i is the noise component, and m is the mean (which might result from offsets in the electronics, etc.). The terms for the pulsar harmonics (less than the 2.5 kHz

bandwidth of the ADC) which should also appear in the above equation, have been left out for simplicity; they turn out to be as negligible as the fundamental. The mean square noise in this record is

$$\langle n_i^2 \rangle = \langle v_i^2 \rangle - m^2 - \frac{1}{2}(x_0^2 + y_0^2) \tag{5.2}$$

where $\langle\ \rangle$ means sum over i and divide by 1024, i.e. take the time average. Barring large quantities of gravitational radiation or pickup, $x_0^2 + y_0^2$ should be small. In fact it was negligible ($\ll 1\%$), leaving the usual variance.

The uncertainty in a quantity derived from these 1024 samples is related to the square root of the variance by the square root of the number of samples. For sine and cosine amplitudes, each is effectively using half of the 1024 samples. So, the uncertainty in the real and imaginary parts of the amplitude calculated above is given by

$$\sigma_i = \left[\frac{\langle n_i^2 \rangle}{512} \right]^{1/2} \simeq \left[\frac{\langle v_i^2 \rangle - m^2}{512} \right]^{1/2} \tag{5.3}$$

All told, 184 records spanning 94 hours make up the data collected for the experiment. Records were discarded if any one of the following applied:

1) empty record - number of ADC traces zero

2) cavity out of lock > 1000 times

3) ADC sensitivity neither 3V nor 10V

Eight records were discarded. Seven of these had one or both cavities out of control too many times. The remaining record was eliminated because the ADC sensitivity had been inadvertently left on an incorrect setting after a test. The

remaining 177 records combined to give 177 complex amplitudes separated by 2.96 μHz, or (94 hours)$^{-1}$, surrounding each of the pulsar related harmonics.

5.2. Polarization

Because of the changing orientation of the interferometer with respect to the pulsar, the detector's sensitivity is a function of both time and polarization.

To analyze this dependence I chose a coordinate system as follows (Figure 5.1). The $\hat{z}$ direction is aligned with the direction of propagation. The $\hat{y}$ unit vector lies in the plane containing the pulsar and the Earth's spin axis. It has a positive projection onto the spin angular momentum. The $\hat{x}$ direction is defined by the right hand rule.

In this coordinate system a convenient polarization basis for the gravitational radiation is defined by components of the metric perturbation in the transverse-traceless gauge (superscript TT):

$$h_{xx}^{TT} = -h_{yy}^{TT} = \mathbf{Re}[h_+ e^{-i\omega(t-z)}] \tag{5.4a}$$

$$h_{xy}^{TT} = h_{yx}^{TT} = \mathbf{Re}[h_\times e^{-i\omega(t-z)}] \tag{5.4b}$$

where ω is the radiation frequency, h_+ and $h_\times$ are complex amplitudes. The response of a quadrupole detector such as the Caltech interferometer to a sinusoidally time varying plane wave with unit strength is given by a complex number representing both the magnitude and the phase of the detector's output. If the two arms of the interferometer are directed along mutually orthogonal unit vectors, $\hat{H}$ and $\hat{L}$, then this response is given by

$$\begin{aligned} S &\equiv \frac{1}{2}(H_i H_j - L_i L_j)\, e_{Pij} \\ &= \frac{1}{2}u(H_x^2 - H_y^2 - L_x^2 + L_y^2) + v(H_x H_y - L_x L_y) \end{aligned} \tag{5.5}$$

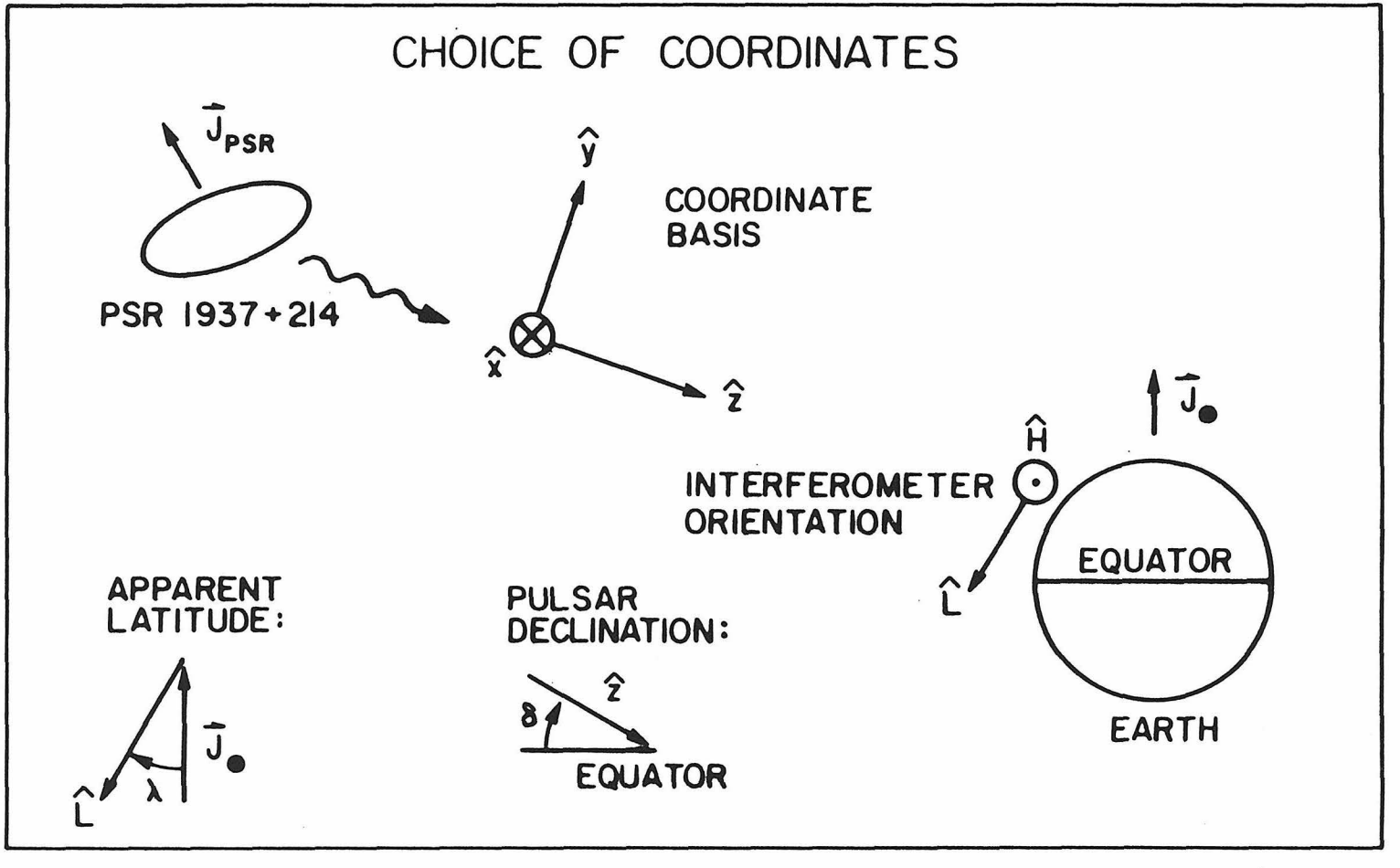

Figure 5.1. The coordinate basis in which the detector's polarization sensitivity was calculated. The z-axis points along the direction of propagation. The x- and y-axes are transverse to it.

where the non-zero components of the polarization tensor, e_P, are

$$e_{Pxx} = -e_{Pyy} = u \tag{5.6a}$$

$$e_{Pxy} = e_{Pyx} = v \tag{5.6b}$$

subject to the normalization condition

$$|u|^2 + |v|^2 = 1 \tag{5.7}$$

For the Caltech detector $\hat{H}$ points eastward and $\hat{L}$ points southward. In terms of the declination of the pulsar, δ, the apparent latitude of the detector, λ, and the phase of the Earth's rotation, φ, (φ=0 when the detector is closest to the pulsar), the response is

$$S = \frac{1}{2}u[\cos^2\delta\cos^2\lambda + 2\sin\delta\cos\delta\sin\lambda\cos\lambda\cos\varphi$$

$$+ \cos^2\varphi(1 + \sin^2\delta\sin^2\lambda) - \sin^2\varphi(\sin^2\delta + \sin^2\lambda)] \tag{5.8}$$

$$- v\sin\varphi[\cos\delta\sin\lambda\cos\lambda + \sin\delta\cos\varphi(1 + \sin^2\lambda)]$$

Figure 5.2 shows the Caltech detector sensitivity for the two cases (u,v)=(1,0) and (0,1) corresponding to "plus" and "cross" polarization respectively.

These two response functions were used to compute separately the gravitational radiation amplitude for each polarization. This was possible with our single detector because of the orthogonality of the response functions for the independent polarizations and the fact that our observation period uniformly spanned an essentially integral number of days.

Assuming first a "plus" polarization (i.e., u=1,v=0) the complex amplitudes (x_i = real part, y_i = imaginary part) and uncertainties computed for each 30

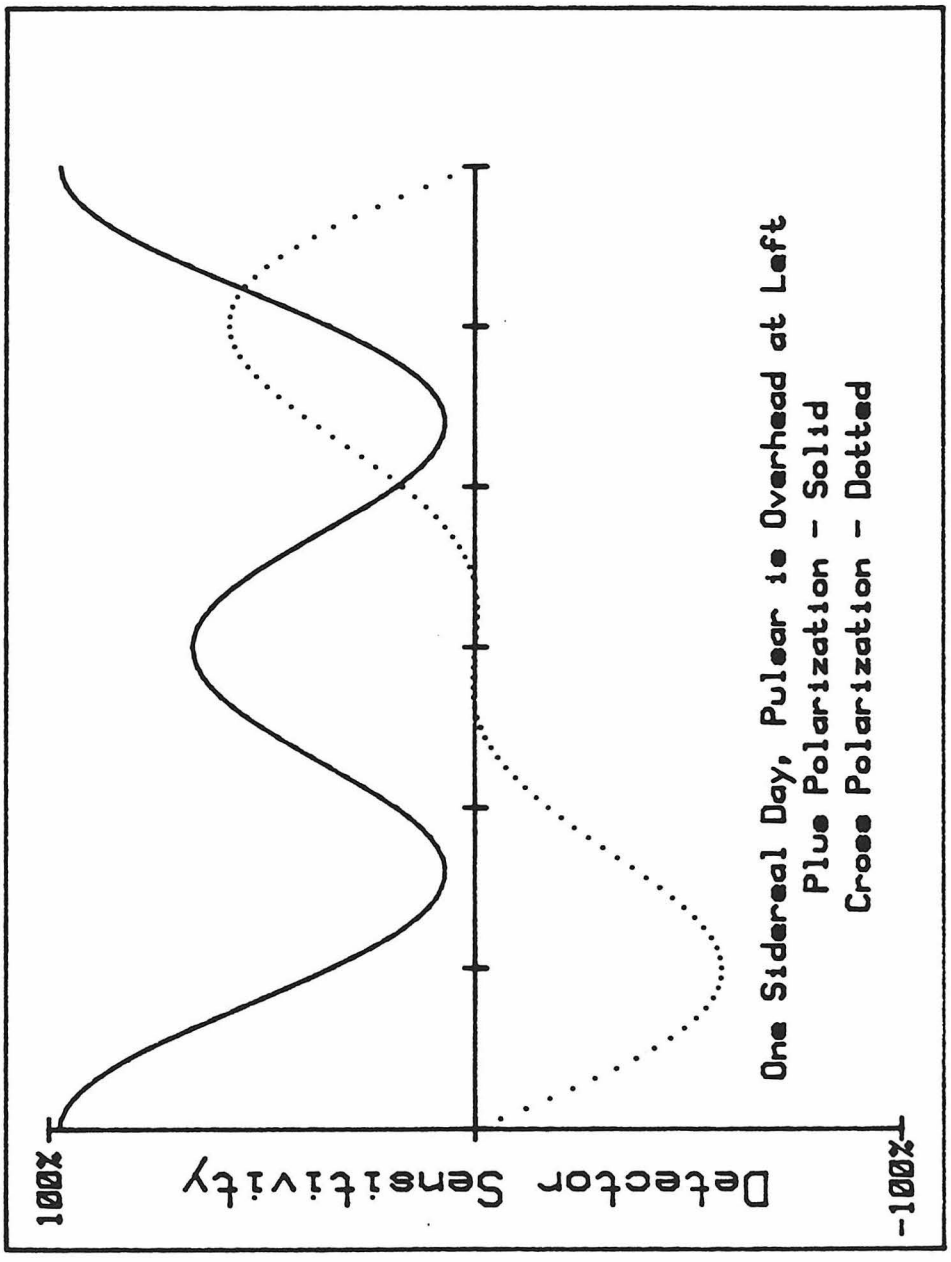

Figure 5.2. The sensitivity of the detector to each gravitational radiation polarization as a function of time. The plot starts with the pulsar overhead, as shown in Figure 5.1. The center of the plot is 12 sidereal hours later with the detector on the other side of the Earth.

minute tape record were divided by the response:

$$x_i \pm \sigma_i \quad \rightarrow \quad \tilde{x}_i \pm \tilde{\sigma}_i \equiv \frac{x_i}{S(t)} \pm \frac{\sigma_i}{S(t)} \tag{5.9}$$

and likewise for $\tilde{y}_i \pm \tilde{\sigma}_i$, where i is the record index. This can be thought of as a change of units from differential strain *in the detector orientation* to differential strain *in the x, y, z coordinates*. This conversion was carried out for the "cross" polarization response function as well.

5.3. Fourier Components

Consider a particular polarization at one of the pulsar harmonics, say "plus" polarization at the fundamental (~642 Hz). The 177 complex amplitudes corrected for polarization response represent the alleged gravity wave signal in a .6 mHz or $(30\ \text{min})^{-1}$ bandwidth centered at the pulsar fundamental. This time domain representation can be transformed to give 177 complex frequency domain amplitudes separated by 2.96 μHz, or $(94\ \text{hours})^{-1}$. If

i is the vector index from 0 to 176

t_i the time the i^{th} vector was measured

$\tilde{x}_i$ real part, corrected for polarization

$\tilde{y}_i$ imaginary part of same

$\tilde{\sigma}_i$ the uncertainty in either part, and

n is the Fourier frequency index from -88 to 88

then

$$\begin{bmatrix} X_n \\ Y_n \end{bmatrix} = \tilde{\sigma}^2 \sum_{i=0}^{177} \frac{1}{\tilde{\sigma}_i^2} \begin{bmatrix} \cos(2\pi n f_* t_i) & -\sin(2\pi n f_* t_i) \\ \sin(2\pi n f_* t_i) & \cos(2\pi n f_* t_i) \end{bmatrix} \begin{bmatrix} \tilde{x}_i \\ \tilde{y}_i \end{bmatrix} \tag{5.10a}$$

$$\frac{1}{\tilde{\sigma}^2} = \sum_{i=0}^{177} \frac{1}{\tilde{\sigma}_i^2} \qquad (5.10b)$$

where $f_* = (94 \text{ hours})^{-1}$.

Equation 5.10 was applied to each polarization at the fundamental pulsar frequency and at the first harmonic. The four resulting Fourier transforms will be discussed in the last chapter.

5.4. Numerical Calibration

The ADC represents voltages with 16 bit binary numbers. This representation was calibrated for the two ADC sensitivities used during the data collection: 3V and 10V. Known square and sinusoidal waveforms at various frequencies and amplitudes were digitized and checked. The calibration factors obtained were consistent to within 1 percent.

After this calibration was established, the data analysis programs were checked (except for polarization corrections) by analyzing a numerical signal as if it had come from the data tapes. The waveform analyzed was, in units of volts:

$$v(t) = \text{sawtooth}[(f_0 + 45 f_*)t] + \text{sawtooth}[(2f_0 - 30.5 f_*)t] \qquad (5.11)$$

where $f_0 \simeq 642$ Hz is the fundamental pulsar frequency, and $f_* = 2.96\ \mu$Hz is the frequency resolution for 94 hours of observing time. The "sawtooth" function is a 2 volt peak-to-peak waveform given by

$$\text{sawtooth}(x) \equiv 2 * (\text{fractional part of } x) - 1 \qquad (5.12)$$

where $x \geq 0$ is in cycles. A simple Fourier analysis gives numbers to compare to the "measured" ones. The comparison is shown in Table 5.1.

Numerical Calibration Check			
Frequency	Expected	Measured	% Error
f_0+45f_*	.637	.623	-2
$2f_0+90f_*$	.318	.286	-10
$2f_0-31f_*$	.405	.375	-7
$2f_0-30f_*$	.405	.375	-7

Table 5.1

As can be seen in Figure 5.3 and Table 5.1 the results are as expected. The slight reduction of the magnitudes is a systematic effect introduced by the calculation of the complex amplitudes from each time record as discussed earlier in this chapter. It is insignificant in the present experiment. The phase shifts (not shown) that accompany the magnitudes are roughly 10° for 642 Hz components and 25° for 1284 Hz components. In making comparisons between the data described in the next chapter and pulsar models or electromagnetic pulse data these phases might be important. They do not enter in placing an upper limit on gravitational radiation from PSR 1937+214.

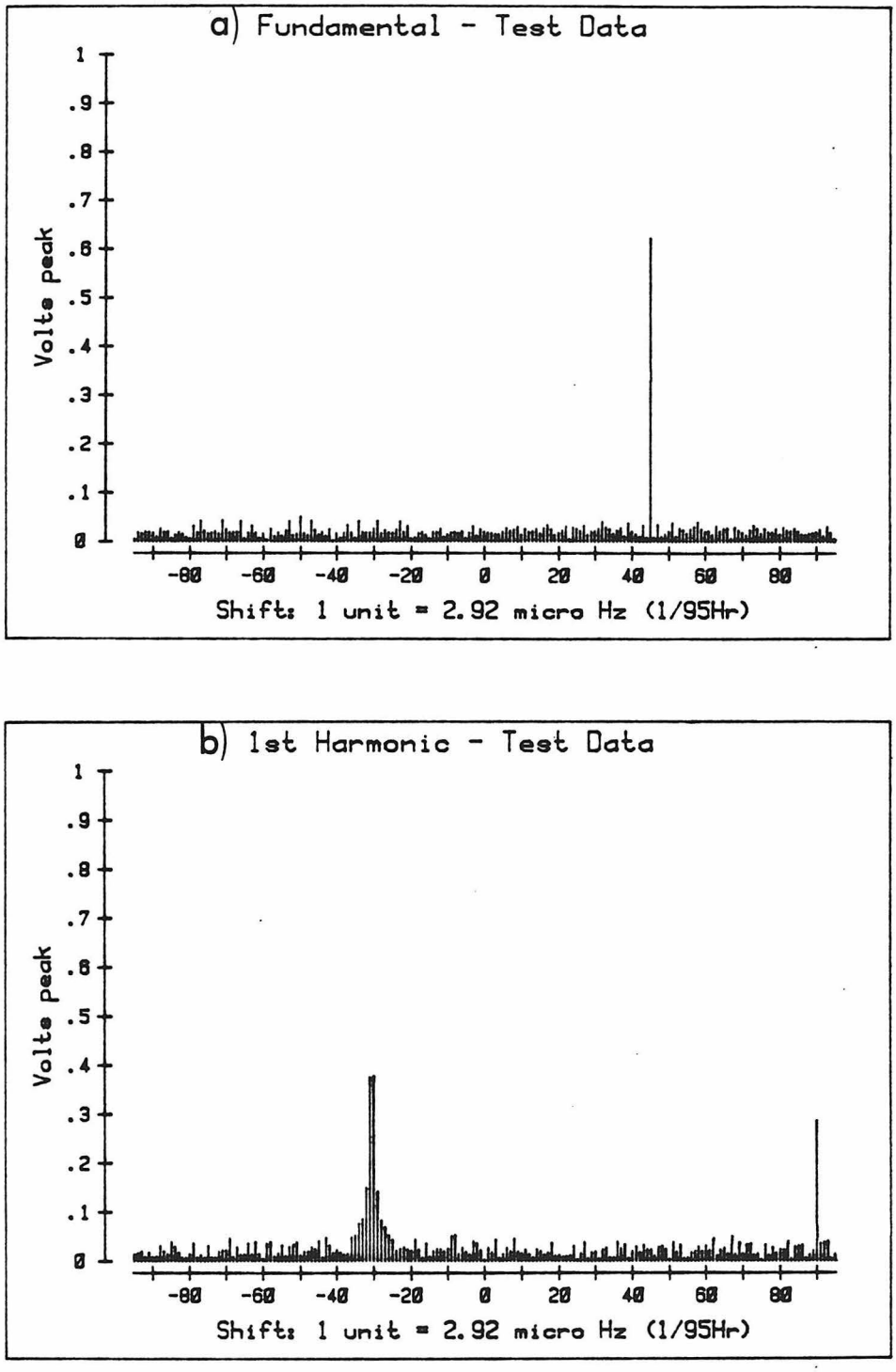

Figure 5.3. The results of test data analysis. The test "signal" was composed of two sawtooth waveforms. The sawtooth near the pulsar fundamental has components near the fundamental (a) and its harmonic (b). The sawtooth near the pulsar harmonic (b) fell between frequency bins; it was resolved symmetrically into adjacent bins.

Chapter 6

RESULTS AND CONCLUSIONS

In this chapter I first give a short overview of the running of the experiment, focusing on the long term stability of the cavity alignment and the steps taken to keep the interferometer locked. In the second section I describe the results of the data analysis and place a polarization dependent upper limit on the gravitational wave strain amplitude. The third section contains an application of the predictions for gravitational radiation from an axisymmetric freely precessing neutron star given by Zimmerman and Szedenits. It is an example of how the data from an experiment like this one could be used to determine some of the physical parameters of a pulsar and its precessional motion.

6.1. The Run

The antenna output was monitored from 17:33 PST on March 12, 1983 to 15:30 on March 16. During the 94 hour experiment, 1.2×10^5 seconds of data were collected. I stayed with the detector for the entire four days. The other members of the group took turns so that there were two of us present at all times. The occasional adjustments of the optics to compensate for drifts (chiefly induced by temperature changes) were typically very minor, taking a single person a few minutes. A small adjustment of the second mode matching lens to reoptimize the fringe visibilities of the two cavities usually sufficed. On occasion the adjustment was slightly more involved, taking two people 10 to 80 minutes. These "major" adjustments were necessitated by the relatively large temperature changes that occurred in the morning and the evening.

The temperature changes, which were most extreme during the morning and late evening, caused mirror mounts, the laser frame, and the 40-meter

vacuum pipes to expand and contract. The number of affected elements as well as the disparate time constants associated with each can make manual compensation (by adjusting mirror mount screws) less than trivial.

During the first 24 hours of the run the temperature in the laboratory was particularly stable because of the prevailing overcast weather. The air conditioning was also probably more efficient because of the small load on the chilled water supply during the weekend. The diurnal temperature excursion was $\lesssim 1°$ C at the corner of the lab. The warming trend that followed led to a larger temperature difference ($\gtrsim 2°$) between night and day. During the last ~24 hours of observing I periodically adjusted the thermostats in each arm of the detector to compensate for the effectively low "loop gain" of the air conditioning system. I was able to stablize the temperature to within a degree.

The effect of these temperature variations is clearly evident in the quality of the data collected (Figure 6.1). Shown are the magnitudes of the 642 Hz Fourier component in each tape record stored during the run. They've been corrected for detector response to the "plus" polarization and weighted by the mean square fluctuation as described in Chapter 5. Ignoring the polarization correction, it is evident that the first and last days of data will contribute more to the final result than the intervening two days.

Several effects determined the stability of the lock. Increased demand on the campus chilled water supply during the hot hours of the day reduced the efficiency of both the air conditioning and the laser cooling water heat exchanger. In addition to the changes in alignment, the thermal drifts caused longitudinal mode hops in both the laser and free mass cavities. Each mode hop, lasting for a fraction of a second, resulted in an average of 15 seconds of contaminated data being discarded.

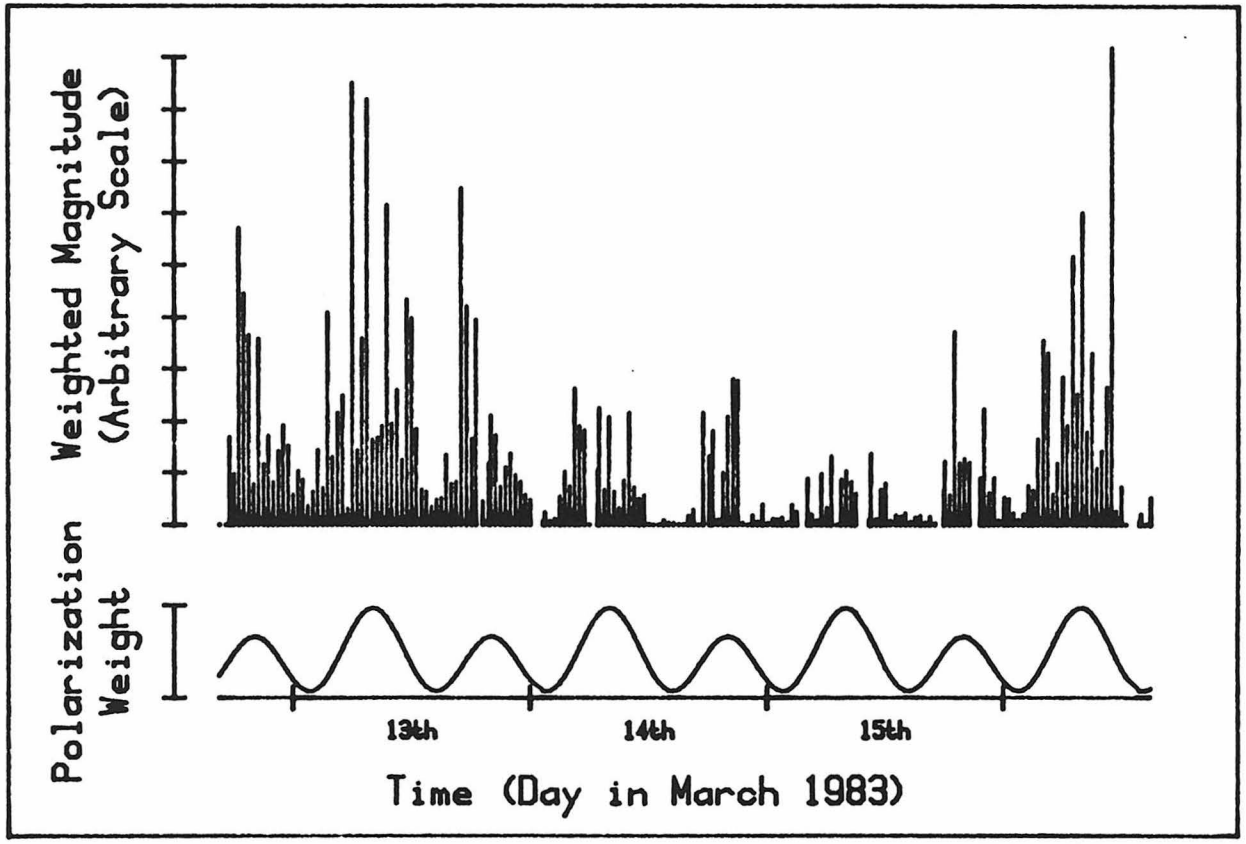

Figure 6.1. The weighted magnitudes, corrected for "plus" polarization. The weighted magnitudes are noticeably larger during the first and last days of the experiment than during the intervening days.

During the four day observing period adjustments taking from 10 to 80 minutes were performed once or twice a day. Quick adjustments taking from 1 to 5 minutes were made every 2 to 8 hours. These adjustment periods all contributed to the *down time* during which data was lost. The chief contribution was caused by one or both cavities falling out of lock. During thermally stable and environmentally quiet times the lock was lost once every 20 to 80 minutes, typically for less than a few seconds (Figure 6.2). But, during less ideal intervals the lock was lost as often as every couple of minutes (Figure 6.3). Although the out-of-lock time was only milliseconds to seconds, the data being averaged in the ADC could not be separated from the contaminating out-of-lock data with the available hardware. As much as a 30 seconds of data were discarded each time.

6.2. Results

Four spectra representing the signal magnitude as a function of frequency and polarization at the pulsar fundamental and first harmonic were calculated from the data collected (Figures 6.4 and 6.5).

I first wanted to rule out any obvious errors in the analysis or data collection. Over the narrow frequency bands shown in the figures, I expected to see a roughly "white" noise background with possible peaks representing gravitational radiation from the pulsar. These peaks could show up in any of the four spectra and at frequencies other than the center, depending on the dynamics of the source as indicated in Chapter 3.

For each spectrum I plotted the amplitudes of all frequency components in the complex plane - a dot for each point in the transform. The scatter looked Gaussian. It was well centered at the origin and there were no obvious correlations between magnitude and phase. The computed mean and standard deviation for the real and imaginary parts of each plot (Table 6.1), show that the two

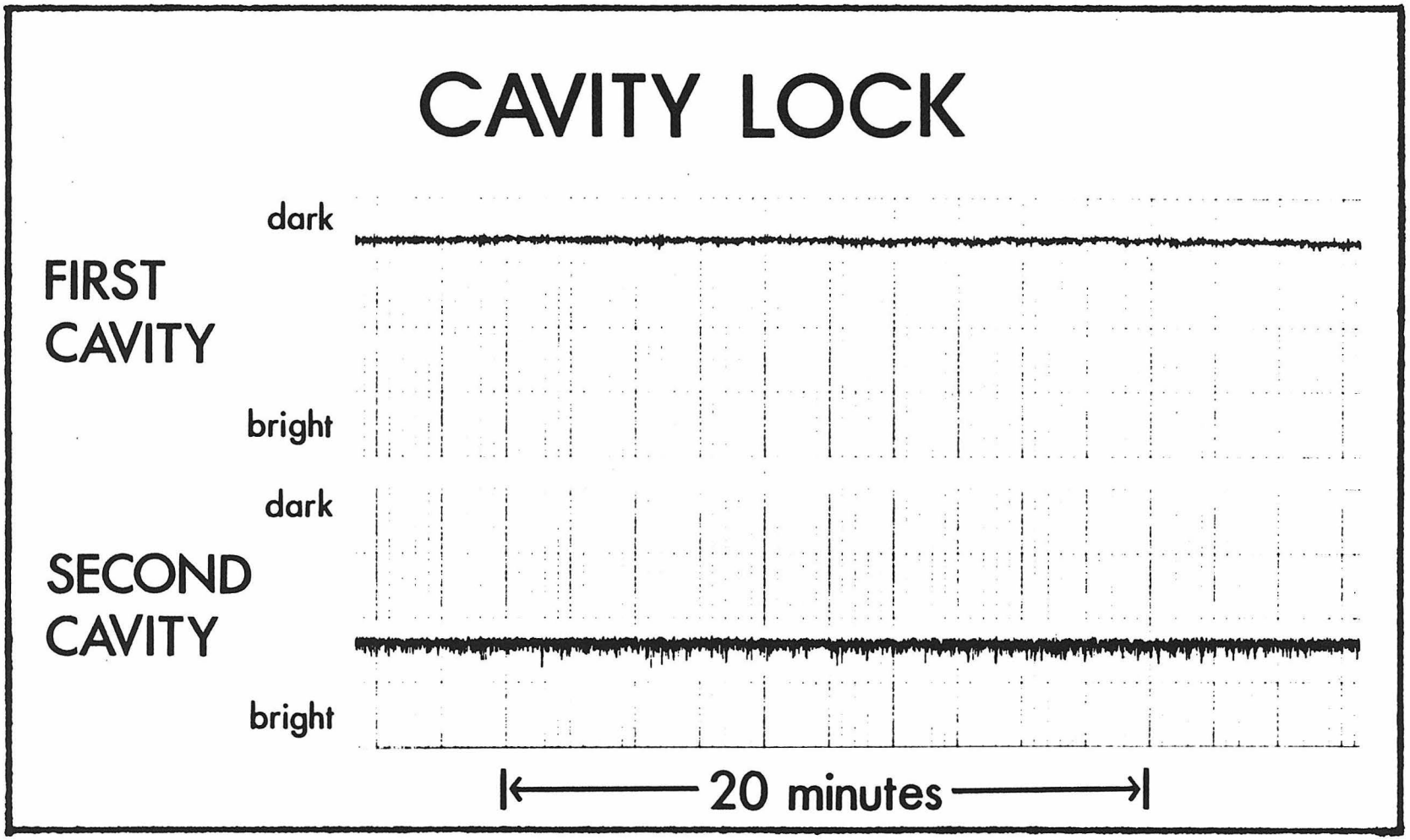

Figure 6.2. An example of both cavities remaining in resonance without interruption. The reflected light intensity from each cavity is maintained at a minimum (toward dark) by the feedback loops. The line thickness is due to low frequency changes in the orientations of the test masses.

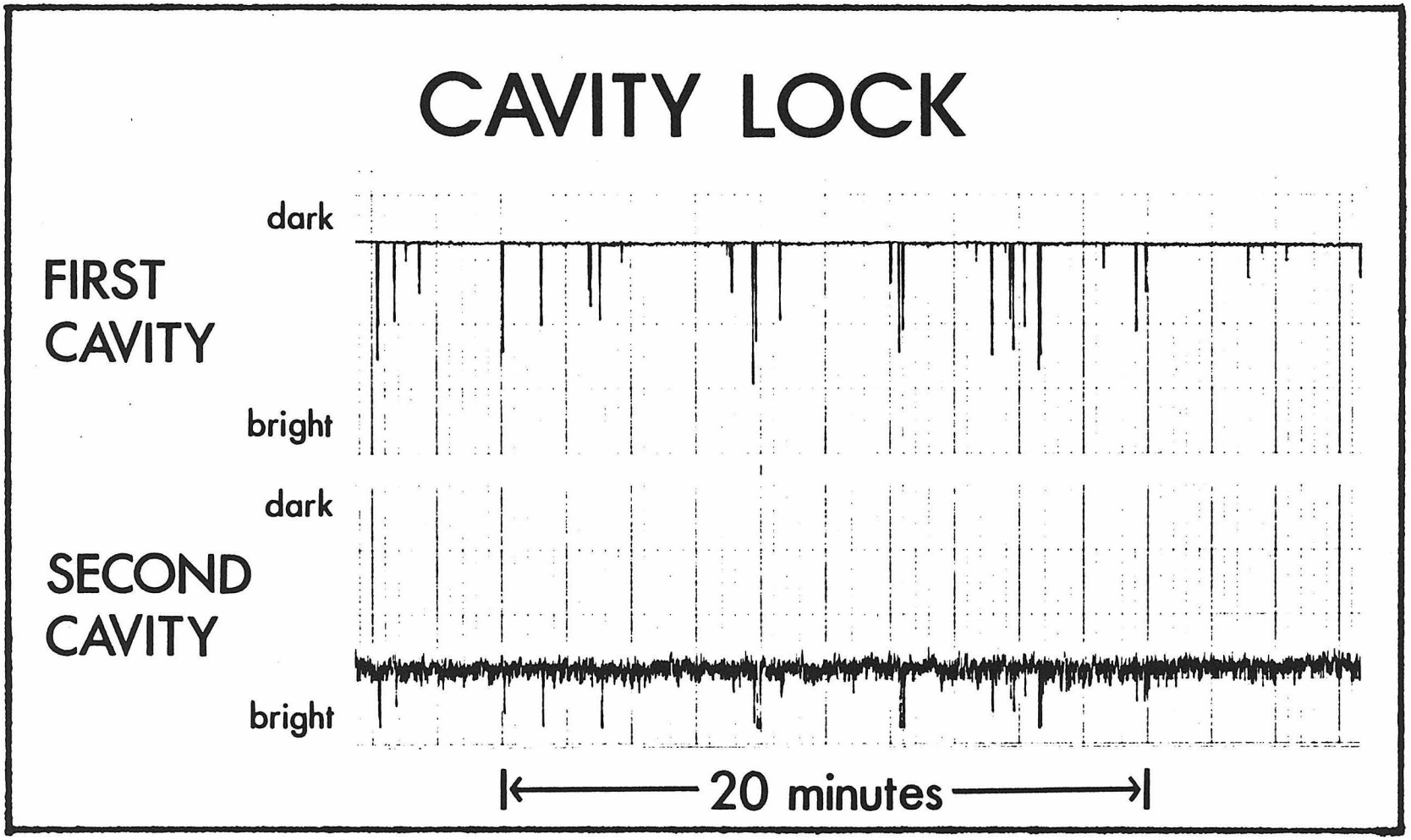

Figure 6.3. An example of the cavities falling out of resonance regularly. Each time lock is lost in either cavity, the reflected light intensity increases momentarily (toward bright). The servo loop usually reacquires lock within a fraction of a second, bringing the intensity back to a minimum. Each dropout caused as much as 30 seconds of data to be lost.

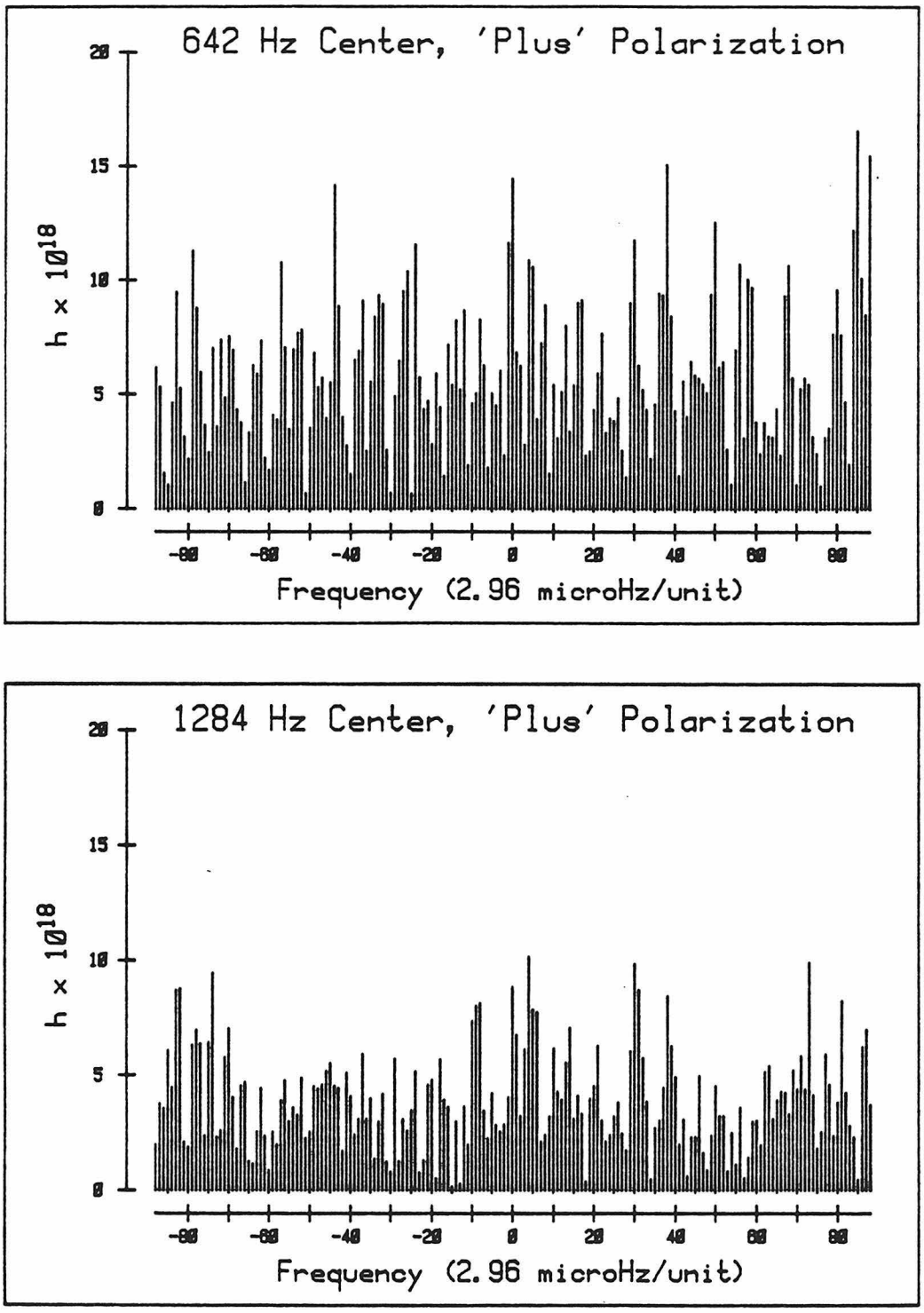

Figure 6.4. The dimensionless strain amplitude spectra for "plus" polarization. The frequency axes are labeled in units of inverse duration of the experiment. The top spectrum is centered at the electromagnetic pulsation frequency of the pulsar. The bottom is centered at the first harmonic.

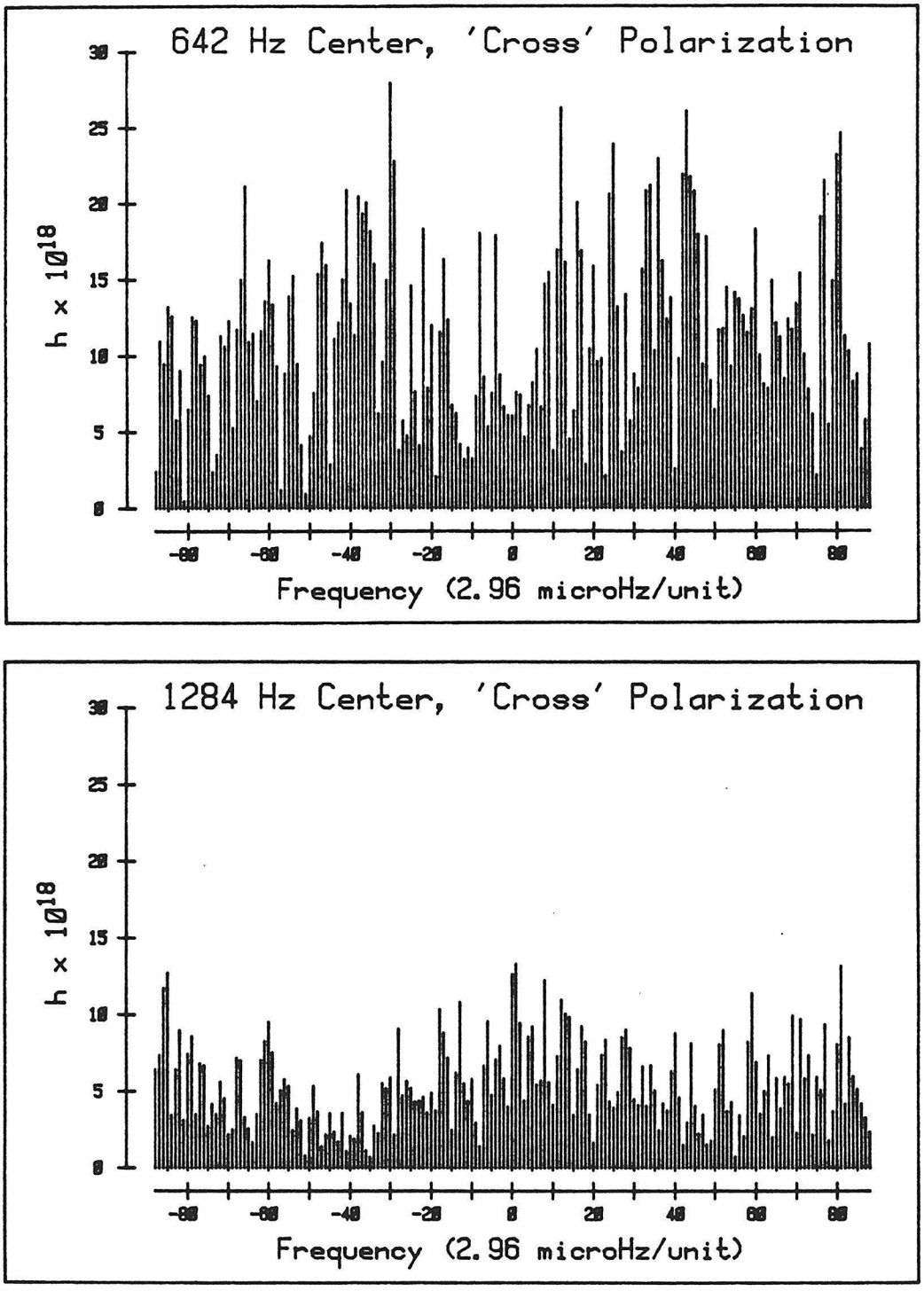

Figure 6.5. The dimensionless strain amplitude spectra for "cross" polarization. The frequency axes are labeled in units of inverse duration of the experiment. The top spectrum is centered at the electromagnetic pulsation frequency of the pulsar. The bottom is centered at the first harmonic.

standard deviations for the real and imaginary parts are equal to within statistical error. This is an indication that the distribution is independent of phase.

Mean and Std. Dev. of the Fourier Components in Units of Dimensionless Amplitude				
Center f	642 Hz		1284 Hz	
Polarization	+	×	+	×
$\overline{\mathrm{Re}}\times10^{20}$	2.8	-24.	16.	-7.6
$\sigma_{\mathrm{Re}}\times10^{18}$	4.6	8.4	3.1	4.4
$\overline{\mathrm{Im}}\times10^{20}$	.016	5.3	6.8	-6.2
$\sigma_{\mathrm{Im}}\times10^{18}$	4.8	9.7	3.2	4.3
$\bar{\sigma}\times10^{18}$	4.7	9.1	3.2	4.4
$(\tilde{\sigma}\times10^{18})$	4.6	7.4	2.5	4.1

Table 6.1

The uncertainty represented by $\bar{\sigma}$, the mean of σ_{Re} and σ_{Im}, is consistent with the variance used to weight the time domain data. That is, $\bar{\sigma} \simeq \tilde{\sigma}$, where $\tilde{\sigma}$ is given by equation 5.10. Failure of this condition might indicate that neglecting the sinusoidal contributions to $\tilde{\sigma}$ in equation 5.2 wasn't valid after all.

The magnitude distributions shown in Figures 6.6 and 6.7 compare well with the theoretical curves. Assuming that the distribution of complex amplitudes is Gaussian, in both real and imaginary parts, with variance $\bar{\sigma}^2$ and negligible offset from the origin, the magnitude distribution is given by the Rayleigh distribution

$$P(r) = \frac{r}{\bar{\sigma}^2} e^{-\frac{r^2}{2\bar{\sigma}^2}} \tag{6.1}$$

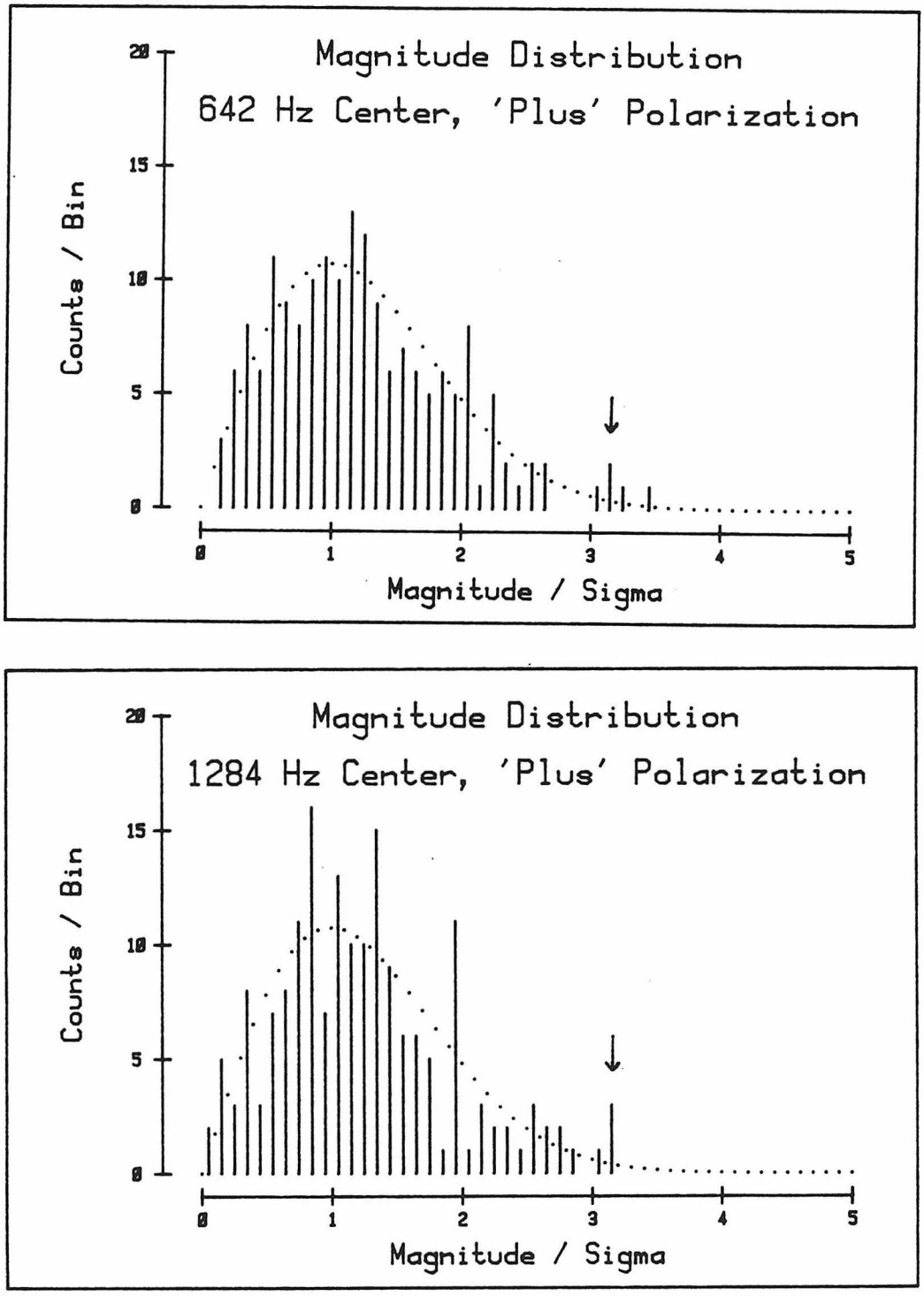

Figure 6.6. The measured and theoretical magnitude distributions for the "plus" polarization amplitude spectra in Figure 6.4. The magnitudes have been normalized to the values for σ in Table 6.1. The magnitude at zero-shift has been identified with an arrow.

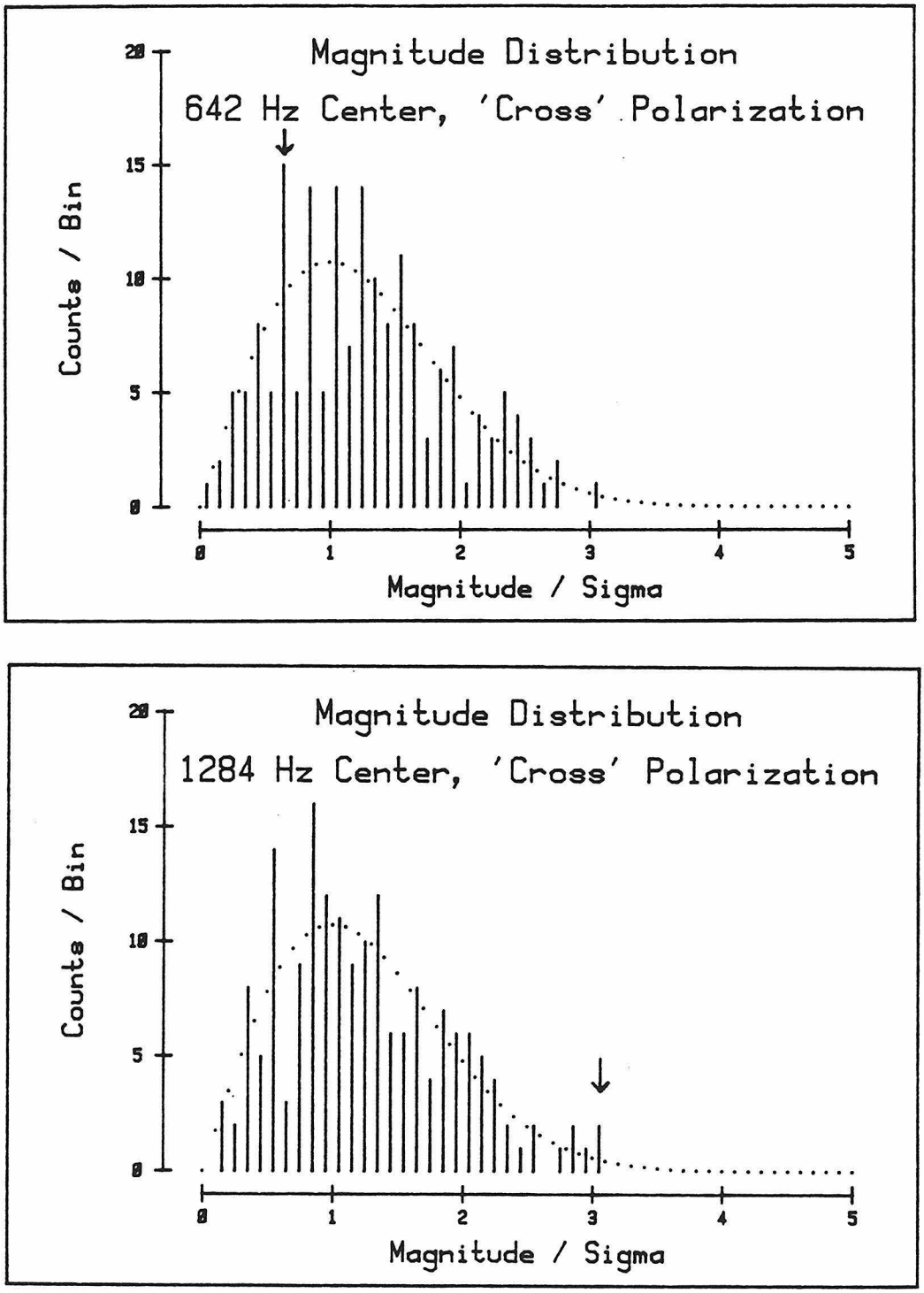

Figure 6.7. The measured and theoretical magnitude distributions for the "cross" polarization amplitude spectra in Figure 6.5. The magnitudes have been normalized to the values for σ in Table 6.1. The magnitude at zero-shift has been identified with an arrow.

where r is the magnitude. Monte Carlo simulations of the magnitude distribution exhibit similar fluctuations from the theoretical curve. This suggests that the spectra are in fact the result of a random process which can be taken to be "white" in the narrow band surrounding each center frequency.

Several of the peaks in each spectrum have confidence levels of ~99%. (I use confidence level to mean to the "central confidence level": the probability that the magnitude will be *less than* the given value.) But, as was demonstrated by the Monte Carlo simulations, they are quite likely within the statistics. There is no compelling evidence for gravitational radiation, or any other systematic source of large amplitude signals (i.e. ground loops, pickup, etc.).

I carried the analysis a little further by assuming that the gravitational radiation signal was at the center frequency in each spectrum. Several ways in which the frequency of emitted gravitational radiation could be different from a multiple of the electromagnetic pulse frequency were discussed in Chapter 3: shift by precession rate, splitting due to triaxial mass distribution, or Wagoner's equilibrium of radiation losses with spin-up by accreting matter. Other mechanisms may exist. But, without a specific model for PSR 1937+214, or an outstanding candidate peak, little can be done except assume the simplest possibility: zero shift.

The zero-shift amplitudes are given as magnitude and phase in Table 6.2. The "raw" phases for the 642 Hz amplitudes can be compared to one another, as can the phases for the 1284 Hz components. But, they have not been corrected for systematic phase shifts which make the 642 Hz phases incompatible with the 1284 Hz phases and both incompatible with electromagnetic pulse data. Among the corrections left out are: 1) the phase shift introduced by the fold-and-shift calculation of the complex amplitudes for each time record, 2) a phase shift introduced by the loop gain of the second arm, and 3) the arbitrary initial phase

Center Frequency Amplitudes and Gravitational Radiation Upper Limits				
Center f	642 Hz		1284 Hz	
Polarization	+	×	+	×
Magnitude ($h\times10^{18}$)	14.4	6.08	8.83	12.7
Raw Phase (deg)	-12	146	34	-163
Confidence (%)	99.1	20.2	97.9	98.6
99.7% Limit ($h\times10^{18}$)	16.1	30.9	10.8	14.8

Table 6.2

of the generated pulsar phase.

A 99.7% confidence limit to the gravitational radiation from the pulsar is set by integrating equation 6.1 using the values for $\bar{\sigma}$ in Table 6.1. The bottom line of Table 6.2 gives these limits.

Confidence levels for the zero-shift magnitudes are given in the table, also. Looking at them it seems possible that the center frequencies may have gotten more than their fair share of low probability amplitudes. To test this I computed the joint magnitude probability given by the 8-dimensional analog to the Rayleigh distribution

$$P(\rho) = \frac{\rho^7}{48} e^{-\frac{\rho^2}{2}} \tag{6.2}$$

where ρ is the dimensionless magnitude in the 8-dimensional space of 4 complex amplitudes (one for each combination of polarization and pulsar harmonic)

$$\rho^2 \equiv \sum_{642,1284} \sum_{+,\times} \left[\left[\frac{\overline{\mathrm{Re}}}{\sigma_{\mathrm{Re}}} \right]^2 + \left[\frac{\overline{\mathrm{Im}}}{\sigma_{\mathrm{Im}}} \right]^2 \right] \tag{6.3}$$

To combine amplitudes from spectra with different center frequencies, I used harmonically related shifts. That is, the amplitudes at a shift of +9 (or $\sim 26\,\mu$Hz) from a center frequency of 642 Hz for each polarization where combined with the amplitudes at a shift of +18 from the center frequency of 1284 Hz. The factor of two in the shift restricted the number of frequency components from 177 to 89. Figure 6.8 (top) shows ρ as a function of shift from the fundamental. In this light, the zero shift amplitudes appear to be more significant; the magnitude corresponds formally to a confidence level of $\gtrsim 99.8\%$. Figure 6.8 (bottom) compares the observed probability distribution to the theoretical distribution given by equation 6.3. Likewise, in Figures 6.9 and 6.10, I compared amplitudes with harmonically related shifts plus or minus one frequency bin (i.e. +9 from 642 Hz was compared separately to +19 and +17 from 1284 Hz). Again, there is no obvious indication that the theoretical curve provides an inconsistent description of the bulk of the distribution.

I then checked the sensitivity of the previously mentioned measurement made by the Glasgow group (Hough, et al. 1983) to the polarization implied by the zero shift amplitudes at 1284 Hz. Coincidentally, the polarization was remarkably close to a null in their sensitivity! The null was a result of a fortuitous cancellation of the response of the detector over the eight hours of their data collection. A smaller averaging time would have exposed a peak as large as the the one in my data without the cancellation. The data tapes were subsequently reanalyzed[1)] in smaller chunks and showed no sign of the peak. This removed all likely possibility that the peak was due to gravitational radiation.

[1)] I gratefully acknowledge Harry Ward and Andrew Munley for reanalyzing the data and providing me with the results.

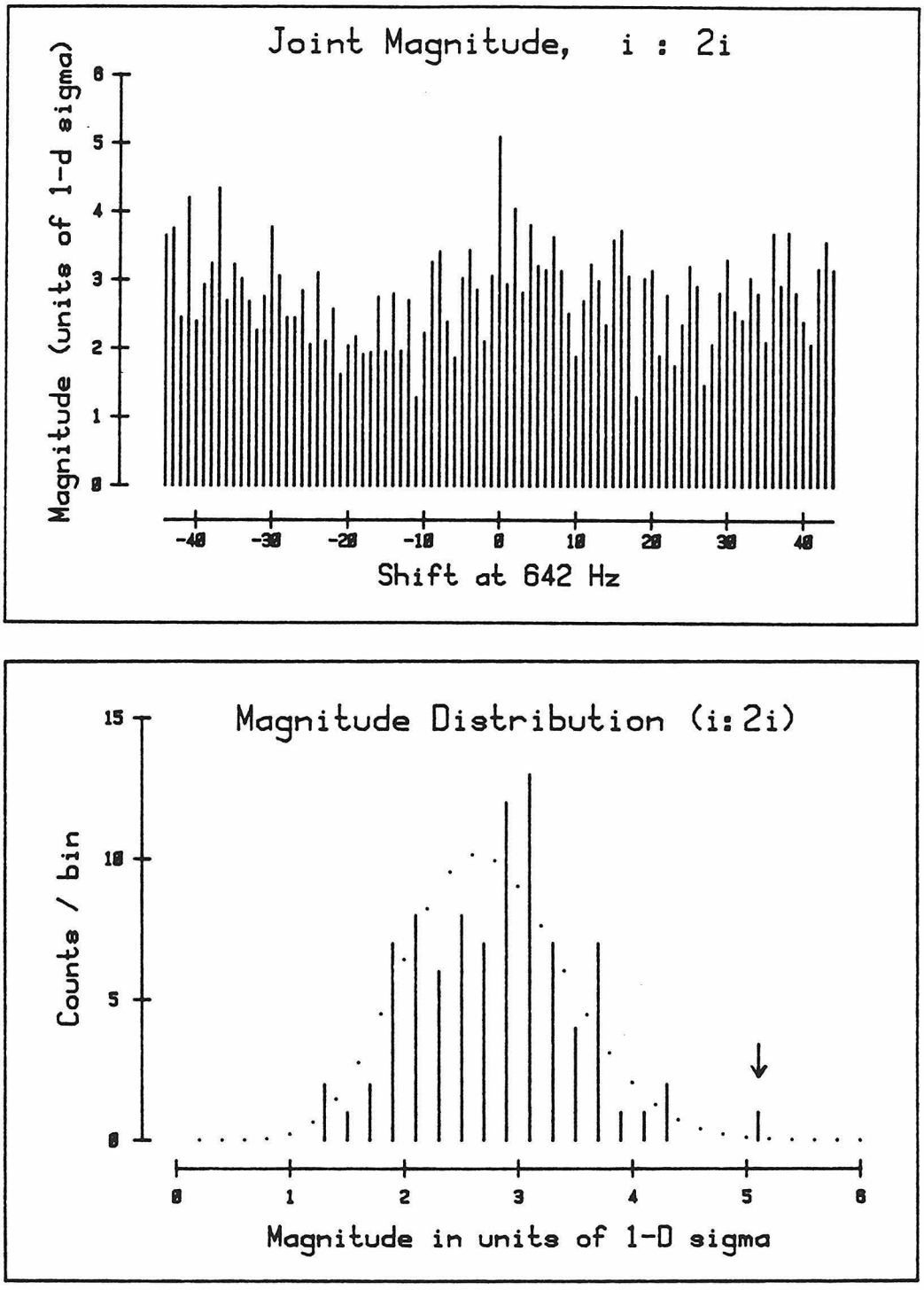

Figure 6.8. The joint magnitude as a function of frequency (a) and its distribution compared to the theoretical distribution (b). Each point in (a) is the square root of the sum of squares of corresponding magnitudes from Figures 6.4 and 6.5 as in equation 6.3. The joint magnitude at zero-shift is conspicuous. It is labeled with an arrow in (b).

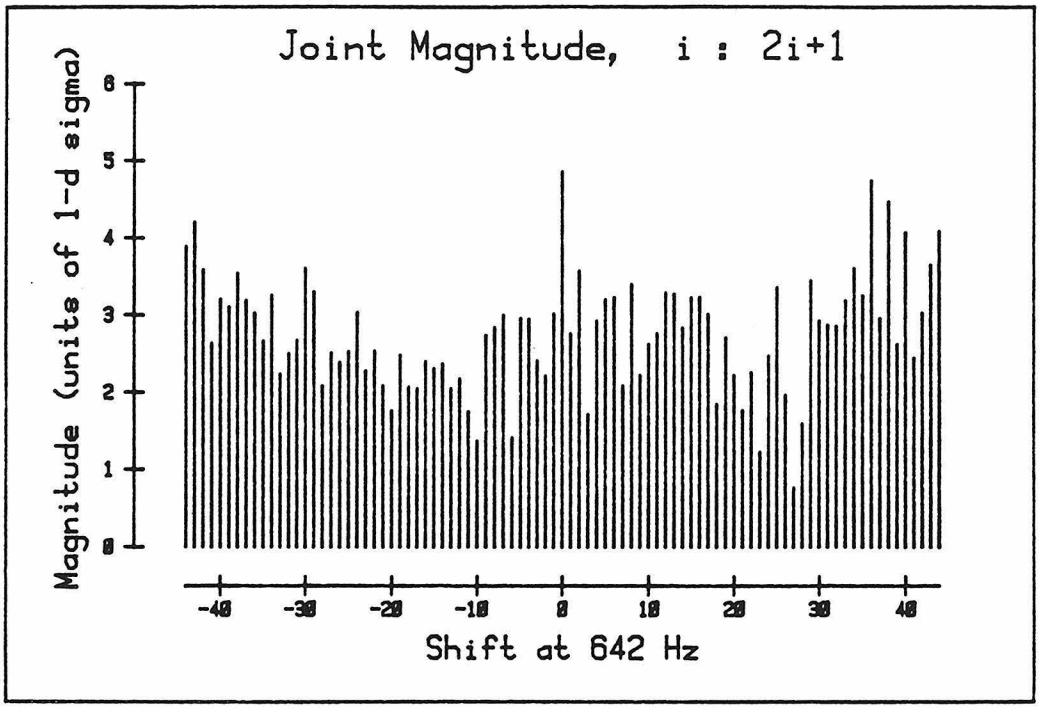

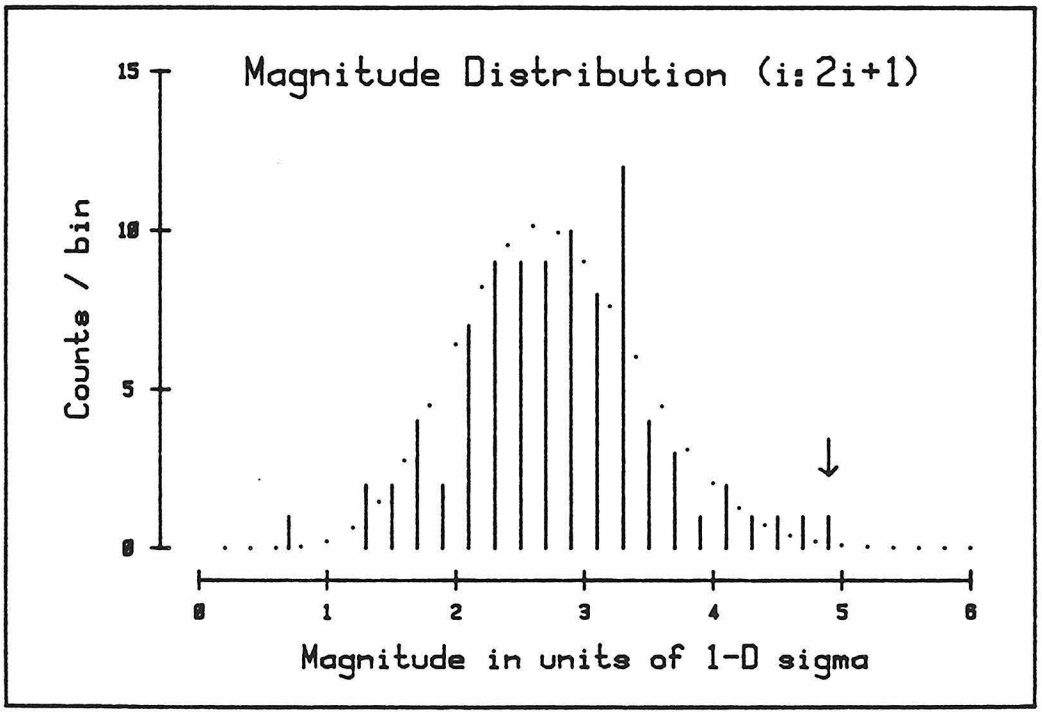

Figure 6.9. The same as in Figure 6.8 except that for each point in the spectrum, indexed by a shift of i, the 1284 Hz magnitudes at $2i+1$ were included in the sum of the squares, instead of the magnitudes at $2i$.

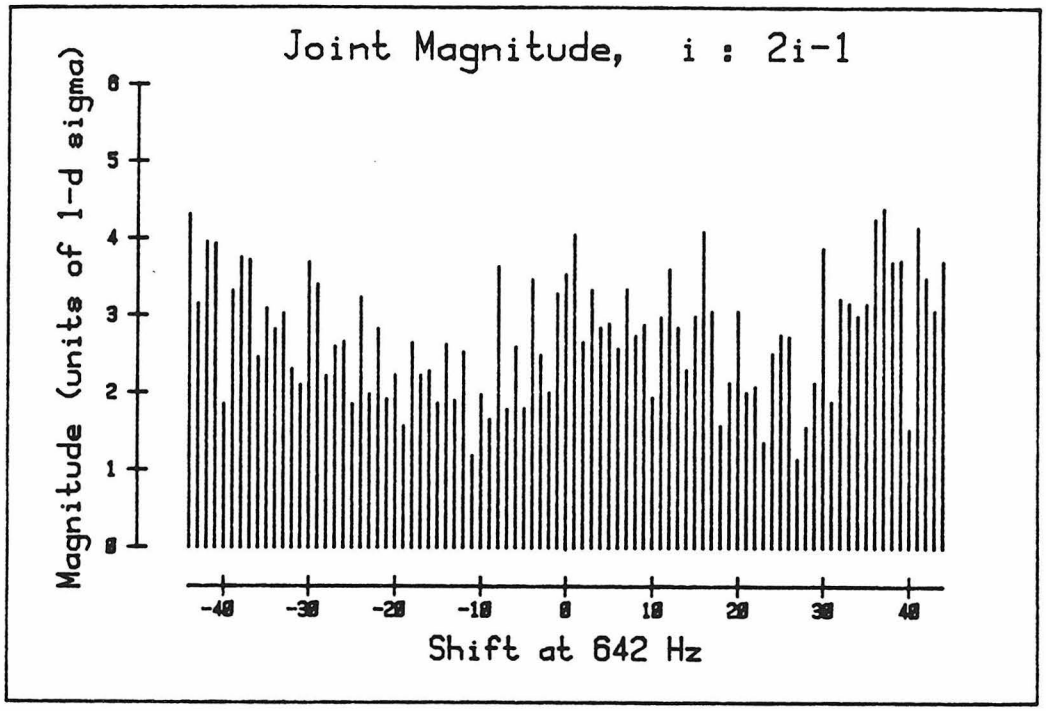

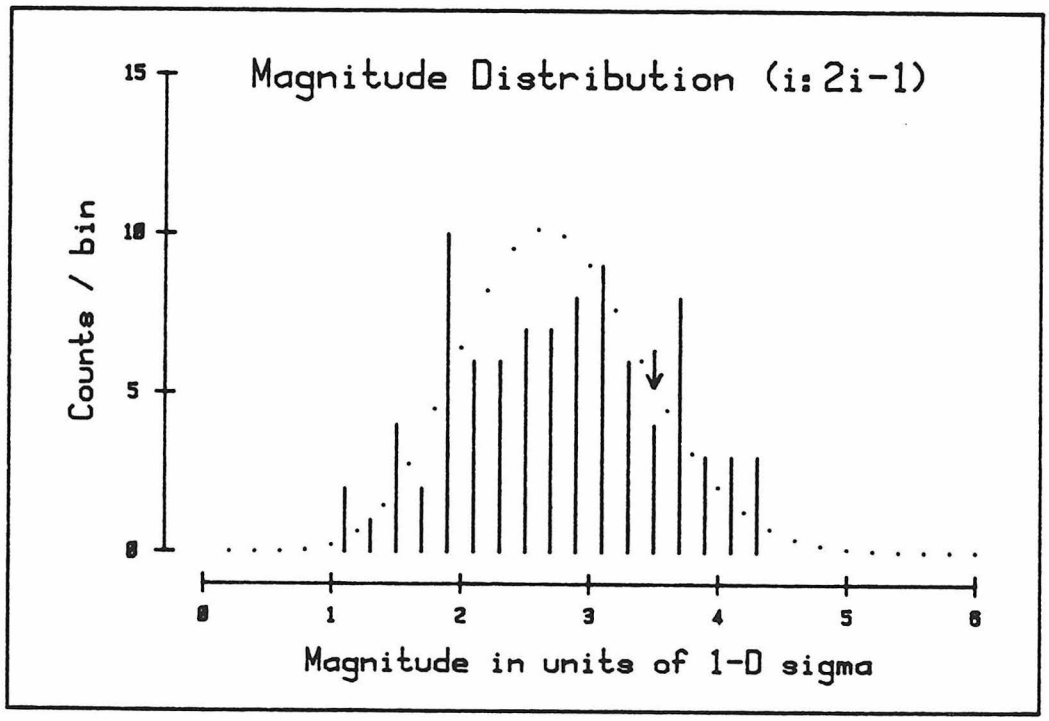

Figure 6.10. The same as in Figure 6.8 except that for each point in the spectrum, indexed by a shift of i, the 1284 Hz magnitudes at $2i-1$ were included in the sum of the squares, instead of the magnitudes at $2i$.

(The slim possibility that I observed the pulsar while the radiation was temporarily "turned on" still remains.)

Remaining as a possible explanation for the peak height (aside from the statistical one) is that a systematic error such as might be provided by a ground loop was responsible. Because of a limitation in the available instrumentation,[2)] the pulsar frequency itself was generated rather than some convenient subharmonic. During a long trial run, a ground loop which coupled the pulsar frequency to the signal was discovered and corrected. Additional pains were then taken to break other ground loops and shield against pickup.

A simple ground loop alone would not easily explain the presence of a large peak in the "cross" polarization spectrum at 1284 Hz since half the data was averaged with a change of sign - it should have canceled. However, systematic variations in the weighting of the data might allow a constant signal to show up in the "cross" polarization. This might arise from any diurnal variation in the performance of the interferometer, such as might be caused by temperature changes. To test this, I computed the the effect of the measured weighting factors on a supposed constant signal. The amplitude that leaked through to the "cross" polarization was 25% of the amplitude appearing in the "plus" polarization. This is six times too small to account for the measured "cross" amplitude at 1284 Hz if it is due entirely to "leakage" from the "plus" amplitude of 8.8×10^{-18} (Table 6.2). A more complicated problem, like a time-dependent ground loop, might explain the peak height.

[2)] The HP-3336A frequency synthesizer has a 1 μHz resolution. With the 10 digit frequency accuracy required, I had to program the synthesizer with 10 times the pulsar fundamental and divide it down externally.

6.3. Speculations

Inverting equation 3.2 I find that an observed $h \approx 10^{-17}$ corresponds to a power output of roughly $60\,M_{\odot}/s$ for an isotropically radiating source 6 kpc distant. A sustained output of this magnitude would be difficult, by some 16 orders of magnitude, to reconcile with current pulsar physics. It is hard to imagine a gravitational source of such an amplitude in this experiment.

Nonetheless, it was instructive and fun to try to calculate the consequences of the measured amplitudes in the context of a simple model. I compared the measured complex amplitudes at zero shift with the Zimmermann and Szedenits waveforms for a freely precessing axisymmetric body.

$$\tilde{h}_{+} = \frac{2I_1\omega^2\varepsilon\sin\theta}{r}\left[(1+\cos^2 i)\sin\theta\cos 2\omega t + \cos i\sin\cos\theta\cos\omega t\right] \qquad (6.4a)$$

$$\tilde{h}_{\times} = \frac{2I_1\omega^2\varepsilon\sin\theta}{r}\left[2\cos i\sin\theta\sin 2\omega t + \sin i\cos\theta\sin\omega t\right] \qquad (6.4b)$$

In these equations ω is the fundamental gravitational radiation frequency, r is the distance to the pulsar, θ is the angle between the pulsar angular momentum and its symmetry axis, i is the angle of inclination of the angular momentum to the plane of the sky (0° is pointing at us), and the ellipticity is $\varepsilon = (I_3 - I_1)/I_1$, expressed in terms of the principal moments of inertia, $I_1 = I_2 \neq I_3$.

Assuming that the signal is at zero shift, is the same as assuming that the precession frequency is less than $\sim .8\,\mu$Hz. A larger precession frequency would shift the gravitational radiation off of the center frequency of 1284 Hz.

A rotation of coordinates about the direction of propagation was required to convert my coordinates x and y to theirs. The coordinates for which equations 6.4 apply maximize the ratio of $|\tilde{h}_{+}|/|\tilde{h}_{\times}|$ at 1284 Hz. Consistency with the model requires also that this ratio be minimized at 642 Hz by the same

transformation. I chose to work first with the 1284 Hz amplitudes because they are both above the background; the 642 Hz "cross" amplitude is buried in the noise. A rotation about the direction of propagation by an angle φ transforms the polarization amplitudes at a given frequency as

$$\begin{bmatrix} \tilde{h}_+ \\ \tilde{h}_\times \end{bmatrix} = \begin{bmatrix} \cos 2\varphi & \sin 2\varphi \\ -\sin 2\varphi & \cos 2\varphi \end{bmatrix} \begin{bmatrix} h_+ \\ h_\times \end{bmatrix} \tag{6.5}$$

The ratio is maximized for an angle of 62°. The projection of the pulsar's angular momentum onto the sky would be either parallel or perpendicular (with either sign) to a line 62° (in the right-hand sense) from my x-axis.

In this coordinate system, the "plus" and "cross" amplitudes at 1284 Hz, are phased by 90° to one another as is evident from the waveforms. (The maximization guarantees this for any initial complex amplitudes, whether they are physical or not.) The ratio is seen from the equation to be $(1+\cos^2 i)/2\cos i$. Interestingly, the maximized ratio sets the inclination angle of the angular momentum to the sky at 94° (90° being in the plane of the sky). This is striking because the electromagnetic pulse profile indicates that the angular momentum vector might indeed be nearly in the plane of the sky. The pulse profile has a primary peak and a secondary peak separated by 180°. We are probably seeing pulses alternately from opposite poles. This is explained most easily by an angular momentum in the plane of the sky and a dipole field aligned perpendicularly.

Next, I assumed that the 642 Hz "plus" polarization amplitude represents a true signal. I calculated the set of "cross" polarization amplitudes for which $|\tilde{h}_+|/|\tilde{h}_\times|$ is minimized by a rotation of coordinates through 62°, as in equation 6.5. The consistent amplitudes are not implausibly far from the measured "cross" amplitude, but further progress along these lines requires a more sophisticated approach.

For a more likely gravity wave signal I could include the statistics of the background to generate a "most likely" set of amplitudes consistent with the model. To do this, I would have to make comparisons of the magnitudes and phases of all four amplitudes. The "raw phases" of Table 6.2 must be corrected as described earlier to compensate for systematic phase shifts that are different at 642 Hz than at 1284 Hz. From the corrected values I could carry the analysis profitably further to arrive at values for θ (between 0° and 90°) and $|I_1\varepsilon/r|$. The assumed distance of 6 kpc then provides and estimate of $|I_3-I_1|$.

6.4. Concluding Remarks

The experiment places a 99.7% confidence limit on gravitational radiation from PSR 1937+214 in 523 μHz frequency bands centered on the radio pulsation frequency and its first harmonic (Table 6.2). Limits were placed on each polarization component separately. The result at 642 Hz is new. It is important because under the reasonable assumptions of small wobble angle and near axial symmetry gravitational radiation is expected to be emitted predominantly at this frequency and not 1284 Hz. The limit placed on radiation at 1284 Hz is not as strong as that implied by the experiment carried out in Glasgow. It did, however, inspire a second look at the Glasgow data to remove the possibility of gravitational radiation in a particularly devious polarization state.

The experiment demonstrated that even at this early stage, the Caltech detector can run unattended for hours at a time and for as long as a day without more than minor adjustment. Valuable experience with the detector and the effects of temperature changes on it was gained.

Appendix

DESIGN OF THE TEST MASS AND POINTING CONTROL SYSTEM

The test masses must be free to respond to gravitational radiation. At the same time, they must be isolated from other perturbing influences - ground vibrations, magnetic fields, etc. - that might masquerade as gravitational radiation. These considerations motivated the design of the test masses and their suspension system and orientation control system.[1)]

The resonant suspension of the test mass allows the mass to be free for gravitational waves above the suspension frequencies. It also provides attenuation of ground vibrations. The final stage of this passive isolation is provided by hanging the test mass from wires, giving it a high-Q pendulum resonance at 1 Hz. Without this high quality factor, the thermal noise of the pendulum mode would limit the sensitivity of the detector.

Likewise, the test mass itself must be made of high-Q material with resonances removed from the frequencies of interest around 1 kHz. The current mass compromises this ultimately necessary design feature in favor of a design which allows convenient access and modification of the optics - a necessity at this early stage in the development of the detector.

Magnetic materials have been avoided where possible, but again, the need for flexibility has taken precedence. Mirrors mounts have been motorized in many places; in the future they will probably have to be machined in the correct place on the test mass. The mirror mounts are the source of resonances and

1) In this endeavor, I have benefited significantly from the work done at Glasgow by R.W.P. Drever, W.A. Edelstein, G.M. Ford, S. Hoggan, J. Hough, I. Kerr, W. Martin, B.J. Meers, A.J. Munley, G.P. Newton, J.R. Pugh, N.A. Robertson, and H. Ward.

damping. The magnets in the motors may be a small source of noise due to their coupling to stray magnetic fields.

The resonant nature of the suspension enhances vibrational motions at the resonant frequency. This doesn't affect the noise performance of the antenna directly since the resonant frequency is well away from the current frequencies of interest, and can be made lower if the interest changes. The resulting motions, both translational and rotational, are too large for the dynamic range of the interferometer. The translations of the test mass at 1 Hz can be as large as 10 to 100 wavelength of light after transient excitations. This exceeds the maximum excursion of the piezo-driven mirror. For even smaller motions than this (only a few wavelengths) the limited bandwidth of the second cavity loop makes it difficult for the loop to acquire lock because of the narrow resonance of the cavity. Small piezoelectric transducers at the wire suspension point have been provided so that the pendulum motion of the test mass can be actively damped.

Likewise, the orientation of the mass is important at least as far as it impinges on the dynamic range limitations of the interferometer. A quick estimate of the dynamic range constraint can be obtained by requiring that the cavity not excite off-axis modes significantly. The rough requirement is that the laser beam be deflected by less than a tenth of the beam diameter at a distance of 40 meters. With a beam diameter of a few millimeters this gives a pointing accuracy requirement of better than 10^{-5} radians. This is the aim of the orientation system.

The design of the suspension system described in what follows is motivated by these constraints. Particular attention was paid to coupling forces and torques to the test mass so that low frequency resonances could be actively damped. Care was taken so that changes in the separations between the masses

are not excited by mechanical couplings since this might degrade the noise performance of the detector.

A.1. The Mechanical Design

Photographs of one of the test masses and its suspension system are shown in Figures A.1 and A.2. The test mass itself is two 14" diameter aluminum disks separated and unified by five 1" square posts - four around the rim, and the central one to which the pendulum suspension wires are attached. The 4.5" separation between the disks is a working space where mirrors and other optics are placed. The test mass is hung at its center of mass to minimize translations due to rocking motion. Three 0.018" diameter piano wires clamp to the center post and pass through holes in the top disk. Twenty centimeters in length, they clamp to a small machined block of aluminum called the control block. A single 0.012" diameter length of piano wire supports the weight of the control block/test mass combination at the center of the control block. All wires that are clamped to the control block make contact with the block in a horizontal plane which divides its mass in half. This minimized many couplings of control block orientation to translation of the translation mass. Furthermore, these four main suspending wires contact the test mass, control block and support point at well-defined places. Their tensions hold them in place in V-grooves.

A.1.1. The Test Mass

The position of the cavity mirror on the test mass minimizes coupling of orientation to cavity length. The mirror axis is made to coincide with the line joining the center of masses of the two test masses and therefore the center of rotations. Because of this, cavity length is completely insensitive to tilts about the mirror axis. The remaining rotation and tilt have only second order coupling

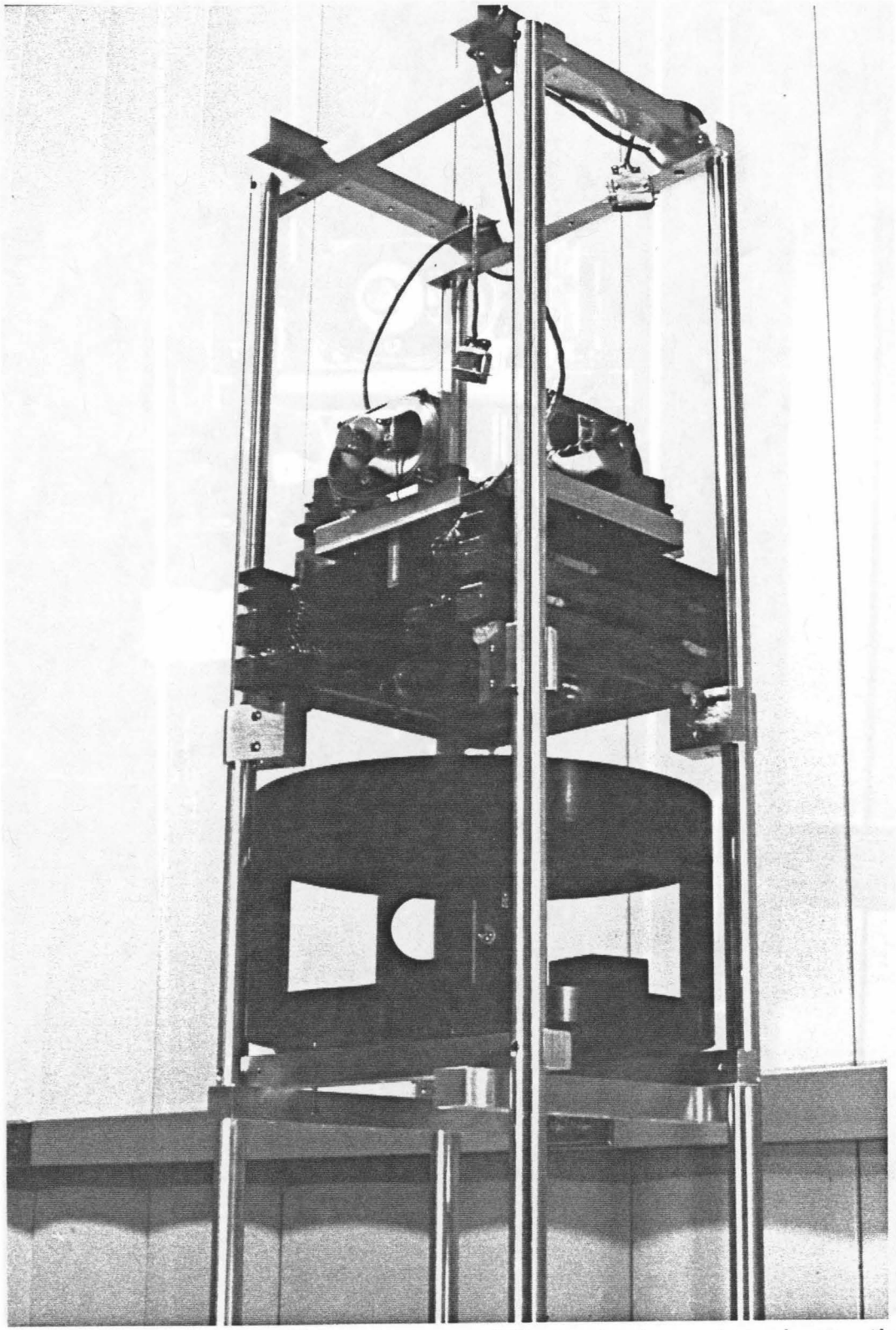

Figure A.1. Oblique view of a test mass and its suspension system showing the frame, lead and rubber isolation stack, transducer support, and test mass.

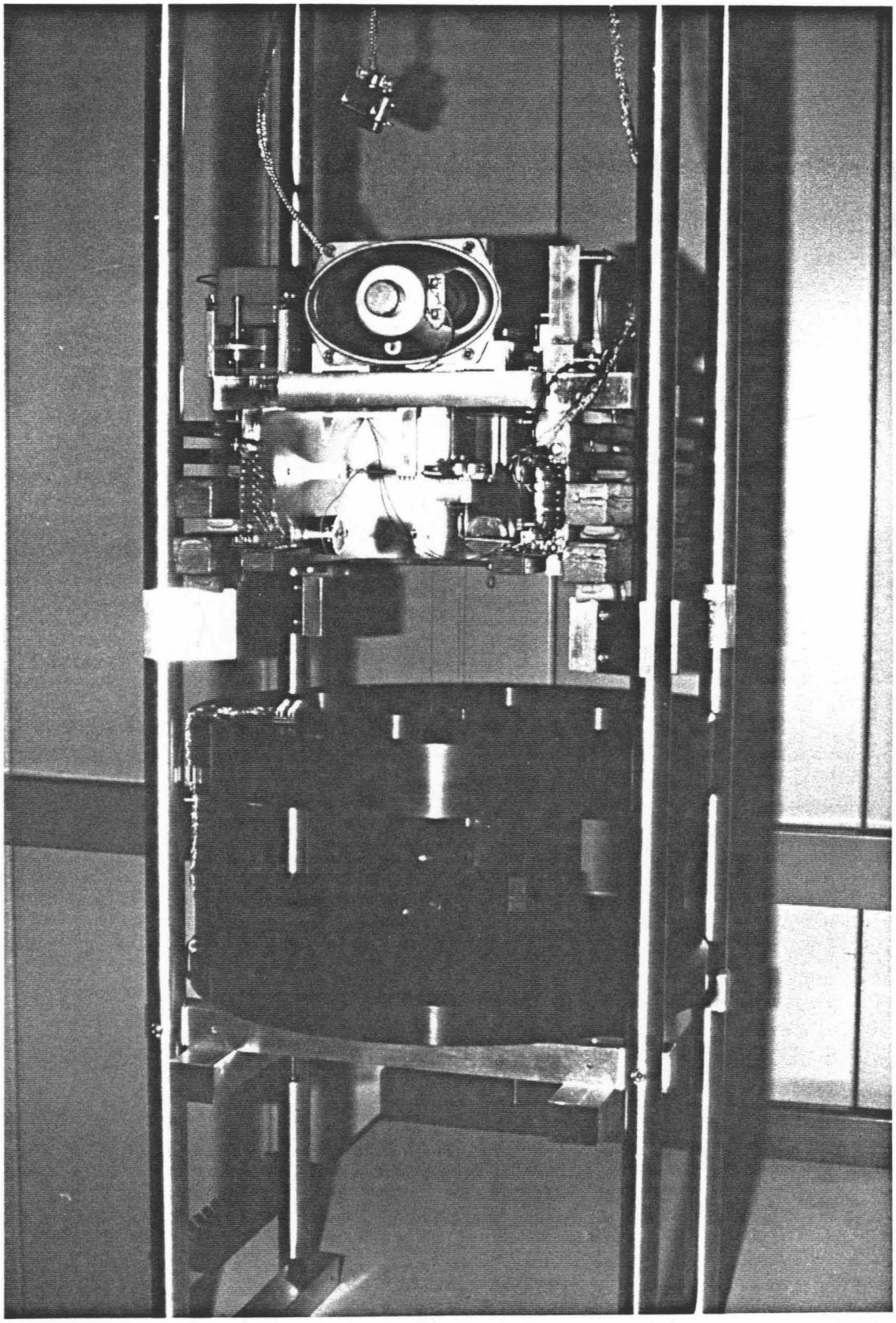

Figure A.2. Frontal view of a test mass showing the frame, transducer support, control block, and suspension wires.

to the cavity length. Ideally, the cavity mirror would be placed at the center of mass. But, because of the optical elements needed between the mirror and the central post, it is quite near the rim of the test mass.

Signals to the various motor driven mirrors and orientation transducers are brought to the test mass by as many as 20 thin wires (about AWG 40).

A.1.2. Control Block

The high Q pendulum mode of the suspension can be artificially damped by applying appropriate forces to the test mass. This is done by effectively moving the point from which the mass hangs. Two piezoelectric flexing disks pull on two of the three suspension wires at a place a few centimeters below the control block (Figure A.3). The three pendulum wires are kept parallel by a 0.004" nichrome wire encircling them and a tensioning spring on the third wire.

The control block itself is constrained from translating by two 0.008" tungsten wires attached at one end to small translation stages for adjustment. The wires are affixed to the centers of adjacent sides of the control block and kept under tension by opposing springs (Figure A.4).

One corner of the control block is linked to the cone of a loudspeaker by a thin wire. The spring that opposes the translation constraint wire on the same side is offset to compensate for the tension in the speaker cone. Current applied to the speaker coil increases or decreases
this equilibrium tension changing the orientation of the control block and applying a torque to the test mass below. The puppet on a string analogy often used to describe this interaction will not be mentioned here.

Tilting torques are applied to the mass as easily. Two thin wires clamp to adjacent sides of the control block and ultimately connect to two additional speaker cones above. The tensions in the cones are balanced by a single spring

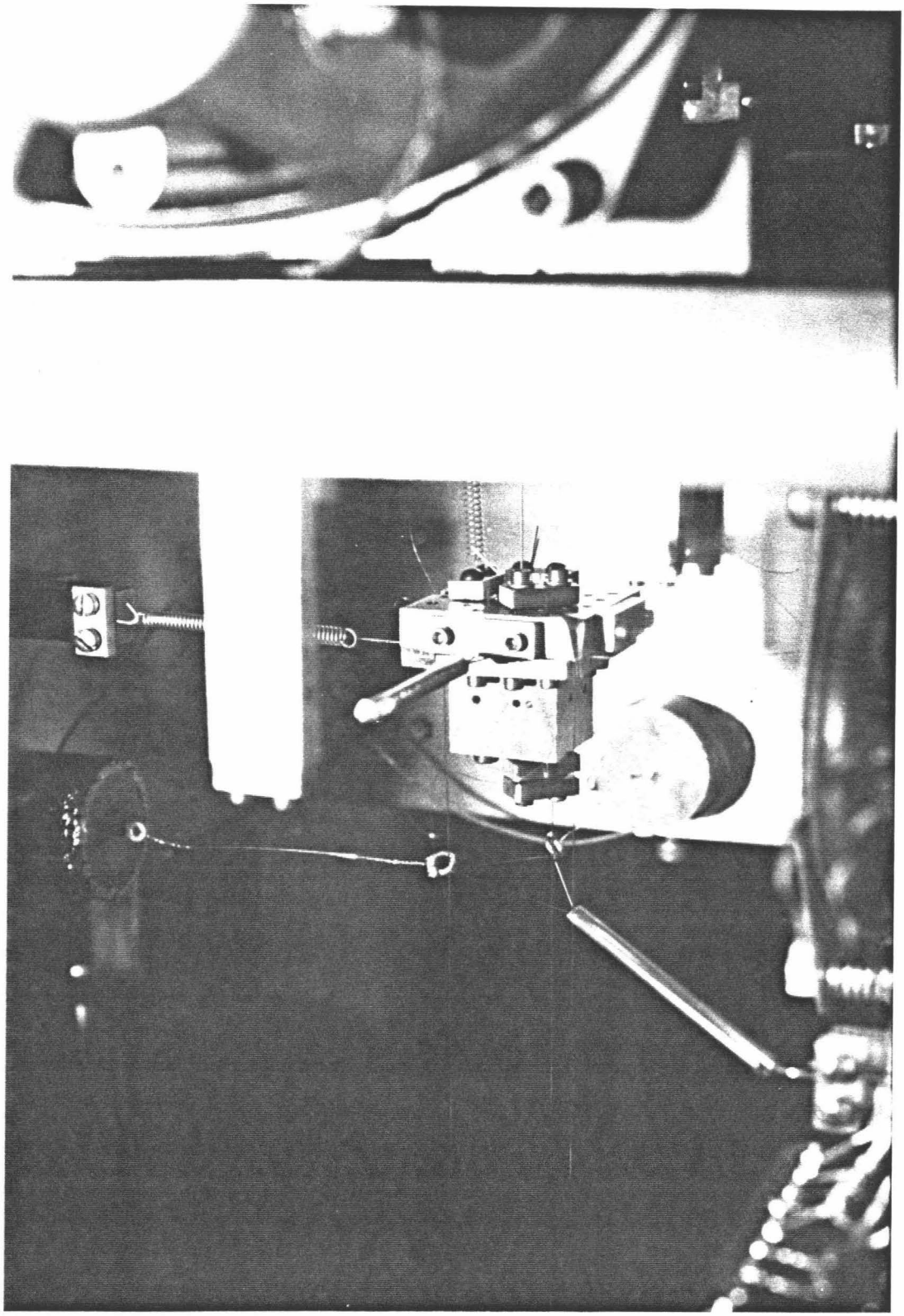

Figure A.3. The control block and piezoelectric wire-pushers. The connections in the horizontal plane of the control block constrain it from translation while allowing it to rotate.

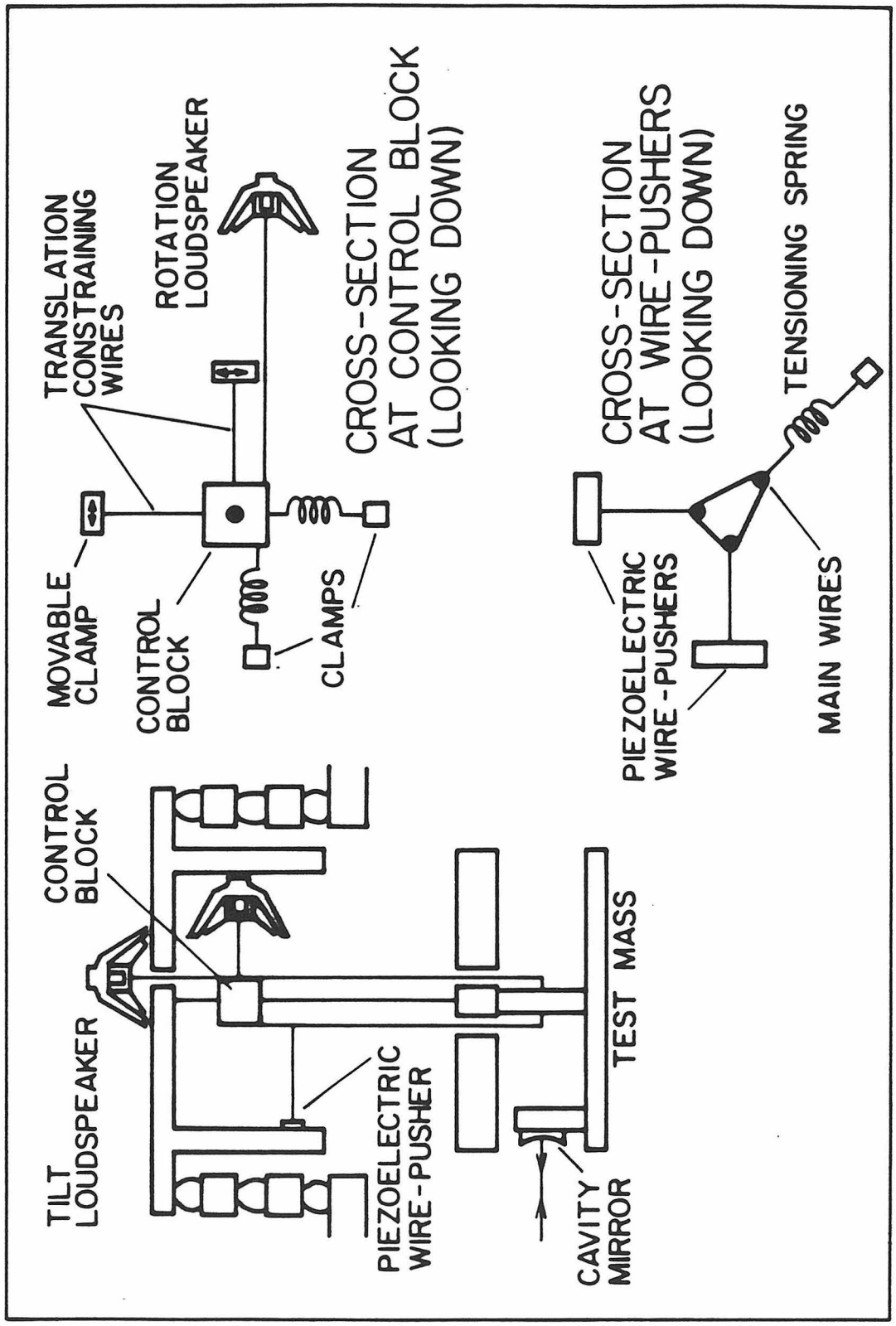

Figure A.4. Connections to the control block. The control block is constrained so that it cannot translate, but remains free to rotate and tilt through small angles. Below the control block, the wire-pushers define the point from which the test mass hangs.

clamped to the opposite corner of the control block edge. The torques are transmitted to the test mass by the suspension wires.

A.1.3. Transducer Support

I should emphasize at this point that all of the connections to the control block (except for the two tilt wires and associated tensioning spring) are made in the same horizontal plane which divides the control block mass into two equal parts. This arrangement minimizes couplings of rotation to tilt and translation.

The other ends of all the wires and springs described so far (except for the three suspension wires destined for the central post of the test mass) wind up anchored in some way to a shell-like construct called the transducer support. The photos in Figures A.5, A.6, and A.7 show details of the transducer support along with its relationship to the control block and the lead/rubber isolation stack. It is a 1" plate of aluminum atop three walls of ½" steel. The enclosure encompasses the suspended control block, leaving the bottom and one side open for access. Speakers, clamp posts, and PET's are anchored to it.

The transducer support rests on three screws, each with a ball bearing fitted to its tip. One round tip seats in a machined dimple. A second seats in a groove. These constraints precisely define the position of the transducer support so it can't rock or slide.

Two of the screws are motor driven. They adjust the tilt of the transducer support and therefore the test mass. Drifts too large for the active servos to accommodate can accumulate as rubber settles, speaker cones age, or the temperature changes by a few degrees Celsius. The transducer support (and so the mass) can also be rotated. It sits on what I call the split horseshoe: a pair of steel horseshoes separated by three ½" ball bearings which roll in a circular guide groove machined on the inside surfaces. The horseshoe shape - a squared

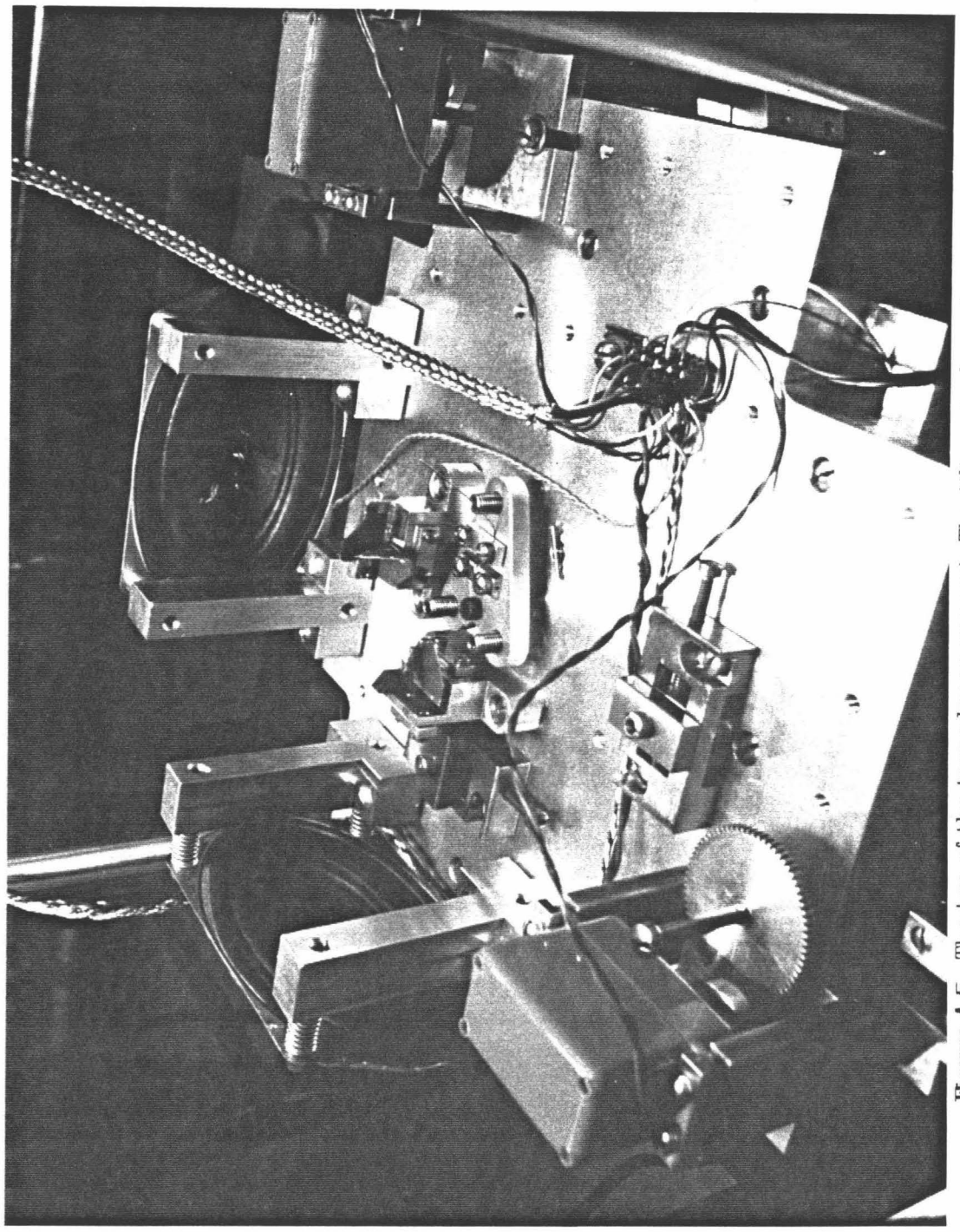

Figure A.5. The top of the transducer support. The tilt control speakers, translation constraint adjustments, and tilt-adjusting motors are shown.

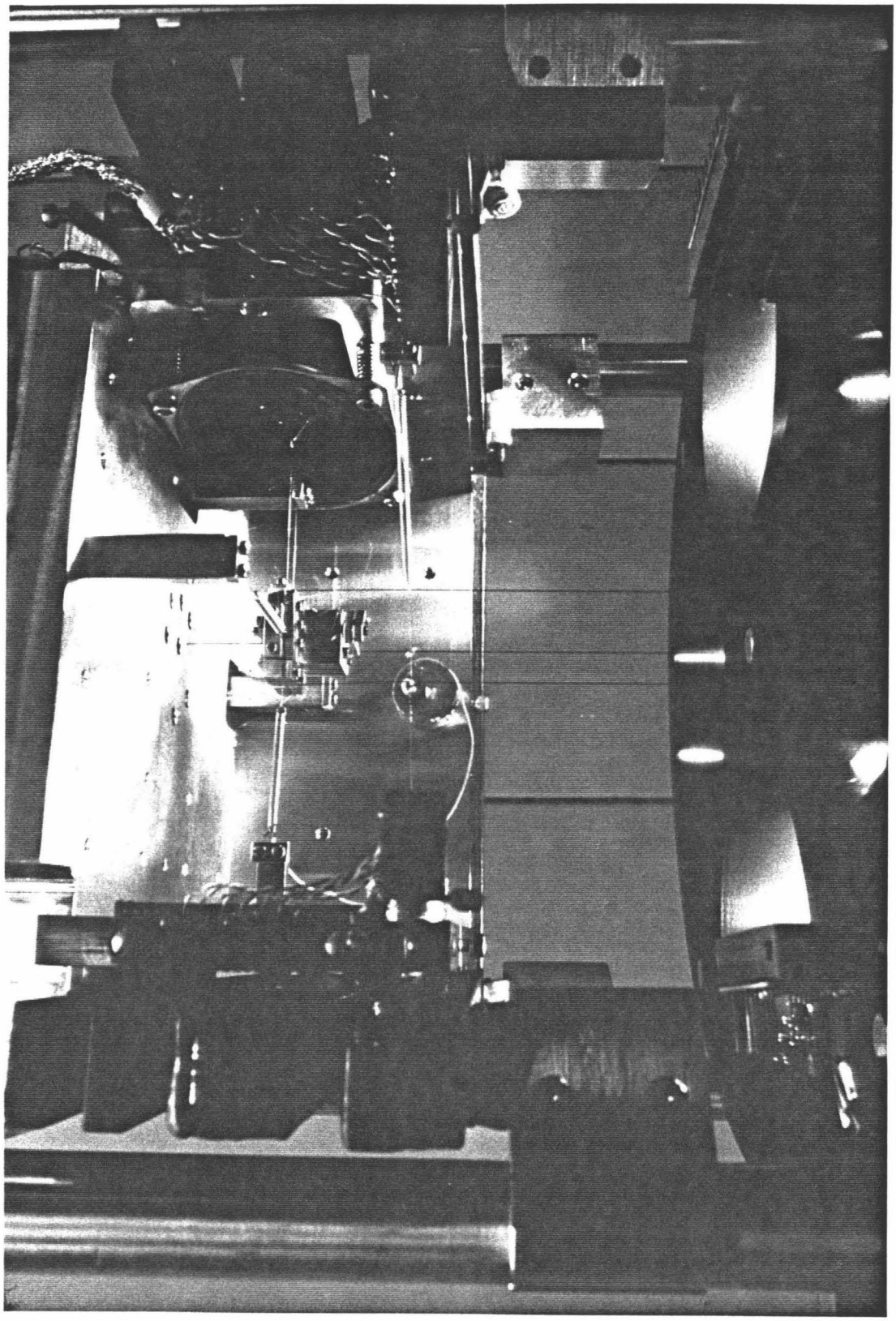

Figure A.6. The inside of the transducer support showing its relationship to the control block and the test mass.

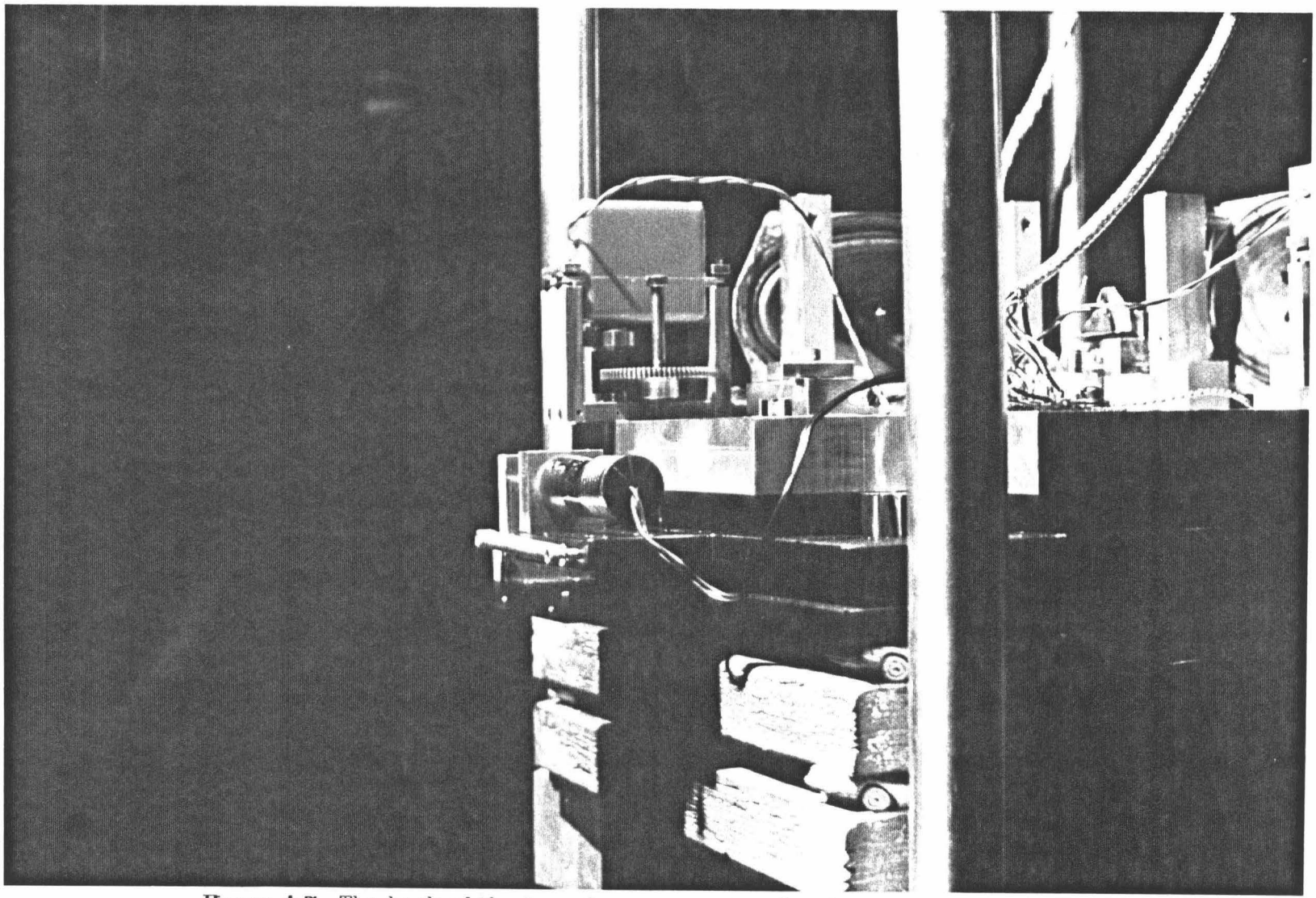

Figure A.7. The back of the transducer support and isolation stack. The alternating lead and rubber "horseshoes", and the motor which drives the "split horseshoe" are shown.

off version of it, anyway - surrounds the three walls of the transducer support, leaving the front free for easy access of the control block. The top half can be rotated with respect to the bottom half by a motor driven screw.

The split horseshoe sits on rubber which sits on top of two alternating lead horseshoe and rubber layers. The bottom rubber pieces rest on an aluminum frame which is bolted to the bottom of the tank.

The lead was chosen because of its density and availability. The more mass, the lower the resonant frequency and the smaller the motion. The rubber is a soft rubber in the form of toy car erasers. It was chosen over other rubbers which were either too stiff, laced with air pockets, or too easily and permanently deformed.

A.2. Effectiveness of Vibration Isolation

A single damped harmonic oscillator such as a pendulum or layer of lead and rubber responds to motion of its suspension point according to

$$(\delta x)^2 = \frac{1 + \frac{z^2}{Q^2}}{(1 - z^2)^2 + \frac{z^2}{Q^2}} (\delta x_D)^2 \qquad (A.1)$$

where δx is the response to driving displacement δx_D, $z \doteq f / f_0$, the ratio of frequency to resonant frequency, and Q is the quality factor.

Two limits of this equation are important for high frequencies. First, for $z \gg 1, Q$ the equation yields

$$\delta x \simeq \frac{f_0}{Qf} \delta x_D \qquad (A.2)$$

This is the limit that is most apt for the lead/rubber stack layers. It applies for frequencies above about 10 Hz since the resonance is at a few Hz and has a Q no bigger than 10.

On the other hand, a high Q stage such as the pendulum suspension may for frequencies of interest be in a regime where $Q \gg z \gg 1$. To include this limit, only assume that z , $Q \gg 1$. In this limit, equation A.1 gives

$$\delta x \simeq \left[\left\{\frac{f_0}{f}\right\}^4 + \frac{1}{Q^2}\left\{\frac{f_0}{f}\right\}^2\right]^{1/2} \delta x_D \qquad (A.3)$$

The combined effect for three stages of lead/rubber and the pendulum isolation is, for frequencies well above any of the uncoupled resonances, the product of single stage attenuations.

The ground noise was measured on the third floor of the W. Bridge Laboratory of Physics on the Caltech campus. For frequencies between 20 Hz and 1000 Hz it seems to be roughly expressible as a power law,

$$\frac{\delta x_D}{\sqrt{\delta f}} \simeq \frac{5\times10^{-5}}{f^3}\,\mathrm{m}/\sqrt{\mathrm{Hz}} \qquad (A.4)$$

I believe this is representative for frequencies above the resonant frequencies of the building, about 10 Hz. Conservative estimates of the quality factors put the motion of the test mass due to the ambient ground noise below $5\times10^{-29}\mathrm{m}/\sqrt{\mathrm{Hz}}$ at 1 kHz.

A.3. Pointing Control

Each test mass is nearly free to rotate about its suspension wire and tilt about two orthogonal axes. The rotation resonance has a natural frequency of about 0.1 Hz. The two tilt frequencies are roughly 0.3 Hz. The quality factors of these resonances are in the vicinity of 100 plus or minus half an order of

magnitude. Before the cavities can remain in resonance, these oscillations must be damped because the ambient motion often exceeds the dynamic range of the interferometer optics. This can't be done with the addition of lossy materials since the quality factor of the pendulum may be indirectly degraded.

Additionally, the many drifts effecting the orientation of the test masses would misalign the cavities in a short time.

To solve these problems, the critical degrees of freedom are controlled active feedback loops. An optical lever monitors the orientation of the mass. The signal from a position sensitive photodiode is amplified and filtered and then applied to the coil of the appropriate speaker. Figure A.8 shows the typical arrangement.

There are two optical levers for each degree of freedom being controlled. One, the local lever, has a short arm and refers the orientation to the optical table on which the test mass frame sits. This lever is part of the feedback loop only when crude alignment is required, particularly when the entire system is being aligned from scratch and it is impractical to maintain the global lever. This lever is 40 meters long and refers the orientation to the table at the opposite end of the arm. The mirror has a 40 meter radius of curvature so that the position sensitive photodiode output is insensitive to angular fluctuations of the laser beam introduced before it enters the vacuum tank.

The signal applied to the speaker coil has both "spring" and "damping" components in a ratio which provides slightly underdamped response of the test mass to orientation jolts. The schematic of the circuit which provides this filtering is shown in Figure A.9. The effect of the closed loop on the error signal is shown in Figure A.10. To remove the possibility that the orientation control loops might introduce noise in the interferometer at high frequencies, the feedback electronics is rolled off as rapidly as possible without introducing unstable

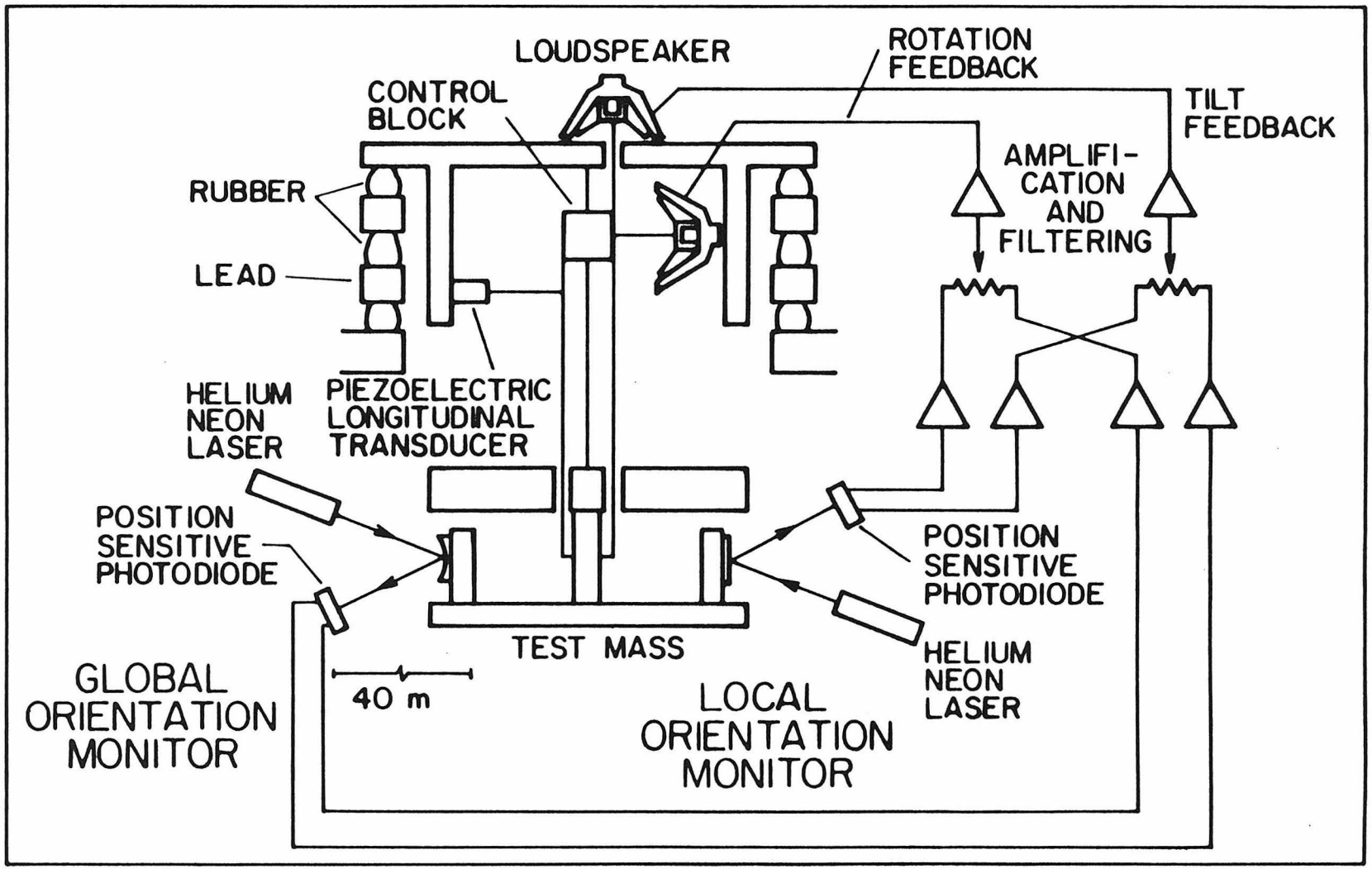

Figure A.8. The orientation control system. Each rotational degree of freedom is monitored by two optical levers. The local monitor provides a rough reference which is useful when the interferometer is being initially aligned. After this, control is passed smoothly to the global monitor by adjusting the potentiometer at the input of the feedback amplifier.

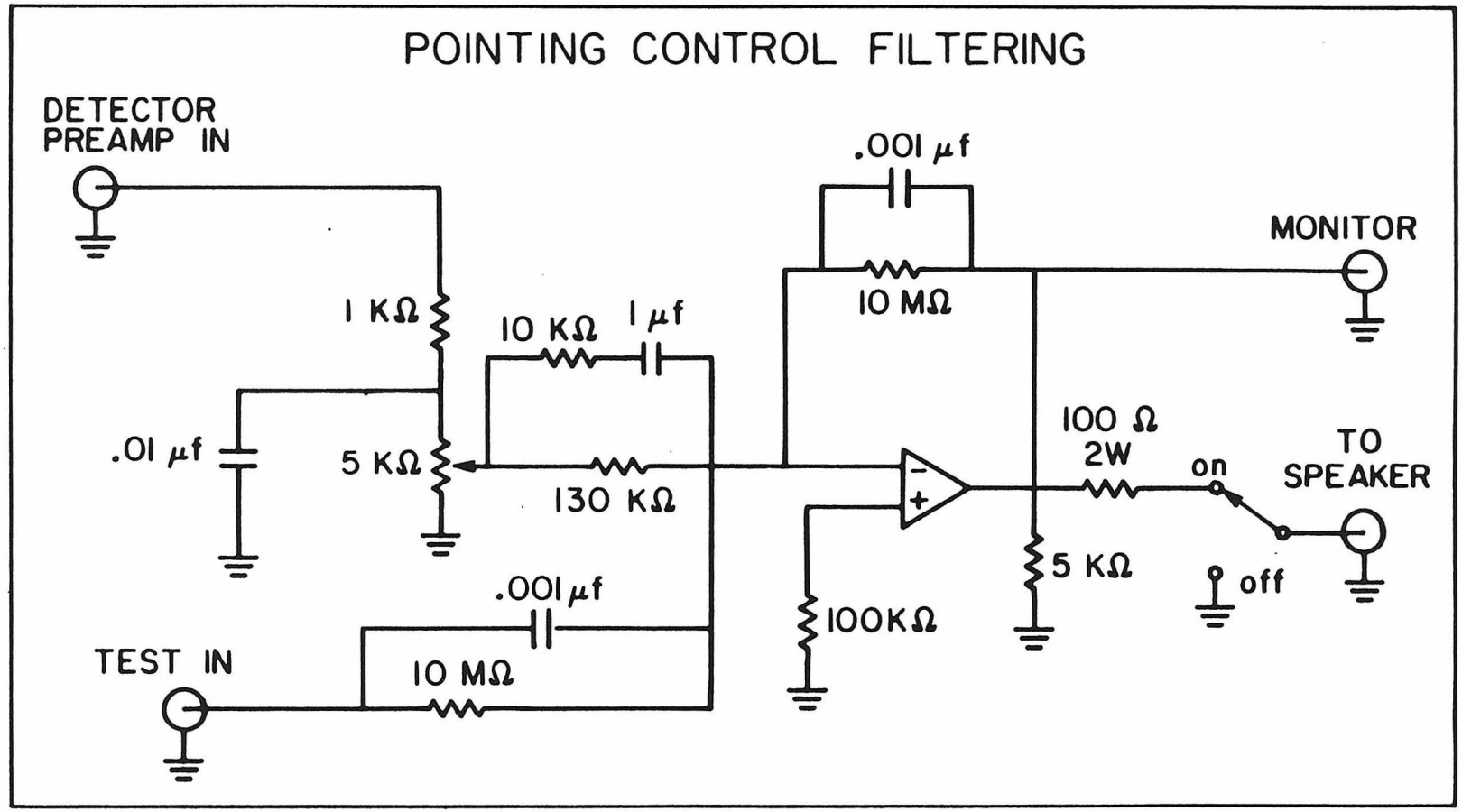

Figure A.9. The orientation control feedback electronics. The 1 μf capacitor and the 130 kΩ resistor at the input of the operational amplifier provide "damping" and "spring" filtering of the input signal. Most of the remaining impedances set the gain and attenuate the drive to the speaker for frequencies above 15 Hz.

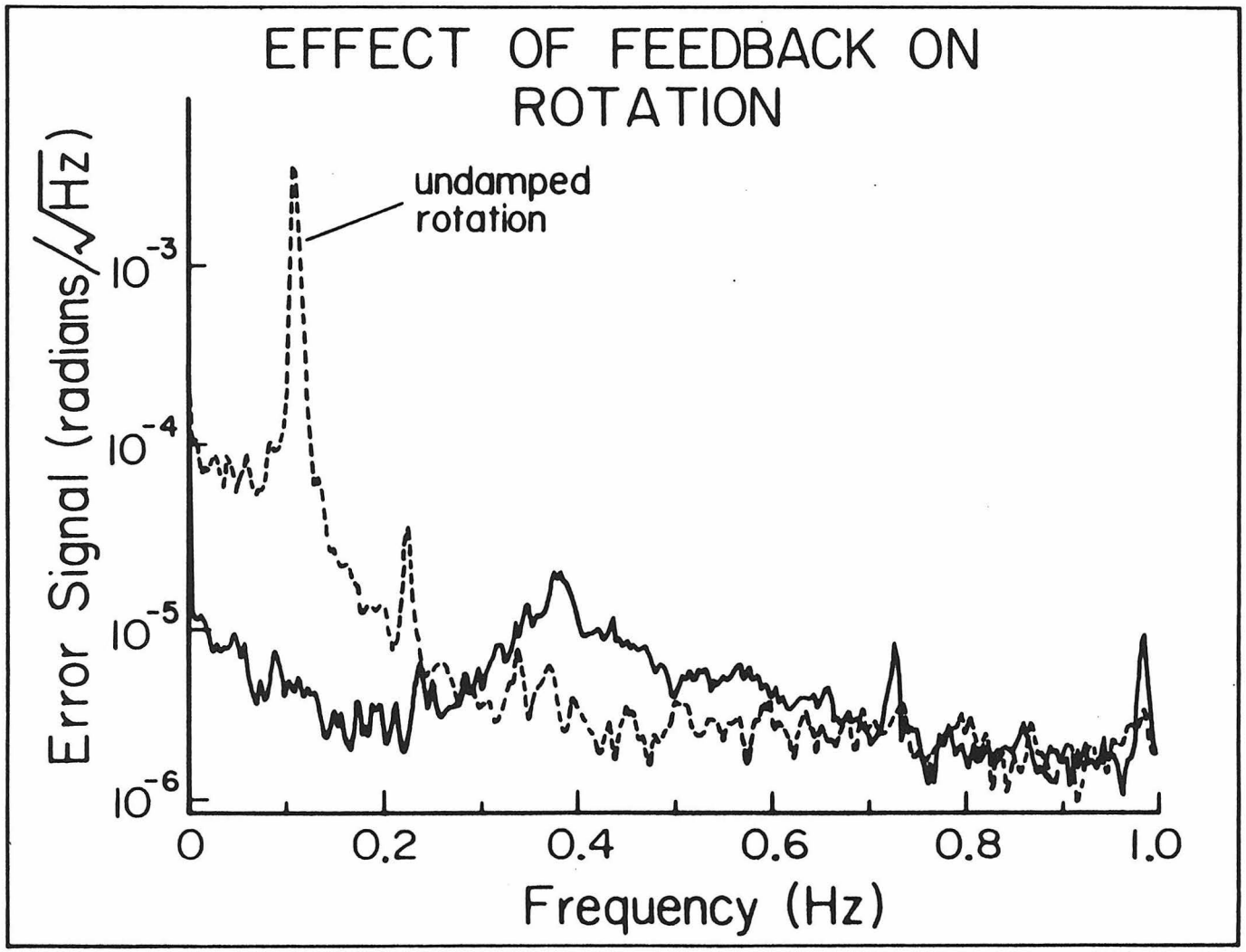

Figure A.10. Comparison of the rotation error signal before and after feedback is applied. The dashed line represents the ambient rotation noise, which is dominated by the resonance. It corresponds to more than 10^{-3} radians rms. With active damping the error signal (solid line) is reduced to about 10^{-5} radians rms. The bulge at 0.4 Hz is the modified resonant frequency, slightly underdamped.

oscillations.

A.4. Auxiliary Michelson Interferometer

The pendulum mode of the suspension also strains the dynamic range of the interferometer cavity loops. When the masses are swinging through a large number of wavelengths (10 to 100 is large) the fast piezo mirror, in particular, has a difficult time tracking the motion. For this reason, a small velocity dependent voltage is applied to some of the PET's at the pendulum suspension point to damp the differential length change between the two cavities.

The error signal is provided by a Michelson interferometer which has been integrated into the global orientation control optics for the masses labeled Huey and Louie (Figure A.11). The quarter wave plate ($\lambda/4$) in front of the 40 meter radius of curvature mirror on Louie rotates the linear polarization of the light in the second arm by 90° so that it is distinguishable from the light traveling down the first arm. The light exiting one port of the Michelson beam splitter is separated according to polarization and provides global orientation information at the position sensitive photodiodes.

The two polarization components exiting the other port are made to interfere by a polarizer oriented at 45° to them. To obtain a quadrature signal one of the polarizations has been phase modulated before the combination at the polarizer. The photodiode signal contains a fringe signal at DC and its quadrature at the modulation frequency. The two fringe signals are combined to give an approximation to the difference in cavity lengths even when the motion is many wavelengths.

The circuit which performs this feat (Figure A.12) is a poor man's fringe counting circuit. The sign of the quadrature signal determines whether the differential length is increasing or decreasing. Multiplying the DC fringe signal by

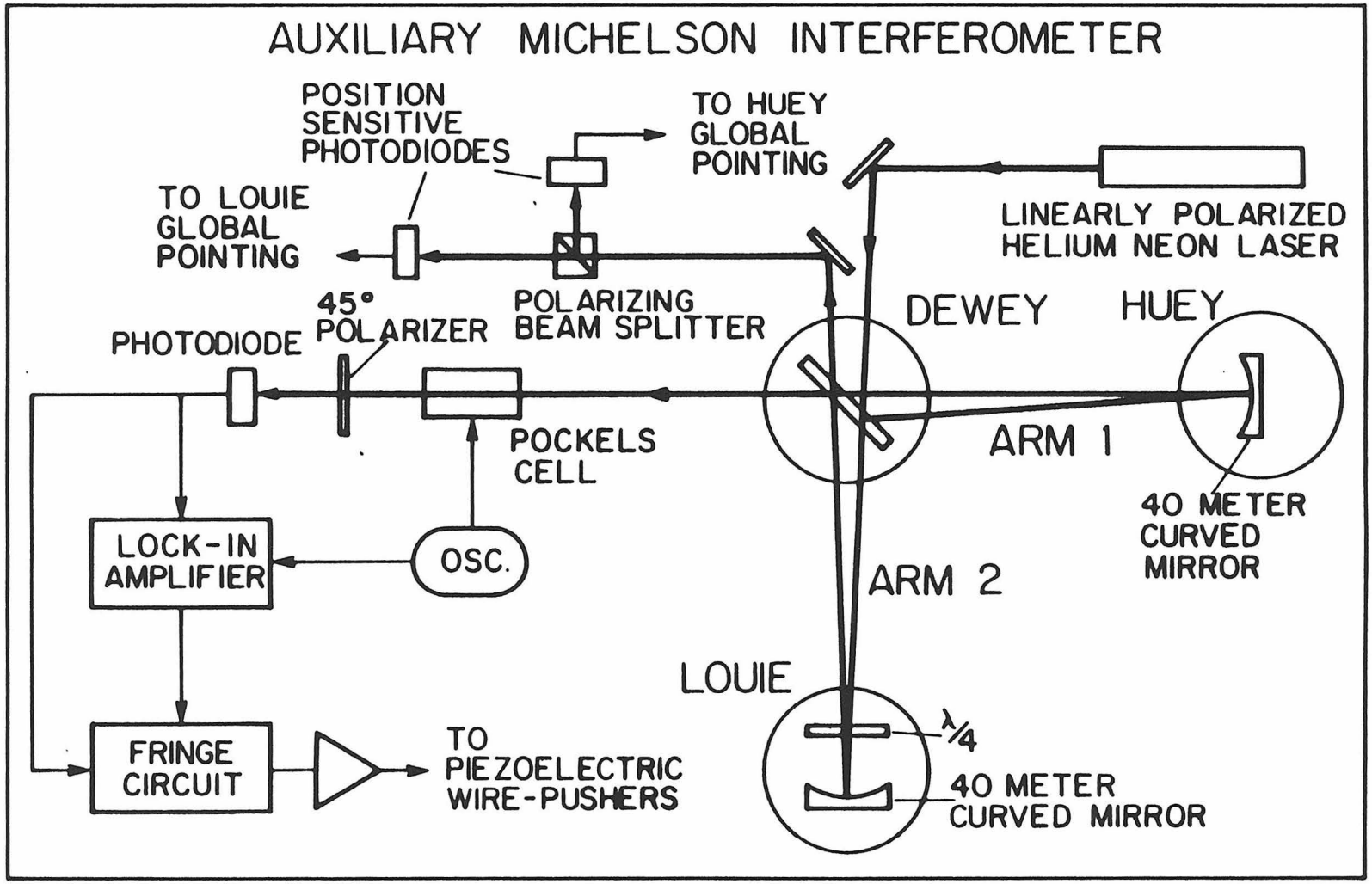

Figure A.11. The combined Michelson interferometer and global pointing optics. The quarter-wave plate on the test mass labeled Louie rotates the polarization of the light in the second arm by 90° with respect to the first arm. The two components exiting the interferometer at the top of the diagram are separated to provide global orientation monitors for the two end masses: Huey and Louie. The two components exiting to the left of Dewey are interfered to provide Michelson fringes. The Pockels cell phase modulates one of the polarization components so that the lock-in can extract the quadrature fringe signal.

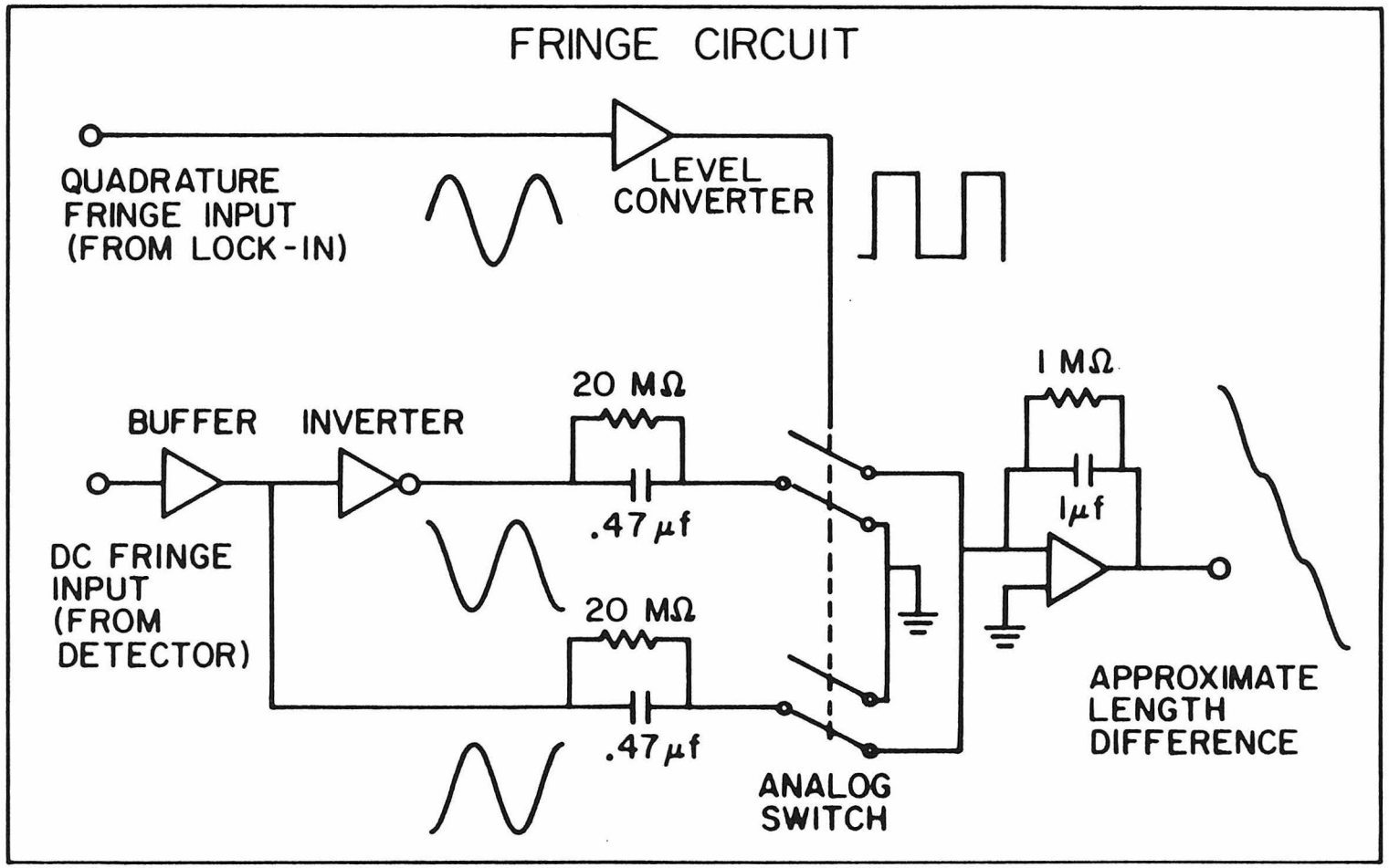

Figure A.12. The fringe circuit. The DC and quadrature fringe signals from the auxiliary Michelson interferometer are combined to generate an approximate arm length difference even when the test masses are moving through many fringes. The circuit works by pumping charge between the 0.47 μf capacitors and the 1 μf capacitor at the output. The pumping direction is determined by the relative phase of the two fringe signals in the same way that the differential test mass velocity is determined.

this sign gives a waveform that consists of positive slope (sinusoidal) segments for one direction of motion and negative slope segments for the other. The analog switch does this multiplication by alternately selecting the signal and its inverted version as required. The segments are composed end to end by the integration of charge onto the final feedback capacitor.

To sidestep startup problems, the charge is slowly drained off this capacitor with a time constant of several seconds. No real DC reference is supplied. This doesn't matter since the signal is only used to provide damping. It is differentiated and applied weakly to two of the PET wire pushers - one on each cavity.

A.5. Exposing a Coupling

This last section of the appendix I devote to an item which demonstrates the effectiveness of the design described to this point. The interferometer was for a time plagued with a large peak in its noise spectrum at 50 to 70 Hz. Noise at this frequency isn't particularly worrisome from the standpoint of detecting supernovae except that this resonance often leads to instability in the pointing servo loops.

The solution to the problem was adjusting the control block constraint wires until the resonance disappeared. The explanation goes like this. The main support wire is clamped to the center of the control block. The control block will, however, rotate about the intersection of the lines defined by the constraint wires. If that point doesn't coincide with the support wire contact, then the center of the control block will translate. The peak in the interferometer noise is evidence of this coupling.

A random noise generator drove the rotation speaker. The voltage induced in the PET wire pushers was monitored with a spectrum analyzer. The

translation stages to which the constraint wire are clamped gave a sensitive adjustment of the constraint geometry.

Misalignment of one constraint wire causes coupling to only one of the PET's, so it was a simple matter to minimize the effect. The results of a typical minimization are shown in Figure A.13. When misadjusted, rotation of the control block causes it to translate horizontally in both directions which in turn excites a mechanical resonance (dashed lines). The results of independently optimizing the adjustment for each direction are given by the solid lines.

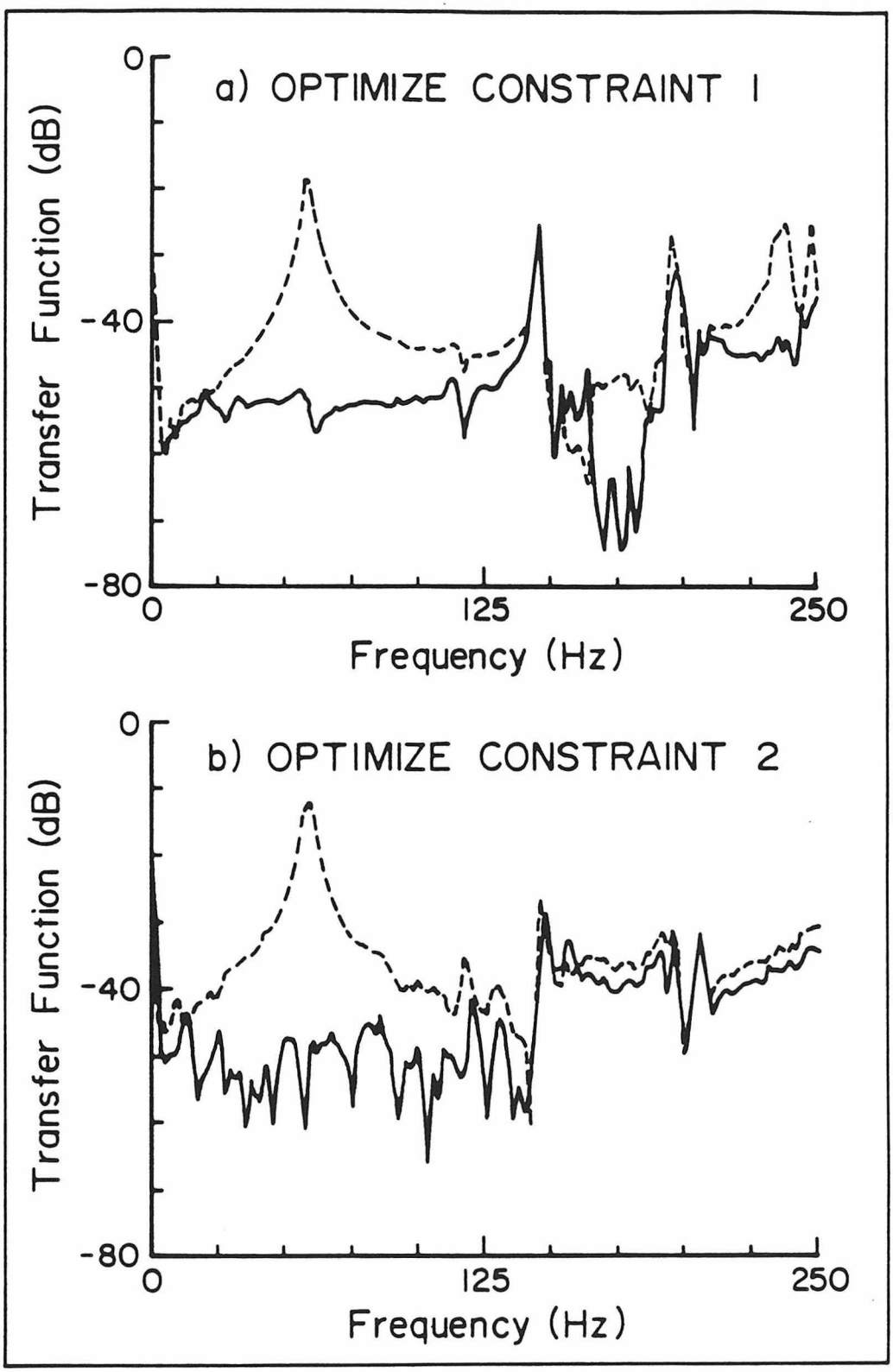

Figure A.13. The effect of adjusting the translation constraint wires on the coupling between control block orientation and position.

REFERENCES

Alpar, M.A., Cheng, A.F., Ruderman, M.A., and Shaham, J. 1982, *Nature*, **300,** 728, "A new class of radio pulsars".

Arons, J. 1983, *Nature*, **302,** 301, "On the magnetization and origin of the millisecond pulsar 1937+214".

Ashworth, M., Lyne, A.G., and Smith, F.G. 1983, *Nature*, **301,** 313, "The 1.5 ms pulsar PSR 1937+21".

Backer, D.C., Kulkarni, S.R., Heiles, C., Davis, M.M., and Goss, W.M. 1982, *Nature*, **300,** 615, "A millisecond pulsar".

Backer, D.C., Kulkarni, S.R., and Taylor, J. 1983, *Nature*, **301,** 314, "Timing observations of the millisecond pulsar".

Boriakoff, V., Buccheri, R., and Fauci, F. 1983, *I.A.U. circ. no. 3806*, "A second millisecond pulsar".

Boughn, S.P., Fairbank, W.M., Giffard, R.P., Hollenhorst, J.N., Mapoles, E.R., McAshan, M.S., Michelson, P.F., Paik, H.J., and Taber, R.C. 1982, *Ap. J.*, **261,** L19, "Observations with a low-temperature resonant mass, gravitational radiation detector".

Braginsky, V.B., and Thorne, K.S. 1980, Orange Aid Preprint 609, Caltech, "Present status of gravitational-wave experiments".

Chandrasekhar, S. 1970, *Phys. Rev. Lett.*, **24,** 611, "Solutions of two problems in the theory of gravitational radiation".

Djorgovski, S. 1982, *Nature*, **300,** 618, "Optical identification of the millisecond pulsar 1937+214".

Drever, R.W.P., Hoggan, S., Hough, J., Meers, B.J., Munley, A.J., Newton, G.P., Ward, H., Anderson, D.Z., Gürsel, Y., Hereld, M., Spero, R.E., and Whitcomb, S.E. 1982, at The Third Marcel Grossman Meeting on General Relativity, Shanghai, China (proceedings in press), "Developments in laser interferometer gravitational wave detectors".

Drever, R.W.P., Hough, J., Bland, R., and Lessnoff, G.W. 1973, *Nature*, **246,** 340, "Search for short bursts of gravitational radiation".

Fabian, A., Pringle, J., Verbunt, F., and Awade, P. 1983, *Nature*, **301,** 222, "Do galactic bulge X-ray sources evolve into millisecond pulsars?".

Forward, R.L. 1978, *Phys. Rev. D*, **17,** 379, "Wideband laser-interferometer gravitational-radiation experiment".

Friedman, J.L. 1983, preprint, "An upper limit on the frequency of pulsars".

Henrichs, H.F., and van den Heuval, E.P.J. 1983, *Nature*, **303,** 213, "Is the millisecond pulsar formed from a coalescence of a close neutron-star binary?"

Hirakawa, H., and Narihara, K. 1975, *Phys. Rev. Lett.*, **35,** 330, "Search for gravitational radiation at 145 Hz".

Hirakawa, H., Tsubono, K., and Fujimoto, M.-K. 1978, *Phys. Rev. D*, **17,** 1919, "Search for gravitational radiation from the Crab pulsar".

Hough, J., Drever, R.W.P., Ward, H., Munley, A.J., Newton, G.P., Meers, B.J., Hoggan, S., and Kerr, G.A. 1983, *Nature*, **303,** 216, "Direct observational upper limit to gravitational radiation from millisecond pulsar PSR 1937-214".

Hough, J., Pugh, J.R., Bland, R., and Drever, R.W.P. 1975, *Nature*, **254,** 498, "Search for continuous gravitational radiation".

Levine, J., and Stebbins, R. 1972, *Phys. Rev. D*, **6,** 1465, "Upper limit on the gravitational flux reaching the Earth from the Crab pulsar".

Manchester, R.N., Peterson, B.A., and Wallace, P.T. 1983, *I.A.U. circ. no. 3795*, "PSR 1937-214".

Mast, T.S., Nelson, J.E., Saarloos, J.A., Muller, R.A., and Bolt, B.A. 1972, *Nature*, **240,** 140, "Search for seismic signals from gravitational radiation of pulsar CP1133".

Michelson, P.F., and Taber, R.C. 1981, *J. Appl. Phys.*, **52,** 4313, "Sensitivity analysis of a resonant mass gravity wave antenna with resonant transducer".

Misner, C.W., Thorne, K.S., and Wheeler, J.A. 1973, *Gravitation*, (San Francisco: W.H. Freeman and Company).

Moss, G.E., Miller, L.R., and Forward, R.L. 1971, *Appl. Optics.*, **10,** 2495, "Photon-noise limited laser transducers for gravitational antenna".

Oide, K., Hirakawa, H., and Fujimoto, M.-K. 1979, *Phys. Rev. D*, **20,** 2480, "Search for gravitational radiation from the Crab pulsar".

Rüdiger, A., Schilling, R., Schnupp, L., Winkler, W. Billing, H., and Maischberger, K. 1982, preprint, MPQ 68, Max-Planck-Institut Für Quantenoptik, "Gravitational wave detection by laser interferometry - noise considerations, current status, and future prospects".

Sadeh, D., and Meidav, M. 1972, *Nature*, **240,** 136, "Periodicities in seismic response caused by pulsar CP1133".

Schilling, R. 1982, lecture delivered at Les Houches summer school on Gravitational Radiation.

Smarr, L. 1979, ed., *Sources of Gravitational Radiation*, Proceedings of the Battelle Seattle Workshop, July 24 - August 4, 1978 (Cambridge University Press).

Smith, F.G. 1977, *Pulsars*, (Cambridge: Cambridge University Press).

Spero, R. 1983, in *AIP Conference Proceedings No. 96, Science Underground (Los Alamos, 1982)*, edited by Michael Martin Nieto, W.C. Haxton, C.M. Hoffman, E.W. Kolb, V.D. Sandberg, and J.W. Toevs (New York: AIP), 347, "Prospects for ground based detectors of low frequency gravitational radiation".

Taylor, J.H., and Weisberg, J.M. 1982, *Ap. J.*, **253,** 908, "A new test of General Relativity: gravitational radiation and the binary pulsar PSR 1913+16".

Thorne, K.S. 1980, *Rev. Mod. Phys.*, **52,** 285, "Gravitational-wave research: current status and future prospects".

van den Heuval, E.P.J. 1977, in *Ann. N.Y. Acad. Sci.*, **302,** Eighth Texas Symposium on Relativistic Astrophysics, edited by M.D. Papagiannis, 14, "Evolution of close binaries and the formation of pulsars".

Wagoner, R.V. 1983, preprint, "Possible source of monochromatic gravitational radiation".

Weber, J. 1960, *Phys. Rev.*, **117,** 306, "Detection and generation of gravitational waves".

Weinberg, S. 1972, *Gravitation and Cosmology: Principles and Applications of the General Theory of Relativity*, (New York: Wiley).

Weiss, R. 1972, in Quarterly Progress Report 105, Res. Lab. Electronics, MIT, 54, "Electromagnetically coupled broadband gravitational antenna".

Whitcomb, S.E., Anderson, D.Z., Drever, R.W.P., Gürsel, Y., Hereld, M., and Spero, R. 1982, at The Third Marcel Grossman Meeting on General Relativity, Shanghai, China (proceedings in press), "Laser interferometer experiment at Caltech".

Zimmermann, M. 1978, *Nature*, **271,** 524, "Gravitational radiation from the Crab and Vela pulsars - a revised estimate".

Zimmerman, M., and Szedenits, E.,Jr. 1979, *Phys. Rev. D*, **20,** 351, "Gravitational waves from rotating and precessing rigid bodies: I. Simple models and applications to pulsars".